Glowing droplets : a diagnostic for particle-laden flows

Please check the document version of this publication:

• A submitted manuscript is the version of the article upon submission and before peer-review. There can be important differences between the submitted version and the official published version of record. People interested in the research are advised to contact the author for the final version of the publication, or visit the DOI to the publisher's website.
• The final author version and the galley proof are versions of the publication after peer review.
• The final published version features the final layout of the paper including the volume, issue and page numbers.

[Link to publication](#)

GLOWING DROPLETS
A DIAGNOSTIC FOR PARTICLE-LADEN FLOWS

GLOWING DROPLETS
A DIAGNOSTIC FOR PARTICLE-LADEN FLOWS

PROEFSCHRIFT

ter verkrijging van de graad van doctor aan de
Technische Universiteit Eindhoven, op gezag van de
rector magnificus, prof.dr.ir. C.J. van Duijn, voor een
commissie aangewezen door het College voor
Promoties in het openbaar te verdedigen
op donderdag 17 oktober 2013 om 16.00 uur

door

Humberto Bocanegra Evans

geboren te Monterrey, México

Dit proefschrift is goedgekeurd door de promotoren en de samenstelling van de promotiecommissie is als volgt:

voorzitter: prof.dr.ir. G.M.W. Kroesen
1$^\text{e}$ promotor: prof.dr.ir. G.J.F. van Heijst
2$^\text{e}$ promotor: prof.dr.ir. W. van de Water
copromotor: dr. N.J. Dam
leden: Prof.Dr. E. Bodenschatz (Georg-August-Universität
                Göttingen)
              prof.dr.ir. J. Westerweel (TUD)
              prof.dr. F. Toschi
              prof.dr. H.J.J. Jonker (TUD)

CONTENTS

CHAPTER 1

INTRODUCTION

The mixing ability of turbulent flows is unsurpassed. Most, if not all, large scale industrial and natural fluid mixing processes make use of this aspect [1]. From the trivial morning action of stirring cream into coffee to pollutants dispersing throughout the atmosphere, numerous processes rely on turbulent transport to achieve homogeneous concentrations. As in many other regards, the nonlinearity of the fluid motion has a surprise when it comes to multiphase mixtures. Particle- and bubble-laden turbulent flows exhibit a counterintuitive behavior: preferential concentration.

In these flows, the dispersed phase is segregated into regions with specific characteristics. As the inertia of the droplets increases, they become stubborn to changes in the flow, and lose the ability to faithfully follow fluid trajectories. There is evidence that regions of high vorticity (high centripetal acceleration) centrifuge the particles away from vortex cores and into high-strain areas [2]. This phenomenon is thought to have major relevance in many particle-laden processes. The aim of this thesis is to present a novel experimental technique that will support our efforts to understand the underlying dynamics of droplet-laden flows.

A droplet within a vortex is analogous to a fast car taking a curve. As the car turns, it feels outward force proportional to its speed and mass, and inversely proportional to the radius of the curve squared ($F_c = mv/r^2$). If the force is high enough to overcome the friction of the tires with the pavement, the car slips out of the curve. In much the same way, a droplet with a rela-

1

tively large mass or a high normal acceleration can be ejected out of a curved trajectory (Figure 1.1).
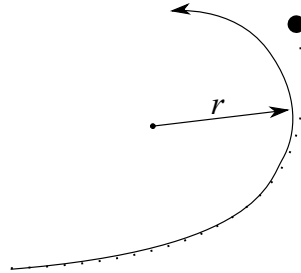
Figure 1.1: *As an inertial particle goes around a curved trajectory its mass prevents it from exactly following the path of a fluid particle. This is a similar situation as a car taking a tight curve at a high speed.*

Given the prevalence of particle-laden flows and the major relevance in many processes involving this type of flows, understanding the physics behind them is of utmost importance for scientific and economical purposes. Over the past few years this phenomenon has received increased attention, with numerous studies being published from experimental, theoretical and numerical perspectives. Even though these studies have increased the knowledge and understanding of the preferential concentration phenomenon, many questions remain unanswered. Recent reviews by Shaw [3] and Balanchandar [4] give a thorough overview of the achievements and some of the remaining challenges in fully understanding the physics of inertial particle physics. Additionally, Toschi & Bodenschatz [5] have reviewed the Lagrangian statistics of tracer and heavy particles in turbulent flows.

The core of this thesis is the elucidation of a new experimental technique that will allow the quantification of the dynamics of turbulent droplet clouds at the shortest timescale of the flow, i.e. the Kolmogorov timescale. The technique makes use of phosphorescent droplets to tag a well defined region inside a cloud. The droplets are made out of a phosphorescent solution and, when excited, emit light for a period of time comparable to the dissipative timescales of the flow.

The present chapter will provide the relevant background that will familiarize the reader with general aspects of particle-laden flows, particularly those involving turbulence. This will provide a base for our subsequent analysis. First, however, we shall briefly address the general characteristics of

turbulent flows and the equation of motion of a particle suspended in a non-uniform unsteady velocity field.

1.1   Equations of fluid motion

Together with the incompressibility requirement $\nabla \cdot \boldsymbol{u} = 0$, fluid motion is mathematically described by the Navier–Stokes equation

$$\frac{\partial u_i}{\partial t} + u_j \frac{\partial u_i}{\partial x_j} = -\frac{1}{\rho}\frac{\partial p}{\partial x_i} + \nu \frac{\partial^2 u_i}{\partial x_j \partial x_j}, \tag{1.1}$$

where u_i represents the ith component of the velocity vector $\boldsymbol{u}$ at a point $\boldsymbol{x}$ in space and p is the pressure at the same point. The velocity field of a dispersed flow is also described by Eq. (1.1), but it must be augmented by an equation of motion for the discrete particles and terms in each equation that characterize the interplay between the fluid velocity field and the particle motion. For very dilute suspensions of point-like particles, the effect of particles on the fluid may be omitted: one-way coupling; whereas for dense suspensions or large particles, the motion of the particle fraction reacts back on the fluid, i.e. two-way coupling. Even higher densities may introduce particle–particle interactions, a regime known as four-way coupling. In our experiments, the concentration of the droplets is so small that the first situation pertains.

Turbulence is commonly defined as the chaotic motion of a fluid where all scales of the flow mutually interact. Even though analytical solutions have been reached for a few simple cases, in a turbulent environment the nonlinearity of the Navier–Stokes equation renders an analytical solution impossible. Chaotic systems are extremely sensitive to initial conditions, which means that even if we could analytically solve the Navier–Stokes equations, the accuracy with which the initial conditions must be defined would be impossible to accomplish. Fortunately, the chaotic behavior of turbulent flows can be analyzed from a statistical perspective, as long as the flow is statistically steady.

Whether a flow will become turbulent is not a straightforward determination. Conventionally, a comparison between the inertial forces and the viscous forces is a good indication of the regime in which the flow is situated. The non-dimensional Reynolds number Re gives the ratio between these two forces. Slow or viscosity-dominated flows are said to be laminar, whereas flows dominated by inertia are turbulent. The threshold between these regimes

is not well defined. Moreover, this threshold depends on the geometry of the flow. The Reynolds number is commonly defined as

$$\mathrm{Re} = \frac{\mathcal{L}V}{\nu},\tag{1.2}$$

where $\mathcal{L}$ and V represent a characteristic length scale and velocity of the flow, respectively, and ν is the kinematic viscosity of the fluid.

The statistical analysis of turbulent flows can be accomplished by the decomposition of the instantaneous velocity into a mean ($^-$) and a fluctuating part ($'$), $\boldsymbol{u} = \bar{\boldsymbol{u}}\left(\boldsymbol{x}\right) + \boldsymbol{u}'\left(\boldsymbol{x}, t\right)$, resulting in

$$\bar{u}_j \frac{\partial \bar{u}_i}{\partial x_j} = \frac{\partial}{\partial x_j}\left[-\frac{1}{\rho}\bar{p}\delta_{ij} + \nu\left(\frac{\partial \bar{u}_i}{\partial x_j} + \frac{\partial \bar{u}_j}{\partial x_i}\right) - \overline{u'_i u'_j} \right].\tag{1.3}$$

These equations are commonly referred to as Reynolds-averaged Navier–Stokes, and are primarily used in modelling of turbulent flows. One of their drawbacks is the lack of closure, that is, there are more unknowns than available equations. Most modelling approaches rely on the development of assumptions to address the closure problem for the Reynolds stresses $\overline{u'_i u'_j}$.

A parallel approach to the understanding of turbulence comes from phenomenological analysis, that is, through observations and ideas that do not arise directly from theoretical derivations. One of the most commonly used avenues in the understanding of turbulence is scale analysis. Turbulence is made up of many eddies with different sizes and all of them can interact with each other. The size of the largest eddies is constrained by the size of the system, whereas the smallest eddies are determined by the energy dissipation of the flow and the viscosity of the fluid. In almost all cases, the energy input is in the largest length (L) and timescales (T) of the flow. Due to vortex stretching and breakup, the energy cascades down into what is known as the inertial subrange. In this subrange, inertial forces are much larger than viscous forces, and as the length- and timescales decrease towards the lower limit of the inertial subrange, viscous forces become ever more apparent. However, it is not until the smallest scales of the flow that viscous forces dominate, and where the smallest eddies of the flow die, victim of viscous dissipation. Following this phenomenological analysis, Kolmogorov was able to predict the magnitude of the smallest scales [6].

The dissipative scale of the flow, commonly referred to as the Kolmogorov scale, is solely dependent on the viscosity of the fluid ν and the energy dissipation rate ε; they are defined as

$$
\begin{aligned}
\eta &= (\nu^3/\varepsilon)^{1/4} && \text{(spatial scale)} \\
\tau_\eta &= (\nu/\varepsilon)^{1/2} && \text{(temporal scale)} \\
v_\eta &= (\nu\varepsilon)^{1/4} && \text{(velocity scale)}.
\end{aligned}
\tag{1.4}
$$

It can readily be seen that, at these scales, viscous and inertial forces are equal, resulting in a Reynolds number of unity.

1.1.1 Statistical tools

As mentioned in Section 1.1 above, turbulent flows are commonly analyzed from a statistical perspective. Experiments allow us to measure properties of the flow, usually the velocity at one or more points, either in a time-resolved or a time independent fashion. However, the velocity measurements themselves do not tell the entire story, and a great deal of information can be obtained from statistical analysis of these measurements.

To obtain information about the structure of the flow, we use, among other things, the structure function

$$
G_p(r) = \langle (u(x + r) - u(x))^p \rangle,
\tag{1.5}
$$

where $\langle \cdot \rangle$ denotes an ensemble average and r is the distance between two points. The structure function gives information on the magnitude of the velocity difference between a point and its surroundings, which in turn, allows us to get information about length scales of the structures present in the flow. Based on phenomenological arguments, Kolmogorov [6] arrived at a universal description of these velocity differences. This presumed universality rests on an exact result, and an extrapolation which later proved wrong.

The exact result for the third-order structure function is,

$$
G_3(r) = -\frac{4}{5}\varepsilon r,
\tag{1.6}
$$

when r is within the inertial range. Kolmogorov extrapolated this result to arbitrary order,

$$
G_p(r) = C_p \varepsilon^{p/3} r^{p/3}.
\tag{1.7}
$$

For the second-order structure function, this definition leads to

$$G_2(r) = C_2(\varepsilon r)^{2/3},$$ (1.8)

whose complementary energy spectrum becomes

$$E(\kappa) = C_k \varepsilon^{2/3} \kappa^{-5/3},$$ (1.9)

where κ corresponds to the wavenumber.

For $p \neq 3$ we know that small but essential corrections to this extrapolation are needed, which owe to the intermittency of turbulence [7]. Intermittency is the tendency of the flow to explore extreme situations, such as extreme values of the velocity differences or accelerations. This phenomenon results in a higher value of the kurtosis, that is, heavier tails in the distribution of these values. The appearance of intermittency at the dissipative scales is well documented, while intermittency in the inertial range leads to anomalous scaling behavior, in conflict with Kolmogorov's theory. ([7] and references therein). We believe that preferential concentration and turbulent intermittency are not related, and that preferential concentration also occurs in weakly turbulent flows with 'normal' statistics. The topic of intermittency, however, is beyond the scope of this thesis. For a in-depth review, we refer the reader to [7] and [8].

1.1.2   Equation of motion for a sphere

The motion of a sphere suspended in a flow field is a fundamental problem in fluid mechanics. Many aspects must be considered in order to correctly represent the forces acting on the sphere. Maxey & Riley [9] derived the equation of motion for a sphere in a non-uniform, unsteady flow. The equation takes into account the pressure gradient, added mass, Stokes drag, Basset history term, and buoyancy. A force balance results in

$$
\begin{aligned}
m_p \frac{\mathrm{d} v_i}{\mathrm{d} t} =\ & (m_p - m_f)\, g_i + m_f \left. \frac{D u_i}{D t} \right|_{\mathbf{Y}(t)} \\
& - \tfrac{1}{2} m_f \frac{\mathrm{d}}{\mathrm{d} t} \{ v_i(t) - u_i[\mathbf{Y}(t)] - \tfrac{1}{10} r_p^2 \nabla^2 u_i|_{\mathbf{Y}(t)} \} \\
& - 6\pi r_p \mu \{ v_i(t) - u_i[\mathbf{Y}(t), t] - \tfrac{1}{6} r_p^2 \nabla^2 u_i \,|_{\mathbf{Y}(t)} \} \\
& - 6\pi r_p^2 \mu \int_0^t \mathrm{d}\tau \left(\frac{\mathrm{d}/\mathrm{d}\tau \{ v_i(t) - u_i[\mathbf{Y}(t), t] - \tfrac{1}{6} r_p^2 \nabla^2 u_i \,|_{\mathbf{Y}(t)} \}}{[\pi \nu(t - \tau)]^{1/2}} \right),
\end{aligned}
$$ (1.10)

where r_p is the radius of the sphere, g_i is the gravitational acceleration, and μ is the viscosity of the carrier fluid. The mass of the sphere is represented by m_p, while the mass of the fluid displaced by the particle is m_f; v_i and u_i are the particle and fluid velocities, respectively. $\mathbf{Y}(t)$ symbolizes the particle position in a Lagrangian reference frame.

In the particular case of water droplets suspended in air ($\rho_f \ll \rho_p$) the added mass term can be neglected in view of the large density difference that exists between the carrier flow and the dispersed phase. Furthermore, the inclusion of gravity must be determined for the case at hand, since the terminal velocity of the particle must be compared to the velocity fluctuations of the turbulent field.

The Faxén correction term ($r_p^2 \nabla^2 u_i|_{\mathbf{Y}(t)}$) accounts for forcing that arises due to velocity gradients along the surface of the sphere. When the diameter of the sphere is much smaller than the characteristic length scale of the flow—the Kolmogorov length scale in this particular case—the term can be neglected. The integral term in Eq. (1.10) represents the Basset history term, which addresses the dynamical nature of the boundary layer around a sphere in unsteady flow. It can be seen from the prefactor, that for very small diameters ($\mathcal{O}(10\,\mu\text{m})$) and large density ratios ($\rho_p/\rho_f \gg 1$), this term is negligible in comparison to the Stokes drag. Nevertheless, certain studies have warned that the value may have a considerable magnitude in specific cases (see e.g. [10]), i.e. for light and neutrally buoyant particles as well as particles with large diameters relative to the Kolmogorov lengthscale. To find the value of this term an integral must be carried out at every time, making the calculation prohibitively expensive. Fortunately, in many cases the term can be neglected altogether, particularly when the droplets are very small compared to the scales of the flow. Nevertheless, high-accuracy approximations have been proposed by van Hinsberg et al. [11].

Not included in Maxey & Riley's equation above is Brownian motion—a random motion resulting from the collision of fluid molecules with small droplets. This effect becomes apparent when the mass of the particle is very small, i.e. low density and/or small radius. In the present study Brownian motion can be disregarded given the size of the droplets and the density ratio of the fluids.

After applying the above assumptions we come to the equation of motion

for a point-particle with finite mass,

$$\frac{\mathrm{d}v_i}{\mathrm{d}t} = \frac{1}{\tau_p}(u_i - v_i), \qquad (1.11)$$

where the relaxation timescale of the particle τ_p represents the time a particle takes to adjust to the surrounding flow. The Stokes number is a commonly used non-dimensional parameter that quantifies the particle inertia in comparison with the flow timescales. In turbulent flow situations, it is usually defined as the ratio between τ_p and the Kolmogorov timescale τ_η, St $= \tau_p/\tau_\eta$. Numerical simulations and experiments have shown that preferential concentration is most evident when St ~ 1 [3, 12]. The explanation for this behavior is that particles with St $\ll 1$ follow the flow more precisely and particles with St $\gg 1$ filter a larger range of small-scale fluctuations.

1.1.3 Particle relaxation time

The time it takes for a droplet to adapt to its surroundings is normally referred to as the particle relaxation time or the particle reaction time. Its value depends on the density ratio between the particle and carrier flow, as well as its viscosity and the diameter of the particle. Through a force balance on a free-falling droplet, we can obtain the particle relaxation time. The forces acting on a droplet in still air are the drag force (in the vertical, positive direction) and its own weight (on the vertical, negative direction), so that Newton's second law becomes

$$F_D - m_p g = m_p \frac{\mathrm{d}V_p}{\mathrm{d}t} \qquad (1.12)$$

We know that the drag force on a spherical droplet under Stokes drag (Re$_p \ll 1$) is $F_D = 3\pi d_p \mu V_p$. Substituting this into Eq. (1.12) we get

$$m_p \frac{\mathrm{d}V_p}{\mathrm{d}t} = 3\pi d_p \mu V_p - m_p g. \qquad (1.13)$$

Because the droplet considered in the current study is not in still air, the relative velocity of the droplet with respect to the air velocity $(u(t) - V_p)$ should be accounted for; Eq. (1.13) becomes

$$\frac{\mathrm{d}V_p}{\mathrm{d}t} = \frac{1}{\tau_p}\left(u(t) - V_p\right) - g, \qquad (1.14)$$

where

$$\tau_p = \frac{\rho d_p^2}{18\mu} \tag{1.15}$$

is the relaxation time. The solution of this equation can be obtained readily for a droplet that is accelerated from rest by setting $V_p(t) = \widetilde{V}_p e^{-t/\tau_p}$, with $\widetilde{V}_p(t = 0) = 0$. Differentiating with respect to time and rearranging we get

$$\frac{\mathrm{d}\widetilde{V}_p}{\mathrm{d}t} = \frac{1}{\tau_p}u(t)e^{t/\tau_p} - g\,e^{t/\tau_p}, \tag{1.16}$$

which can be integrated to arrive at

$$\widetilde{V}_p(t) = \frac{1}{\tau_p}\int_0^t u(t')\,e^{t'/\tau_p}\,\mathrm{d}t' - \frac{1}{\tau_p}g\left(e^{t/\tau_p} - 1\right). \tag{1.17}$$

Finally, we go back the the original velocity V_p,

$$V_p(t) = \frac{1}{\tau_p}\int_0^t u(t')e^{\frac{t'-t}{\tau_p}}\,\mathrm{d}t' - \frac{1}{\tau_p}g\left(1 - e^{-t/\tau_p}\right), \tag{1.18}$$

so that the droplet velocity lags a time τ_p behind the velocity field.

1.2 Background: particle-laden flows

Scientists and engineers have been interested in particle-laden flows for decades, which has resulted in a vast collection of theoretical, numerical and experimental studies (see e.g. [3, 5]). Such interest is owed to the many applications that can be given to these flows. For example, Falkovich et al. [16] argue that the phenomenon of preferential concentration affects the evolution of droplet sizes within clouds, increasing the probability of collisions, which in turn results in accelerated droplet growth. The dispersion of inertial particles is also of interest in both environmental and industrial contexts. Many studies suggested the approximation of particle trajectories as fluid parcels (see e.g. [17]), however, in the recent past we have learned that this is an incorrect assumption [13]–[15].

The information obtained from these, and many other, investigations has dramatically increased our understanding and helped in the advancement of the field, yet many questions remain. Let us review a few of these studies to obtain a clear perspective of the problem at hand.

1.2.1   Preferential concentration

The possibility of having a compressible particle field within an incompressible fluid velocity field, was first pointed out by Maxey [13]. This could lead to inhomogeneities in the concentration of the dispersed phase (see Figure 1.2) even when the carrier flow is homogeneous and isotropic. For incompressible flows, the divergence of the velocity field $\nabla \cdot \boldsymbol{u} = 0$. On the other hand, the divergence of an inertial particle field is described by

$$\nabla \cdot \boldsymbol{v} = -\frac{\tau_p}{4} \left[S^2 - \Omega^2 \right] , \tag{1.19}$$

where S and Ω represent the strain and vorticity, respectively. It can be seen from the above equation that droplets will be ejected from vorticity dominated regions and agglomerate in strain dominated areas. This can be explained by the inability of particles to withstand high centripetal accelerations, being centrifuged out of vortices (as pictured in Figure 1.1). The highest accelerations in a flow field are expected to be at scales comparable to the Kolmogorov scales, therefore we anticipate the inhomogeneities to be more pronounced at these scales. Additionally, we observe the that divergence is proportional to the Stokes number, meaning that clouds with heavier particles will experience more pronounced segregation. However, this equation is only valid for relatively low Stokes numbers, as will be shown in Chapter 6.
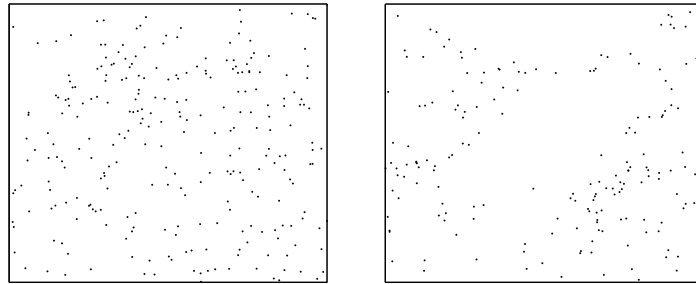
Figure 1.2: *Snapshot of numerical simulation of (a) light and (b) heavy particles in homogeneous isotropic turbulence. The slices have dimensions of $500\eta \times 500\eta \times 50\eta$. It can be readily seen that light particles are more homogeneously distributed. Also, the heavy particle spatial distribution shows voids. The data was obtained from the iCFDdatabase (see [18]).*

There is no particular diagnostic that answers all of our questions regarding particle-laden flows. On the experimental side, several techniques have been used in order to examine the physics of multiphase flows, each one resulting in valuable information that was not available with other diagnostics. Point-like diagnostics such as phase-Doppler anemometry (PDA) have been used to probe the spatial properties of inertial particle dispersion. Saw et al. [12] employed PDA to measure the deviation in the distribution of particles from a truly homogeneous suspension. Additionally, multidimensional experimental methods such as particle tracking velocimetry (PTV), have been employed to assess the behavior of inertial particles in turbulent flows. For example, using PTV, Gibert et al. [19] found that heavy particles tend to visit strain-dominated areas of the flow. Also using PTV, Ayyalasomayajula et al. [20] have shown that the fluctuations of the particle acceleration are reduced due to inertial filtering effects.

Numerical simulations have also played a crucial role in the study of preferential concentration by providing information that is unaccessible through experiments. The increase in computing power achieved in recent years has made it possible for scientists to numerically simulate flows with considerably high Reynolds numbers. However, the quantity of droplets and the time span that can be simulated remain an obstacle in the simulation of flows with high droplet concentration. Nevertheless, many of these simulations support the idea of preferential concentration. Calzavarini et al. [21] looked at the spatial scales of the segregation of two different sets of particles, while Bec et al. [22] found that the dimensionality of the particle distribution is at its lowest when particles have a Stokes number St ≈ 0.6.

Many other experiments and numerical simulations have been carried out. A more comprehensive review will be given in Chapter 6, where we will explore the phenomenon of preferential concentration using the phosphorescent tagging technique.

1.2.2 Dispersion of heavy particles

Most of the work on dispersion is focused on times comparable to the integral timescale T, given common applications such as diffusion of pollutants in the atmosphere. Here we revisit this problem through the new perspective given by our proposed technique. A comprehensive review about dispersion will be given in Chapter 5; for now, let us briefly look at some of the relevant literature.

Taylor [23] set the foundation for the analysis of the dispersion problem. In his study, the dispersion of scalar particles from a point source was addressed. The analysis was performed from an Eulerian reference frame, but made use of Lagrangian autocorrelation of a particle. For times much smaller than the Lagrangian integral time T_L, the mean square displacement is given by

$$x^2(t) = x^2(0) + \langle v^2 \rangle t^2, \tag{1.20}$$

whereas for times $t \gtrsim T_L$ dispersion is given by

$$x^2(t) = 2\langle v^2 \rangle T_L t. \tag{1.21}$$

A few years later, Richardson [24] studied the dispersion of particle clouds in the atmosphere and, through observations, arrived at the famous relation

$$\Delta^2(t) = g\varepsilon t^3, \tag{1.22}$$

where g is known as the Richardson constant. This result, however, is applicable only after time $t > t_0 = (\Delta_0^2/\varepsilon)^{1/3}$, once the correlation between neighboring particles has been lost and the initial separation Δ_0 is no longer important.

Batchelor [25] analyzed the dispersion of a pair of particles within the inertial range. He approached the problem using the known (two-thirds power law) behavior of the second-order structure function. In this regime, the governing equation is

$$\langle \Delta^2(t) - \Delta_0^2 \rangle = \frac{11}{3} C_2 \left(\varepsilon \Delta_0 \right)^{2/3} t^2. \tag{1.23}$$

Both Richardson's and Batchelor's analyses follow the particle pairs in a Lagrangian frame of reference.

Recently, with the help of more powerful computers and modern experimental techniques, a renewed interest has arisen in the topic of dispersion. Ouellette [26] performed particle tracking in homogeneous isotropic turbulence, finding an outstanding agreement with Batchelor's pair dispersion relation. Richardson's t^3 scaling was observed only for the smallest achievable initial separation. It was argued, however, that for most natural and practical applications the t^3 scaling may not be reached given the relatively small separation between T_L and t_0. Nevertheless, all of the above analyses pertain to the dispersion of fluid particles and tracers, whereas the present work focuses on the behavior of heavy particles. In the context of heavy particles,

dispersion is expected to differ, although the way inertial effects will become apparent is not entirely clear.

A different analysis can be obtained by calculating the Lyapunov exponents of a system, which give an indication of the speed at which two infinitesimally close trajectories in phase space separate. A three-dimensional dynamical system has six Lyapunov exponents $\lambda_1 > \cdots > \lambda_6$, with λ_1 known as the maximal Lyapunov exponent. A positive value for this exponent is usually associated with a chaotic system. The use of Lyapunov exponents as a mathematical tool to analyze particle behavior presents certain advantages. Bec et al. [27] studied the dependence of Lyapunov exponents of inertial particles on Stokes number. The largest Lyapunov exponent λ_1 is affected by two competing mechanisms: the filtering effect of inertia, which weakens chaoticity and the preferential concentration of particles in high strain regions, which presents a higher stretching rate, thus increasing the chaoticity. The ratio $\lambda_1(\text{St})/\lambda_1(\text{St}=0)$ has a maximum at $\text{St} \approx 0.35$, which is explained by the preferential probing of strain-dominated regions by heavy particles.

1.2.3 Gravity effects

Several studies have noted the importance of gravity in particle and droplet behavior [28]–[31]. Two distinct mechanisms have been pointed out in regard of gravity effects, the first of which is known as the 'crossing trajectories' mechanism, whose name refers to the crossing of particles from one eddy to another due to the force gravity exerts on them. This mechanism has been linked to a faster decorrelation of the velocity of a particle as a result of a particle crossing to an adjacent eddy instead of remaining within the same eddy for the entire turnover time.

In clouds, gravity effects become apparent on droplets that have reached increased settling velocities. Heavy settling droplets tend to travel through regions of high strain, circumventing vortex cores. As has been previously stated, it is precisely in these regions where droplets agglomerate due to preferential concentration. Therefore, it has been proposed that, as heavier droplets settle, they coalesce with smaller droplets while sweeping through high droplet concentration regions. This phenomenon is known as 'preferential sweeping', and has been linked to enhanced droplet growth in clouds, leading to rain initiation.

Buoyancy forces play a similar role as gravity. Gopalan et al. [32] used 3D holography to follow the trajectories of diesel drops in turbulent water flow.

They found that in some instances droplets have a faster dispersion than the theoretical prediction for fluid parcels. However, the similarity between the densities of the dispersed and carrier phases results in a different interaction than in gas–liquid situations.

1.3   This thesis: glowing clouds in the lab

Inhomogeneities in the concentration of particles have major relevance in many industrial settings, for example fuel injection in internal combustion engines. The homogeneity of the air–fuel mixture plays a role in the efficiency of combustion [33]. Evidently, preferential concentration could negatively impact the homogeneity of the mixture. As we have previously mentioned, acceleration in rain initiation has been linked to particle–turbulence interactions. Given the large scales of clouds, the local characteristics of the flow are ideal, i.e. homogeneous isotropic turbulence with zero mean flow. It is our aim to replicate such flows in the laboratory. Let us now look at some flow properties of clouds and the challenges of replicating these in the laboratory.

1.3.1   Replicating cloud conditions

There is a common belief that condensation is the only driving force behind precipitation. While it is true that condensation plays an important role in droplet growth, it is a dominant effect only for droplets with diameters smaller than $10\,\mu$m, while gravity is the dominant mechanism for droplet growth for diameters greater than $30\,\mu$m [34]. Some studies [16, 3, 28, 35] point to turbulence as the missing link between these two regimes. It is postulated that turbulence induces inhomogeneities in the particle concentrations, which in turn modifies the collision kernel and increases the probability of collision between droplets. If droplet collisions result in their coalescence, they can quickly grow until the effects of gravity become apparent.

Acquiring field data in turbulent clouds is a challenging task. Temperature, (turbulent) flow properties as well as droplet size and concentration are relevant in the characterization of the system. The turbidity resulting from high droplet concentration makes optical velocity measurements particularly difficult. In addition, hot-wire anemometers are delicate instruments prone to damage when struck by even the tiniest of droplets. Recently, Siebert et al. [36] were able to measure turbulent statistics in a cloudy boundary layer

using sonic anemometers, finding an elevated turbulence intensity. Moreover, their data was in good agreement with expected theoretical values for locally isotropic turbulence.

A substantial amount of data regarding droplet sizes and spatial structure has been gathered using the Fast Forward Scattering Spectrometer Probe (Fast-FSSP), designed by Brenguier and coworkers [37]. Analyzing a collection of measurements from the Fast-FSSP, Chaumat & Brenguier [38] could not conclusively measure the degree of clustering due to uncertainty limitations of the probe. However, Kostinksi & Shaw [39] using data from the same apparatus but an alternative clustering indicator, confirmed statistically significant clustering.

Clouds may reach integral length scales on the order of 10^3 m, while having dissipative length scales reaching 10^{-3} m [40], resulting in well separated scales and great local isotropy and homogeneity with virtually zero mean flow. The following two chapters will describe the steps taken to construct the working setup that simulates cloud-like conditions in the laboratory.

This thesis focuses on experimental work to develop and test a novel diagnostic that will yield information about the behavior of heavy droplets suspended in an isotropic, homogeneous turbulent velocity field with zero mean flow. Generating such flow has proven challenging, however, Hwang & Eaton [41] successfully fabricated an experimental facility capable of generating this type of flow; several refined designs have followed since [42]–[44]. In Chapter 2 we give an overview of the different approaches taken to generate homogeneous isotropic turbulence with zero mean flow, and perform a scale analysis to optimize the turbulence generation for its application to droplet tagging. We will also describe the flow characterization system used in our measurements.

Clouds are made up of a broad distribution of droplet sizes. Nevertheless, to find a concrete dependence of the droplet dynamics as a function of their inertia, it is our goal to measure inertia effects on flows that have a well-defined Stokes number. This raises a new challenge considering that the generation of monodisperse droplets is a non-trivial task. Additionally, the measurement of the diameter of droplets of micrometer size presents challenges of its own. In Chapter 3 we will address the generation of a well characterized aerosol and the size measurement of the generated droplets. Additionally, we address practical issues regarding droplet generation and measurement, and provide details of the automated data processing algorithm that was developed.

1.3.2   Glowing droplets

The uniqueness of our method rests on the possibility of tagging particles, practically rendering all non-tagged particles invisible. Molecular tagging velocimetry has been used as a flow diagnostics for decades. Both fluorescence and phosphorescence have been used to obtain information about flows. From straightforward velocity measurements in Poiseuille flow to pressure sensing paint in aircraft models, the possibilities are comprehensive. In the present study we use a phosphorescent solution to observe the behavior of heavy droplets. Previously, a similar idea was used by Krüger & Grünefeld [45] to obtain velocity measurements in a fuel injector spray. In their study, however, only a snapshot of the velocity field was obtained, as it was possible to obtain only one pair of images in every tagging sequence.

In our study we aim to uncover the dynamical behavior of the clustering phenomenon, which requires a sequence of images that span a few Kolmogorov times. To this aim, a solution with a longer lasting phosphorescence was sought. This can be applied in a variety of situations, e.g. dispersion of a droplet cloud where only the tagged volume will be visible after the tagging procedure. Ideally, we would like a phosphorescent solution that glows for extended periods of time, say, comparable to the integral timescale T. Even though this is not currently possible, we believe that the ability to follow tagged droplets for several Kolmogorov times will provide valuable insight into the dynamics of preferential concentration. In addition, the tagging technique remains functional at much higher particle concentration than techniques such as PTV. In Chapter 4 we will explain the photophysics involved in Molecular Tagging Velocimetry (MTV) as well as the characterization and optimization of the phosphorescent solution used in our experiment.

1.3.3   Dispersion and preferential concentration at the Kolmogorov timescales

Once it is possible to generate the desired flow conditions, we explore two fundamental aspects of the behavior of particle-laden flows. First, the long-standing problem of turbulent dispersion is revisited in Chapter 5. Dispersion is of great interest in atmospheric flows, thus has been mostly analyzed at the integral timescales, that is, the longest timescales of the flow, while knowledge about the dynamics at the dissipative scales is scarce. Using our novel technique we focus on the dispersion of a cloud of heavy droplets at such

length and timescales.

Chapter 6 addresses the interesting topic of preferential concentration. Most of the research on this particular topic consists of statistical snapshots of the distribution of droplets in a turbulent velocity field. As important as these statistics are, we are interested in the time and length scales of clustering, and the dynamics of segregation. With the newly developed phosphorescent tagging technique we aim to shed light on the dynamics of particle clustering and its scales.

CHAPTER 2

TURBULENCE CHAMBER AND FLOW STATISTICS

It is the goal of this study to shed light on the dynamics of droplets suspended in homogeneous, isotropic turbulence with zero mean flow. This type of 'idealized' turbulence has been studied in depth numerically, analytically and, in recent years, experimentally. The attributes of this type of flow are well established, giving us the opportunity to compare and validate our experimental results. To this aim we have designed and tested a turbulence chamber.

As previously mentioned, our idea is to selectively tag droplets by dissolving phosphorescent molecules in water, making droplets out of this solution, illuminating the droplets by a laser and following the droplets using a fast camera, thus giving us the ability to study the dynamics of preferential concentration on the smallest time and length scales.

Important constraints in the design of the experiment are the phosphorescence lifetime τ_{ph} of the droplets, the camera exposure time t_e of the imaged cloud, and the desired spatial resolution of the registered image. In addition, the Reynolds number of the flow should be as large as possible. The key turbulence parameters that can characterize the flow are the turbulent velocity fluctuations u (or the turbulent energy per unit mass q^2, which in the isotropic case is $q^2 = 3u^2$) and the energy dissipation rate ε. In this chapter we will describe the relevant scales of the flow (Section 2.1) and how these impact the design of the chamber. Afterwards (Section 2.2), we will briefly discuss

the available methods to measure turbulence statistics, and, in particular, describe our particle image velocimetry setup. In Section 2.3 we will present the resulting velocity fields and flow statistics. Concluding remarks will be given in Section 2.4.

2.1   Turbulence chamber design

In recent years, several devices capable of producing homogeneous, isotropic turbulence have been designed [41]–[43]. Each in its own way, these designs rely on generating a mean transfer of momentum while maintaining mass transfer at a minimum, on average. Table 2.1 summarizes the turbulence statistics of three experimental facilities capable of producing such flows. Let us briefly look at the methods used to generate them. Hwang & Eaton's (H&E) [41] design consists of a cubical box whose corners have been cut off to accommodate eight synthetic jet actuators, one in each corner. The actuators are driven by random noise to produce homogeneous, isotropic turbulence with zero mean flow. The maximum stable Reynolds number reached was $Re_\lambda = 218$.

Using water as a working fluid, Zimmermann et al. [42] fabricated an icosahedral chamber with opposing propellers in each of its twelve vertices to create homogeneous isotropic turbulence. They named their apparatus the Lagrangian Exploration Module (LEM). The increased number of symmetry axes appears to be beneficial for the homogeneity of the flow. The maximum attainable Taylor-based Reynolds number is considerably high, reaching $Re_\lambda = 330$. The use of water is beneficial in certain aspects, such as a longer Kolmogorov timescale, which would reduce the necessary time resolution of the velocity measurement system. However, due to the increased density of the carrier fluid, reaching $St \sim 1$ would most probably compromise the requirement of $d_p \ll \eta$ necessary for the point-particle assumption.

Study	Fluid	u_{rms} (m/s)	λ (mm)	Re_λ	η (μm)	τ_k (μs)
H&E [41]	air	0.85	3.83	218	132	1160
LEM [42]	water	0.13	2.7	330	73	5300
Chang et al. [43]	air	1.1	6.4	481	155	1500

Table 2.1: *Summary of turbulence statistics of recent experimental facilities capable of producing homogeneous isotropic turbulence with zero mean flow.*

Following the trend of increased number of axes of symmetry, Chang et al. [43] used a truncated icosahedron (similar to a soccer ball) and placed synthetic jets on each of its 32 faces. Such an amount of axes of symmetry allowed them not only to obtain an outstandingly homogeneous, isotropic flow with $\mathrm{Re}_\lambda = 481$, but also to accurately generate and control flows with prescribed anisotropic characteristics. Since every face of the chamber was used to mount speakers, the optical access was limited to small orifices. It was through some of these orifices that they introduced laser beams for laser-Doppler anemometry measurements. For our particular experiment, optical access for cameras is essential, making this design problematic.

We conclude that the best option for our particular requirements is an improvement on Hwang & Eaton's design, since we plan to use optical diagnostics. Our aim is to increase the maximum attainable Reynolds number, while maintaining homogeneity and isotropy. In what follows, we will explore our possibilities to achieve this.

2.1.1 Length and timescales of turbulence

The energy dissipation rate $\varepsilon \equiv 2\nu\langle s_{ij}s_{ij}\rangle$ ($s_{ij} \equiv$ rate-of-strain tensor) lies at the core of the phenomenological analysis of turbulence made by A.N. Kolmogorov in his seminal 1941 paper [6]. For homogeneous isotropic turbulence, it becomes

$$\varepsilon = 15\nu\left\langle \left(\frac{\partial u_1}{\partial x_1}\right)^2 \right\rangle, \tag{2.1}$$

(see Appendix A.1 for derivation). This can be used to determine relevant turbulent scales, i.e. the Taylor microscale λ and the Kolmogorov length and time scales η and τ_η, respectively, through the following relations

$$\lambda = \left(\frac{5\nu q^2}{\varepsilon}\right)^{1/2} = \left(\frac{15\nu u^2}{\varepsilon}\right)^{1/2} \tag{2.2}$$

$$\tau_\eta = \left(\frac{\nu}{\varepsilon}\right)^{1/2} \tag{2.3}$$

$$\eta = \left(\frac{\nu^3}{\varepsilon}\right)^{1/4}. \tag{2.4}$$

The integral and Kolmogorov length scales are related to the Taylor-based

Reynolds number Re_λ by

$$\frac{L}{\eta} = C_\varepsilon 15^{-3/4}\text{Re}_\lambda^{3/2}, \tag{2.5}$$

where C_ε is a dimensionless constant of order 1, and the integral length scale L is defined in terms of the normalized correlation function $R_{ii}(x)$ (such that $R_{ii}(0) = 1$) as

$$L = \int_0^\infty R_{ii}(x)\mathrm{d}x. \tag{2.6}$$

Since turbulence becomes more independent of the way it is stirred as the ratio between the integral scale and the Kolmogorov scale grows, it is convenient to strive for the highest obtainable ratio. Combining (2.4) with the Kolmogorov estimate of the dissipation rate,

$$\varepsilon = C_\varepsilon \frac{u^3}{L}, \tag{2.7}$$

we obtain

$$\eta = \left(\frac{\nu}{u}\right)^{3/4} \left(\frac{L}{C_\varepsilon}\right)^{1/4}. \tag{2.8}$$

Additionally, we know that the Taylor-based Reynolds number is related to the large-scale Reynolds number $\text{Re} = uL/\nu$ by

$$\text{Re}_\lambda = 15^{1/2}C_\varepsilon^{-1/2}\text{Re}^{1/2},$$

which results in

$$\text{Re}_\lambda = \left(\frac{15uL}{C_\varepsilon \nu}\right)^{1/2}. \tag{2.9}$$

Similarly, the relation between the Kolmogorov timescale and the large scales of the flow is

$$\tau_\eta = \left(\frac{\nu L}{C_\varepsilon}\right)^{1/2} u^{-3/2}. \tag{2.10}$$

We will now use these relations to see whether an improved Hwang & Eaton [41] apparatus is possible with a larger Reynolds number.

When designing the new apparatus we have roughly two choices: either increase its size or increase the velocities. In order to see more clearly the effects of these changes, let us summarize the dependence of the key parameters

on L and u:

$$\text{Re}_\lambda \quad \propto \quad L^{1/2}u^{1/2} \tag{2.11}$$

$$\eta \quad \propto \quad L^{1/4}u^{-3/4} \tag{2.12}$$

$$\tau_\eta \quad \propto \quad L^{1/2}u^{-3/2}. \tag{2.13}$$

The first possible improvement would be to increase the size of the apparatus. We see in Eq. (2.12) that η has only a weak dependence on L, meaning η will remain approximately the same even after a considerable increase in the size of the chamber. This may be advantageous because the smallest observable η will depend on the spatial resolution of the experiment. Additionally, if our droplets are to be treated as point-particles, η should be much larger than the droplet diameter d_p. However, increasing the size may have a negative effect on the magnitude of the velocity at the center of the chamber since the distance from the jet orifice to the center will increase.

With increasing size, the Taylor-based Reynolds number increases proportional to $L^{1/2}$. At the same time, the Kolmogorov time scale also increases proportional to $L^{1/2}$, which may be disadvantageous for our phosphorescence method because of time limits placed by the lifetime of the solution.

Now let us assume that we keep the size of the apparatus the same and increase the velocities. Then, the Reynolds number will increase $\propto u^{1/2}$, and the Kolmogorov length scale η decrease $\propto u^{-3/4}$, which may bring a spatial resolution issue; but the timescale decreases strongly as $\tau_k \propto u^{-3/2}$, which is advantageous for our phosphorescence method. We conclude that the best way to improve the design of H&E's apparatus [41] is by increasing the velocity.

Increasing the velocities may be accomplished by using more powerful loudspeakers. However, accommodating these may clutter the apparatus, so a compromise must be sought. By taking twice as big loudspeakers, and assuming that the membrane movement is the same, the velocities become four times larger (if the size of the orifice remains the same). Therefore, τ_k can become eight times smaller, while η is reduced by approximately two-thirds. It can be easily shown that for water droplets in air ($\rho_p/\rho_{air} \approx 1000$), the relaxation time will be equal to the Kolmogorov time, i.e. St $= 1$, if the droplet diameter d_p and the Kolmogorov length scale fulfill

$$d_p \cong 0.135\eta,$$

therefore

$$d_p \cong 0.135\ L^{1/4}\ u^{-3/4}\nu^{3/4}C_\varepsilon^{-1/4}. \tag{2.14}$$

For the Hwang & Eaton [41] paper we thus find $d_p \approx 18\,\mu$m. With velocities four times larger, the droplet size becomes $d_p \approx 7\,\mu$m, which seems rather small. However, most probably, the limitation on droplet size is the phosphorescence intensity, which will be addressed in Chapter 4.

In conclusion, in order to have many smallest-eddy turnovers during the decay time of the phosphorescence, we should have large velocities with, consequently, small droplets. The final design of the turbulence chamber, shown in Figure 2.1 below, consists of a cubical box with a side length of 40 cm and eight speakers of 36.5 cm diameter (MTX Audio sub-woofer model RT15-04, Mitek Corporation, Phoenix, AZ, USA) each with an independent 145 Watt amplifier (model RN-2160, Rodek, Garden Grove, CA, USA). The jet orifice is 4 cm in diameter, and the box has four square windows ($20 \times 20\,\text{cm}^2$) for optical access.
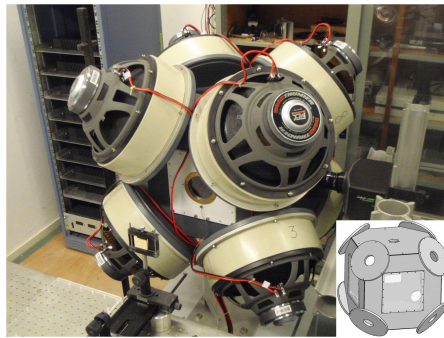
Figure 2.1: *Picture and CAD drawing (inset) of the final design of the turbulence chamber. The side length of the cubical chamber is* 40 *cm. It has eight synthetic jets which use* 36.5 *cm speakers and a jet orifice of* 4 *cm.*

2.1.2 Speaker control and balancing

As mentioned above, understanding of droplet behavior in isotropic, homogeneous, zero-mean flow turbulence is the goal of this study. The first step to achieve this is the creation of a flow with these characteristics. Synthetic jets fulfill the requirement of average momentum transfer while averaging zero mass transfer. This is possible due to the asymmetry in the flow around the orifice during the contraction and the expansion of the synthetic jet cavity. When the membrane contracts, the velocity profile at the jet's orifice resembles a top hat (Figure 2.2(a)), meaning that the mass ejected is traveling paral-

lel to the axis of the orifice. On the other hand, when the membrane expands, the air comes from all directions (Figure 2.2(b)).
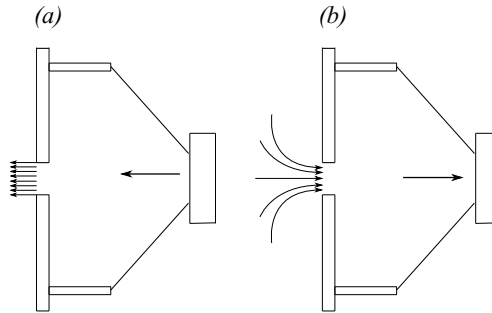
Figure 2.2: *The (a) contraction and (b) expansion of the membrane is an asymmetric process that allows for mean momentum transfer without mean mass transfer.*

The speakers are driven by creating an analog signal and sending this signal to an amplifier, which in turn is connected to the speakers. Several factors must be considered when creating the excitation signal. First, the maximum frequency a speaker can handle is limited by its dynamical response; subwoofers are especially suited for lower frequencies. Second, periodic signals are easy to produce, but any imbalances among the power of the jets will be more easily translated into a mean flow. Taking these two factors under consideration, the speakers are driven using colored noise, with the frequency of the color chosen near the resonance frequency of the speakers.

To generate the signal we use a 16-bit, 8-channel analog output card (16AO16, General Standards Corporation, Huntsville, Alabama, USA) with a 256 kS FIFO buffer. Our sampling frequency was 10 kS/s per channel, easily meeting the Nyquist criterion. The FIFO buffer allowed for data to be loaded as needed by the use of an interrupt. The buffer was filled with data and as the buffer reached the one-quarter flag, a new batch of data was fed through, achieving a seamless signal throughout the entire measurement.

The signal is obtained from uniformly distributed random numbers x_i^m created for each channel, where the subscript i denotes the sample number in time and m represents the channel number. To maintain a constant volume in the chamber these numbers are balanced at any given time by ensuring that $\sum_{i=1}^{M} x_i^m = 0$, which is done by subtracting the mean from x_i^m, $m = 1, \cdots, M$, with M being the total number of active channels. The consequence is that at each given time the numbers x_i^m are correlated. Next the time series is

convolved with a filter function to produce the samples y_i^m of the output signal

$$y_i^m = \sum_{k=-N}^{N} a_k x_{i-k}^m, \tag{2.15}$$

with $a_k = F(kt_s)$ where t_s is the sample time and the filter function

$$F(t) = \frac{1}{\sigma\sqrt{2\pi}} \exp\left[\frac{-t^2}{2\sigma^2}\right] \sin(2\pi f_0 t). \tag{2.16}$$

Here σ represents the Gaussian width and f_0 the central frequency. Since x_i^m is balanced, so is y_i^m. Further, since the spectrum of the random numbers is white, the spectrum of the balanced driving signal is the Fourier transform of Eq. 2.16,

$$\widetilde{F}(f) = \exp\left[-(2\pi)^2(f-f_0)^2\frac{\sigma^2}{2}\right]. \tag{2.17}$$

In Figure 2.3 we illustrate the filtering procedure. Through the 'color' of the signal it is possible to drive the jets near a particular frequency, for example the resonant frequency f_r. For our speakers, $f_r = 20$ Hz, however, we did not drive the jets using this frequency because the jet velocity increase had a negative effect on the homogeneity of the flow.
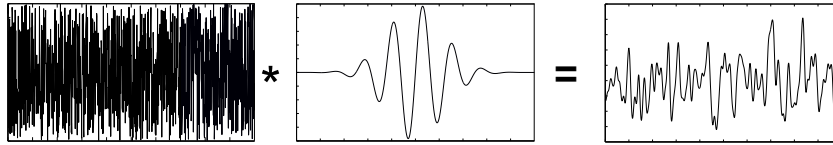
Figure 2.3: *The driving signals for the speakers were obtained by convolving a vector of random numbers with a Gaussian modulated sine wave of frequency f. Shown signals are in arbitrary units.*

After prolonged use, the temperature of the speakers and amplifiers may considerably rise, changing the resistance of the speaker coil, in turn affecting the stationarity of the turbulent flow due to changes in the response of the speaker membrane. To avoid these displacement fluctuations, 80 mm cooling fans were installed on the amplifiers and speakers. The cooling allowed the system to reach a steady temperature after approximately 15 minutes of continuous use. Before a set of measurements was performed, the speakers were

allowed to reach a stable temperature by running the system for an appropriate time span.

Several steps were taken to balance the speakers in order to create a flow with the lowest possible mean velocity. The first step was to ensure the *rms* output signal from the amplifiers was constant for a sinusoidal input. This was achieved by manually adjusting the gain for each amplifier. Even after this adjustment, possibly due to manufacturing inconsistencies, the velocity field was not balanced. The second step towards balancing the flow consisted of measuring the displacement of the speaker membrane using a high-precision CMOS displacement sensor with a resolution of $10\,\mu$m. The difference in the measured displacement of each speaker was used to correct the driving signal, but due to small, unavoidable inconsistencies in the mounting procedure of the speakers, the resulting velocity fields were still considerably unbalanced.

Given the failed attempts to systematically balance the flow, it was necessary to do a trial-and-error balancing approach by adjusting the input signal and measuring the flow characteristics using particle image velocimetry (PIV) and iterating on this procedure until satisfactory results were achieved. We used the results from the membrane displacement measurements as initial guesses. The results of the PIV measurements will be addressed in the following section.

2.2 Flow characterization

In an experiment we must characterize the inertial-range properties of the turbulent flow. Since developed turbulence is scale-independent, instrument resolution should not matter. Nevertheless, in this experiment we are interested in droplet statistics on the smallest scales, which we would like to measure directly. However, we will show later that the resolution of the PIV technique falls short to actually resolve the smallest scales; so we must either extrapolate measured gradients to smaller scales, or resort to inertial range quantities combined with known scaling behavior. Before we describe these methods, let us briefly summarize the techniques of velocimetry and their limitations.

A common technique used in turbulence, due to its unparalleled time resolution and its maturity, is hot-wire anemometry. This technique can measure the velocity at a fixed point in space, and is consistently used in flows that have a mean velocity, such as wind tunnels, pipe flows and water channels. Unfortunately, the intrusive nature of this technique, together with the in-

ability to distinguish between back and forward flow, render this technique inappropriate for our particular setup.

There exist several non-intrusive techniques that rely on optical measurement of the flow through the use of seeding particles that are sufficiently small to act like fluid tracers. One of such optical techniques is laser-Doppler anemometry (LDA). The point-like nature of this diagnostic comes paired with advantage of high spatial resolution. Unfortunately, resorting to this technique would translate into a prohibitive number of measurements to evaluate a velocity field of area $\sim 10\,\mathrm{cm}^2$.

Phase-Doppler anemometry (PDA) works in a similar fashion as LDA, but presents an attractive addition when it comes to particle-laden flows: it is capable of measuring both the velocity and the particle diameter at a point in space. Similarly it suffers from a point-like nature. Moreover, multiple diffraction in dense particle suspensions may degrade the quality of the data. For an in-depth review of LDA and PDA, the reader is referred to [46].

Thanks to the progress in imaging tools over the past two decades, a couple of two- and three-dimensional methods have gained popularity, being now commonplace in many fluid dynamics laboratories. These are particle tracking (PTV) and particle image velocimetry (PIV). PTV has the capability of measuring particle tracks in two or three dimensions with good spatial resolution. It has greatly enhanced the ability of fluid dynamicists to learn about Lagrangian properties of flows. In order to accurately track particles, it is necessary to have a data rate comparable to the shortest timescales of the flow, resulting in the need for a high repetition laser, which is not available in our laboratory.

PIV is the Eulerian counterpart of PTV, which offers the possibility of directly measuring full velocity fields in two or three dimensions, depending on the particular equipment available. A downside of PIV is that its resolution is not sufficient to resolve the smallest scales in a turbulent flow. Fortunately, a few methods, which will be addressed below, have been proposed to overcome this limitation. In what follows, we will give a brief summary of the working principle of this diagnostic technique. For an extensive treatise, the reader is referred to [47, 48], where the capabilities and limitations of almost every variant of particle image velocimetry are reviewed.

Briefly, the procedure consists of the measurement of the average displacement of tracers inside the flow, which is done by imaging tiny particles or droplets at two slightly different times (with a known time difference Δt) and correlating small regions—known as interrogation windows—of the im-

age pair to determine the average velocity within each region (see Figure 2.4). The size of the interrogation window must be large enough so that it at least contains a few particles. However, the flow velocity is an average over the interrogation window. This imposes a limit on the smallest resolved scale.
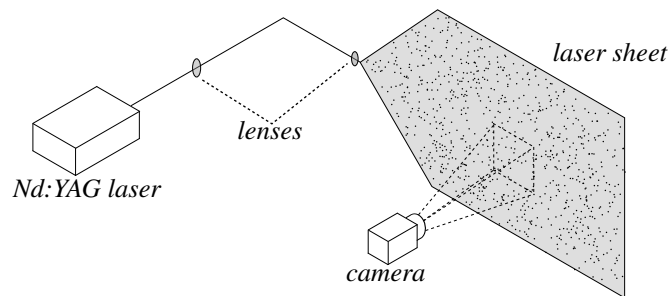
Figure 2.4: *Schematic representation of particle image velocimetry (PIV). A pulsed Nd:YAG laser is used to illuminate tracers in the flow at two distinct times with a known time delay Δt. Lenses are used to transform the laser beam into a thin sheet. The images are then divided into small interrogation windows (e.g. 32×32 pixels), which are correlated to obtain the average velocity within the interrogation region. This procedure is repeated for the entire image to obtain the full velocity field.*

Many variations of the method have been developed to increase the data yield, e.g. stereoscopic PIV measures three components of the velocity field in one plane, while tomographic PIV is able to measure the three components in a volumetric region. From the simplest 2D PIV to the more complex variations, the use of interrogation windows inherently filters scales smaller than the size of these regions (Δ). In many instances Δ falls well within the inertial range of the flow, making it difficult to directly calculate crucial quantities such as the energy dissipation rate ε. Sheng et al. [49] proposed a procedure based on the Smagorinsky model [50] that allows for the calculation of sub-grid stresses. Using the scaling properties of turbulence, the energy dissipation rate can also be estimated from the second- and third-order structure functions which can be calculated using PIV data.

Our PIV setup used consisted of a dual-head Nd:YAG laser (CFR400, Quantel, Les Ulis, France) and a 1600×1200 pixel^2 digital camera (ES2020, Princeton Instuments, Trenton, NJ, USA). Seeding for the PIV measurements was done with a commercial smoke generator capable of producing droplets

of approximately 1 μm. The field of view was approximately 60×80 mm^2 (resulting in a magnification of 20 pixel/mm); the sampling rate was 15 Hz. The processing was done with commercial software (PIVtec, Göttingen, Germany) with a 32 × 32 pixel interrogation area with a 50% overlap. Even though the magnification of the optical setup results in a spatial resolution of 25 μm/pixel, we have seen above that a filtering effect is introduced by the averaging over interrogation regions. The resulting distance between grid points is approximately 5η, yet the resolution is set by the windows size and is twice that value. For every case analyzed, approximately 1500 PIV samples (3000 images) were acquired. The acquisition was performed in batches of 300 images due to the decline of tracer concentration over a span of approximately 10 seconds. Before every recording, an appropriate quantity of smoke was injected into the chamber, and after homogenisation of the tracer concentration, the recording was started.

2.2.1   Large-eddy PIV

As we have seen above, PIV has a spatial filtering effect on the velocity field. If, hypothetically, we reduced our field of view to, say, 16× 12 mm^2, a laser timing issue could arise due to the requirement that particles displace no more than one-third of the size of the interrogation window. Taking the worst case scenario of velocity fluctuations of 6 m/s, the maximum acceptable time delay between our images $\Delta t =$17 μs, which is not attainable with the available laser. Furthermore, the spatial resolution of the velocity field would still be five times larger than the Kolmogorov length scale.

Given such resolution issues, methods to circumvent this limitation have been devised. Let us assume we have a PIV velocity field to measure the small scale turbulence properties. The turbulent kinetic energy at a point (x_1, x_2) in the plane of measurement is given by

$$q^2(x_1, x_2) = \left\langle \sum_{i=1}^{3} u_i^2(x_1, x_2) \right\rangle \tag{2.18}$$

where $\langle \cdot \rangle$ denotes the ensemble average and u_i is the fluctuating component of the velocity.

Because 2D PIV yields only the u_1 and u_2 components of the velocity,

then, by assuming isotropy, Eq. (2.18) can be written as

$$q^2(x_1, x_2) = \frac{3}{2}\Big\langle \sum_{i=1}^{2} u_i^2(x_1, x_2) \Big\rangle. \qquad (2.19)$$

Based on the isotropy assumption, the out-of-plane velocity u_3^2 should have on average the same magnitude as the average in-plane fluctuations u_1^2, u_2^2. In the case only u_3 can be measured,

$$q^2(x_1, x_2) = 3\Big\langle u_3^2(x_1, x_2) \Big\rangle. \qquad (2.20)$$

Given that the spatial resolution of PIV is not high enough to measure the smallest turbulent scales, a trick must be used to correct for the unresolved motion. This trick consists of defining the stress as in the Smagorinsky model [50], expressing it in the resolved gradients. Thus,

$$\varepsilon(x_1, x_2) \approx -2\Big\langle \tau_{ij}(x_1, x_2)\widetilde{S}_{ij}(x_1, x_2) \Big\rangle, \qquad (2.21)$$

with

$$\widetilde{S}_{ij}(x_1, x_2) = \frac{1}{2}\left(\frac{\partial u_j(x_1, x_2)}{\partial x_i} + \frac{\partial u_i(x_1, x_2)}{\partial x_j} \right), \qquad (2.22)$$

where $\widetilde{S}_{ij}$ is the filtered strain measurement, and where the sub-grid stress τ_{ij} is estimated from the Smagorinsky model

$$\tau_{ij}(x_1, x_2) = -C_s^2 \Delta^2 \left| \sqrt{2\widetilde{S}_{ij}(x_1, x_2)\widetilde{S}_{ji}(x_1, x_2)} \right| \widetilde{S}_{ij}(x_1, x_2), \qquad (2.23)$$

where $C_s = 0.17$ is the Smagorinsky constant and Δ is the spatial resolution of the velocity vectors. This spatial filtering is determined by the linear dimension of the interrogation window. This application of the Smagorinsky [50] model has been used to calculate the sub-grid stresses in PIV data and is described extensively by Sheng [49], and compared to other methods by de Jong et al. [51].

2.2.2 Estimating ε from structure functions

For inertial-range separations r, the second- and third-order structure functions in homogeneous isotropic turbulence should behave as

$$G_2(r) \;=\; C_2 \varepsilon^{2/3} r^{2/3} \tag{2.24}$$

$$G_3(r) \;=\; -\frac{4}{5}\varepsilon r. \tag{2.25}$$

We see that the value of the dissipation rate can be calculated from the structure functions given the measured G_2 and G_3 structure functions. These functions are available from the PIV data, which allows us to estimate the dissipation rate and compare its value to that obtained from the Large-eddy PIV method.

2.3 Characteristics of turbulent flow

It is our aim to understand the effect inertia has on the dynamics of droplets suspended in the flow. We will explore different Stokes numbers by changing the droplet size while maintaining constant turbulence. As will be explained in Chapter 3, we generate droplets using a spinning disk aerosol generator (SDAG), which creates a parasitic flow. Therefore, it is necessary to balance the speaker power according to the perturbation introduced by the spinning disk. PIV was performed for each of the five cases, with all of them resulting in relatively similar characteristics. Each one of the cases corresponds to a different Stokes number.

2.3.1 Turbulence statistics

Table 2.2 presents a summary of the turbulence statistics for every case as well as those for Hwang & Eaton's [41] for comparison. It can be seen that the average turbulent velocity fluctuations have more than doubled compared to H&E, and that, similarly, the Taylor-based Reynolds number had a proportional increase.

Another notable aspect of the turbulent statistics is the elevated value of the energy dissipation rate ε. This result was first calculated using the Large-eddy PIV method proposed by Sheng [49], and later validated using the second-order structure function. While not in perfect agreement, both

	Present Study Case					Hwang and
	1	2	3	4	5	Eaton (2004)
$\langle u \rangle$ (m/s)	1.95	2.06	2.08	2.03	2.04	0.9
ε (m²/s³)	71.9	60.7	58.7	53.9	55.3	11.3
Re_λ	448	548	563	562	560	218
τ_η (μs)	457	497	505	527	521	1160
η (μm)	83	86	87	89	88	132
d_p (μm)	11.0	15.4	16.5	18.8	21.9	—
St	0.95	1.67	1.86	2.43	3.15	—

Table 2.2: *Comparison between turbulence statistics of H&E [41] and the five cases of the present study.*

methods were consistent to within 20%. It was noted by de Jong [51] that the LEPIV method usually overestimates the value of ε, while the converse is true for the second-order structure function; this is consistent with our findings.

As seen in the contour fields of the magnitude of the velocity fluctuations (Figure 2.5), the homogeneity of the flow within the measurement window is substantial. A subtle pattern emerges in the field where the highest values appear in the center, while the magnitude decreases as we move towards the edges. However, we see that the magnitudes range between 2.7 and 3.1 m/s, which is within approximately ten percent of the average magnitude.

It must be noted that the region of interest for the phosphorescent tagging experiments is approximately 30×30 mm², which is why the velocity fields show a smaller area than that described earlier. Outside of this window the homogeneity is reduced substantially, with the turbulent velocity fluctuations further decreasing in magnitude away from the center. We believe this is a result of the size of the jet orifice diameter and the short distance from the orifice to the center of the box. Unfortunately, the jet orifice could not be increased due to the design of the chamber. Several attempts were made to break the large scales of the flow by placing obstacles, i.e. crosses and wire mesh, in front of the orifice. However, the effect on the homogeneity of the flow was low, while these objects considerably reduced the velocity fluctuations.

An opposite scenario was seen in the mean velocity fields, where higher values were observed around the edges. The mean velocity fields of all five cases are shown in Figure 2.6. It can be seen that, in comparison with the total
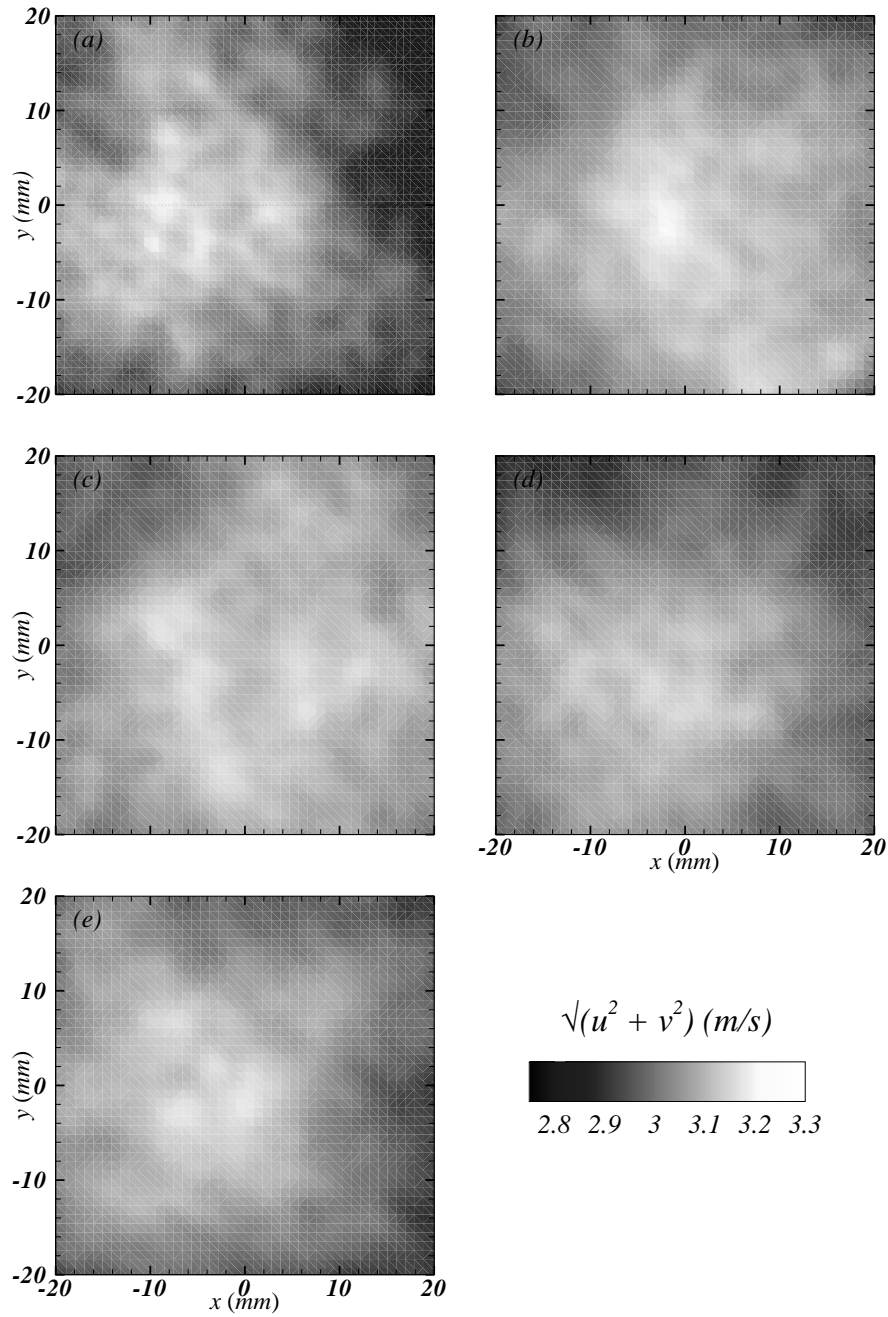
Figure 2.5: *Contours of the magnitude of the velocity fluctuations, (a)–(e) for cases 1–5, respectively. All four velocity fields present a high degree of homogeneity.*
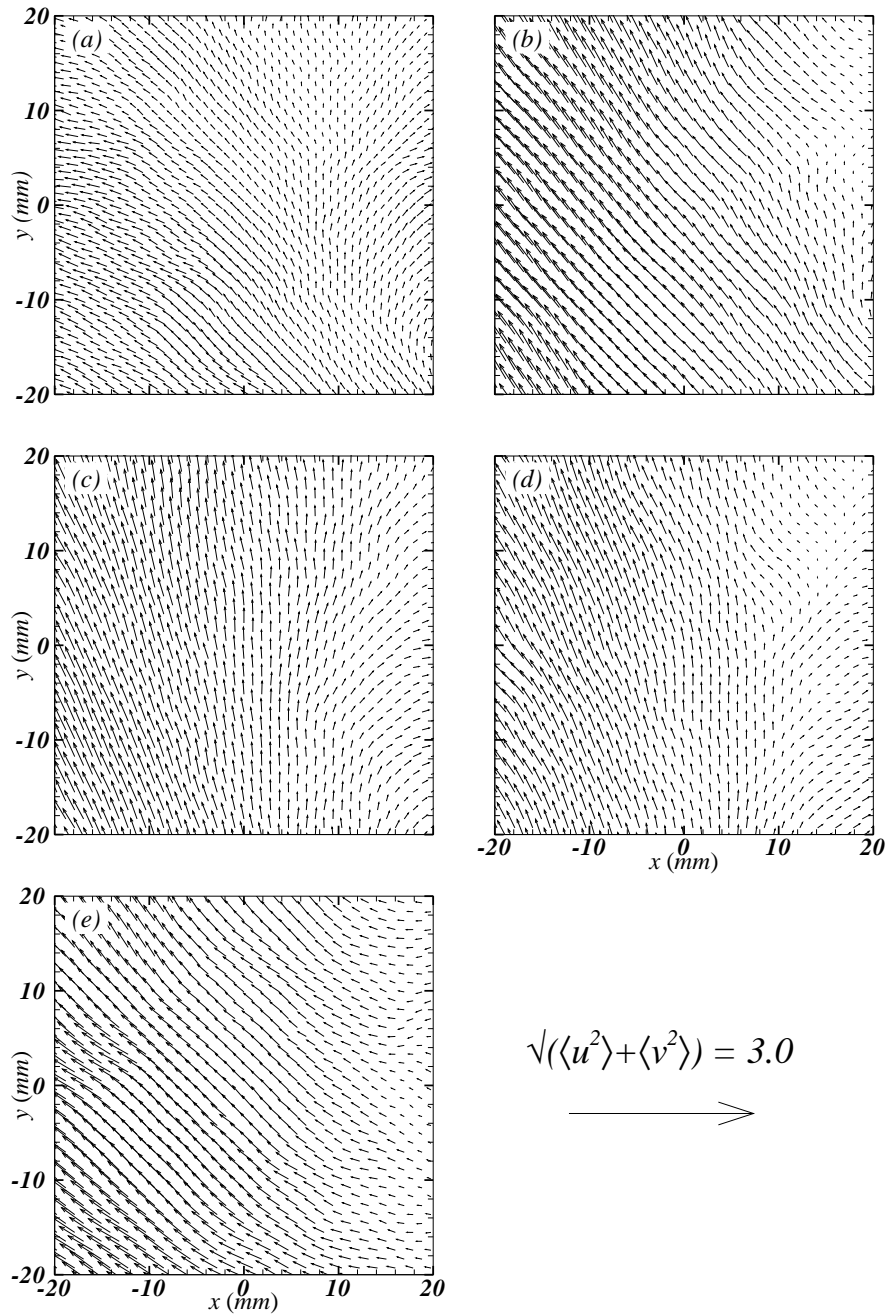
Figure 2.6: *Velocity fields for cases 1–5. The reference vector has a magnitude of $\sqrt{u^2 + v^2} = 3.0$ m/s. It can be seen that the mean velocity is much lower than the average velocity fluctuations.*

magnitude of the velocity fluctuations, the mean velocity field is much lower (approximately one-tenth of the turbulent velocity fluctuations).

2.3.2   Structure functions

The structure functions of the turbulent flow provide important information about its isotropy. Additionally, we can use them to estimate the energy dissipation rate ε of the flow. Our PIV system only provides two components of the velocity, yet it is important to ensure isotropy and homogeneity of the three components. Information about the statistics in the z-direction was obtained by rotating the turbulence chamber 90 degrees and repeating the PIV measurements. Given the similarity of turbulent statistics of the five different cases, this measurement was only performed for case 2. The data obtained for the four other cases in the xy-plane displays similar characteristics as case 2, therefore we do not expect the values in the z-direction to change considerably.

Structure functions encompass small (inertial-range) to large scales. Inhomogeneity affects the large scales, this is especially so for the third-order structure function. Therefore, we have normalized the velocity field by its local *rms* value, $u'(x, y) = u(x, y)\langle\langle u^2(x, y)\rangle\rangle_{x,y}^{1/2}/\langle u^2(x, y)\rangle^{1/2}$, so that $\langle u'^2(x, y)\rangle^{1/2}$ is everywhere the same, and similarly for v. As expected, this affected most the third-order structure function. The resulting structure functions are shown in Figure 2.7. From $G_2(r) = C_2\varepsilon^{2/3}r^{2/3}$ we derive $\varepsilon = 72.9$ m^2/s^{-3}, while from $G_3(r) = -\frac{4}{5}\varepsilon r$ we find $\varepsilon = 65.9$ m^2/s^{-3}; values that compare well to that found from our direct measurement of the gradients, $\varepsilon = 75.8$ m^2/s^{-3}. Our results appear to be in agreement with the comparison made by de Jong et al. [51], with large-eddy PIV consistently giving a higher value for the dissipation rate, and the converse being true for the structure functions. We also find that the large-scale isotropy u/v of the flow is excellent, as is shown in Figure 2.7(d).

In general, structure functions depend both on the velocity component involved and on the direction of the separation vector. In isotropic turbulence there are two distinct second-order structure functions, the transverse $G_{xx}^y(r)$ and $G_{yy}^x(r)$, and the longitudinal $G_{xx}^x(r)$ and $G_{yy}^y(r)$. We have

$$G_{xx}^x(r) = \langle(u_x(\boldsymbol{x} + r\boldsymbol{e}_x) - u_x(\boldsymbol{x}))^2\rangle, \qquad (2.26)$$

and similarly for $G_{yy}^y(r)$. Likewise,

$$G_{xx}^y(r) = \langle (u_x(\boldsymbol{x} + r\boldsymbol{e}_y) - u_x(\boldsymbol{x}))^2 \rangle, \tag{2.27}$$

and similarly for $G_{yy}^x(r)$.

Figure 2.7: *Relevant turbulence characteristics for the PIV measurements in the xy-plane. (a) Second-order longitudinal structure functions in the x- and y-direction. (b) Third-order structure functions in the x- and y-direction. (c) Contour field of the magnitude of the velocity fluctuations. (d) Contour field of u/v. (e) Isotropy calculated using Eq. (2.28). (f) Ratio between x and y structure functions.*

The values of transverse functions should be the same, and so should the longitudinal ones. Incompressibility then dictates the following relation between longitudinal G_2^L and transverse G_2^T structure functions,

$$G_2^T(r) = G_2^L(r) + \frac{r}{2}\frac{\mathrm{d}}{\mathrm{d}r}G_2^L(r), \qquad (2.28)$$

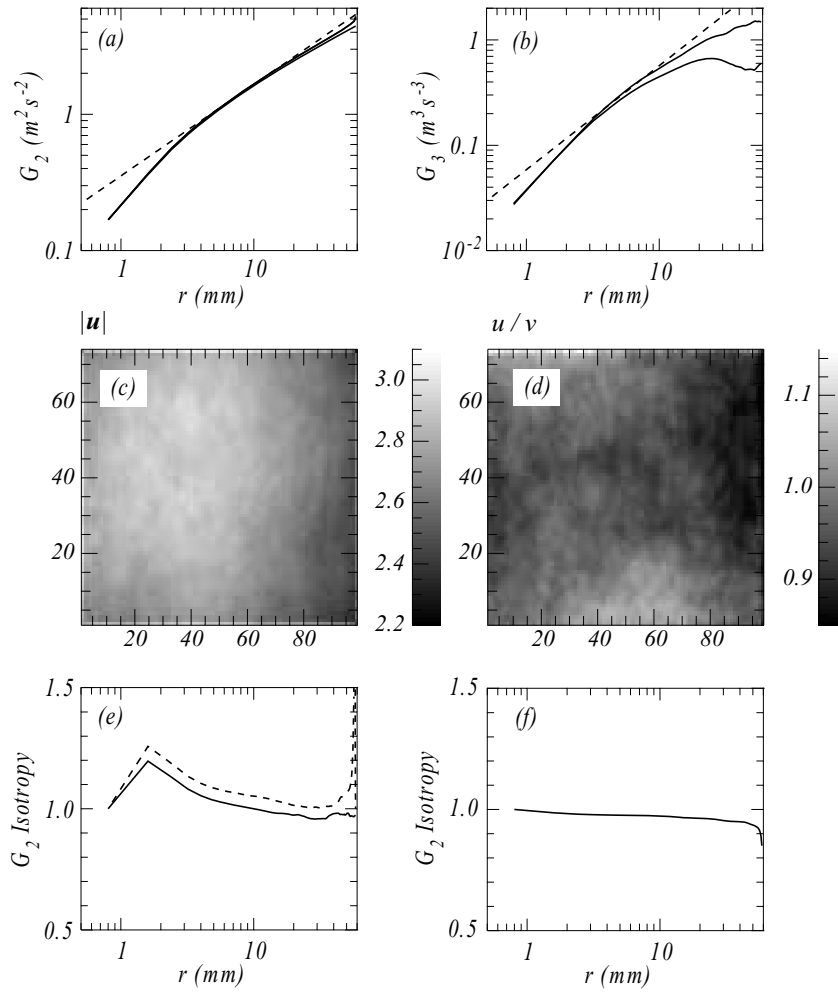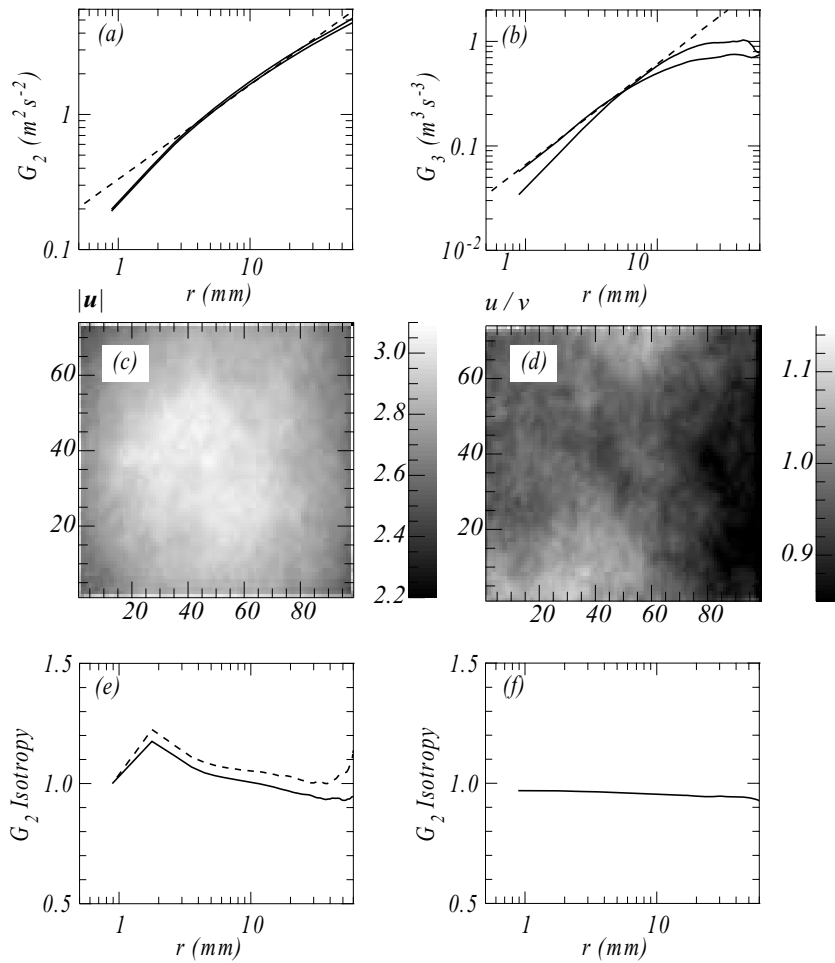**Figure 2.8:** *Relevant turbulent characteristics for the PIV measurements in the yz-plane. (a) Second-order longitudinal structure functions in the y- and z-direction. (b) Third-order structure function in the y- and z-direction. (c) Contour field of the magnitude of the velocity fluctuations. (d) Contour field of u/v. (e) Isotropy calculated using Eq. (2.28). (f) Ratio between y and z structure functions.*

where G_2^T is $G_{xx}^y(r)$ or $G_{yy}^x(r)$ and G_2^L is $G_{xx}^x(r)$ and $G_{yy}^y(r)$.

A good way to measure the small-scale anisotropy is a test of the isotropy relation for the second-order longitudinal and transverse structure functions. In Figure 2.7(e) we plot the ratio $G_2^T(r)/(G_2^L(r) + \frac{r}{2}\frac{\mathrm{d}}{\mathrm{d}r}G_2^L(r))$, for both directions of the separation vector, while in Figure 2.7(f) we plot $G_{xx}^x(r)/G_{yy}^y(r)$. We conclude that the turbulence is isotropic at both large and small scales.

2.3.3 Integral length and timescale

Even though an increased effort by the scientific community has been devoted to generate homogeneous isotropic turbulence with zero mean flow, an important anomaly is encountered in the calculation of the integral length scale of the flow. Supported by the available literature [41]–[44], [52] and by our own experience, we see that in such flow facilities this length scale appears to be considerably, or in some cases, much larger than the homogeneous isotropic region of the flow. Moreover, the measured correlation functions do not reach zero, so the integral length scale must be estimated indirectly. This is the case for Hwang & Eaton's experiment [41], where it was not possible to obtain the integral length scale from the correlation function, and an estimation has to be made using the kinetic energy and the dissipation rate. Chang et al. refer to a large-eddy turnover time as they use extended self-similarity to calculate scaling exponents of the structure functions, however, the value is not supplied. The same apparatus was used in the study by Bewley et al. [52], where the transverse correlation function R_{ii}^T was measured using LDV. From the relation between the longitudinal and transverse correlation functions [53],

$$R_{ii}^T = \frac{1}{2}\left[R_{ii} + \frac{\mathrm{d}}{\mathrm{d}r}\left(rR_{ii}\right)\right], \tag{2.29}$$

it can be easily shown that the longitudinal integral length scale is twice the transverse. We can then estimate the longitudinal integral length scale in [52] to be $L_{11} = 160$ mm, which is considerably higher than the homogeneous region given in [43] (≈ 100 mm).

Goepfert et al. [44] were able to obtain an integral length small enough to fit within their measurement area (40 mm). We see two possible causes for this (which need not be exclusive): the open setup—as opposed to a closed chamber—and the use of perforated sheet to create an array of small jets. The latter, we believe, limits the size of the larger length scales, however, it has a negative impact on the Reynolds number.

In the present study we estimate the integral length scale L by fitting an exponential function to the tails of the correlation function, as shown in Figure 2.9. We find $T_{xx} = 77.5$ mm and $T_{yy} = 80$ mm.

The reason for such large values of the integral length scale remain unclear, although we expect the walls of the chamber, and the size of the jet orifice as well as the distance from the orifice to the center likely playing a role. In the present study, we are interested in the dynamics of droplets at the smallest scales, thus we do not foresee any considerable effect. However, in studies were integral time- and length scales are of interest, this issue must be addressed.
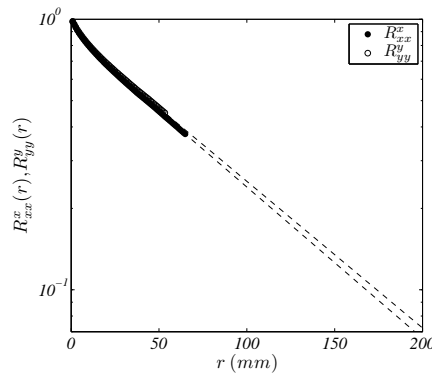
Figure 2.9: *Plot of the measured correlation functions R^x_{xx} and R^y_{yy} (symbols) and corresponding fits (dashed). The estimated integral length scale is approximately 80 mm. This is considerably higher than the region of homogeneity and may be due to wall effects or the forcing mechanism.*

2.4   Conclusion

Throughout this chapter, we presented three options for the design of a turbulence chamber and the characterization of the flow within it. We reviewed scaling relations of turbulent flows in order to improve on an earlier design by Hwang & Eaton [41]. After analyzing the scaling relations of turbulence we decided to increase the size of the speakers in order to increase the Reynolds number. Additionally, we explained the algorithm used to create the driving signal for the synthetic jets. A brief description of the available techniques for velocity measurement was given, and the working principle of particle image

velocimetry was described in further detail. Furthermore, the experimental setup used to characterize the flow in the turbulence chamber was illustrated.

The results of the PIV measurements demonstrate that we have indeed been able to generate homogeneous, isotropic turbulence with a considerably reduced mean flow and an increased Re_λ, establishing the functionality of the experimental facility. The isotropy of the flow was determined in several different ways: we did so by comparing the longitudinal structure functions in all three directions and by looking at the relationship between the longitudinal and transverse structure function in homogeneous isotropic turbulence (Eq. (2.28)). Finally we tested the isotropy in the large scales by comparing the velocity fields of the components of the velocity fluctuations u and v.

With this in mind, we will now proceed to give a detailed explanation of the droplet generation and characterization in the following chapter, and an explanation of the phosphorescent tagging technique thereafter.

CHAPTER 3

AEROSOL GENERATION AND CHARACTERIZATION

The generation and characterization of particles and droplets is essential for industrial and scientific purposes. On a day-to-day basis we rely on the creation of aerosols for processes as trivial as hairspray application or as sensitive as medication dispensing through inhalers and nebulizers. Since the characteristics of aerosols play a crucial role in the transport of droplets, a reliable generation process is essential.

Monodisperse aerosols can simplify the analysis of particle-laden flows, e.g. fundamental studies of droplet behavior in turbulent flow, where, ideally, a single Stokes number should characterize the droplets. There exist several types of devices to produce a collection of monodisperse droplets: vibrating orifice, flow focusing and spinning disk aerosol generators. The first two offer a very narrow distribution of droplet sizes with the drawback of single droplet production rate. The advantage of the spinning disk droplet generator is that large amounts of droplets can be produced simultaneously. Briefly, fluid is applied near the center of a fast spinning disk, wetting its surface completely. Due to the centrifugal force, fluid ligaments are ejected tangentially from the disk rim. These ligaments break up into a primary droplet and a few satellite droplets of smaller diameter. All primary droplets have approximately the same diameter, which is determined by the angular velocity of the disk, the fluid density and its surface tension. The principle of the spinning disk gen-

erator is well established [54]–[56], yet little is known about the particle size distribution function (PDF).

A few techniques exist to measure droplet sizes and their PDFs, of which interferometric particle imaging (IPI) is quite attractive because of its relatively simple setup. Other optical techniques are direct microscopic vision, which suffers from the small field of view of microscope objectives, and phase-Doppler anemometry, which provides a simultaneous measurement of the droplet size and velocity at a single point in space.

The purpose of this chapter is to give an overview of the droplet generation and characterization methods used in our study. In Section 3.1 we present the background and theory of IPI. Additionally, we present an algorithm for image analysis for interferometric particle imaging with an emphasis on a reliable measurement of particle size distribution functions, which is tested using synthetic images. In Section 3.2 we explain the working principle of spinning disk aerosol generators and present the characteristics of our experimental setup. Next (Section 3.3), we present the resulting PDFs obtained using our novel processing algorithm and compare our findings with available literature. We give concluding remarks of the chapter in Section 3.4.

3.1   Interferometric particle imaging

IPI, first proposed by König et al. [57] and Ragucci et al. [58], presents particularly convenient characteristics when compared to other methods: it has the capability of yielding two-dimensional data while most other available methods are point measurements. Additionally, the only necessary equipment is a reasonably coherent light source and a camera. In cases where droplets have relatively high velocities, the use of a pulsed light source is required to 'freeze' the particles.

3.1.1   Background

The scattering of coherent light off a droplet results from interference between light wavefronts passing over and through the droplet. However, for droplets larger than the wavelength of light, the picture can be simplified to rays originating from two glare points, one corresponding to a reflected ray, and one to a ray which is refracted twice. This creates a difference in the optical path, introducing a phase shift between the two rays. The shift creates an interfer-

ence pattern where each fringe translates into a full wavelength difference in the path travelled. A derivation of the difference in optical path lengths of these two rays can be found in Albrecht et al. [46].

When the diameter of large droplets is being measured, counting fringes can be a simple and relatively accurate method of interpreting the data. The number of fringes N_{fr} is related to the droplet diameter d_p by

$$N_{fr} = \frac{d_a d_p \mathrm{A}}{2\lambda v} = \frac{\Delta\theta_r}{\Delta\varphi} \tag{3.1}$$

where d_a is the aperture diameter, v is the object distance, λ is the wavelength of the incident light and $\mathrm{A}(\theta_r)$ is a geometry-dependent factor defined as

$$\mathrm{A}(\theta_r) = \left(m\cos\left(\theta_r/2\right) + \frac{m\sin\left(\theta_r/2\right)}{\sqrt{m^2 + 1 - 2m\cos\left(\theta_r/2\right)}} \right), \tag{3.2}$$

with m the relative refractive index and θ_r the angle between the incident light and the optical axis of the setup. $\Delta\theta_r$ is the total angle swept by the interference pattern, and $\Delta\varphi$ is the angular period of the interference fringes. It is important to differentiate between θ_r and $\Delta\theta_r$.

As droplets decrease in size, a higher resolution is necessary to accurately measure their diameter. The discreteness of fringe counting limits the resolution with which we can measure droplet sizes, since it is not uncommon to encounter fractions of fringes, which are hard to quantify. A better resolved analysis can be obtained by measuring the wavelength of the interference pattern λ_I.

The geometric arrangement of IPI is sketched in Figure 3.1(a). The angular separation $\Delta\varphi$ of the fringes is determined by the optical path length difference of the two scattered rays,

$$\Delta\varphi = \frac{2\lambda}{\mathrm{A}(\theta_r)d_p}. \tag{3.3}$$

If these rays have equal intensity, the visibility of the fringes is maximal. In general, the contrast depends on the scattering angle θ_r and the polarization of the light. For water droplets with a diameter $d_p \simeq 20~\mu$m the optimal angles are $\theta_r \approx 100°$ and $\theta_r \approx 70°$ for parallel (p) and perpendicular (s) polarization, respectively.

Angular information of scattered light is obtained from out-of-focus imaging, with the optical arrangement sketched in Figure 3.1(b). In this arrangement, particle images are circular spots with diameter d_i determined by the

location of the object plane and the size d_a of the lens aperture. The intensity in the spots is modulated by fringes.

If x is an image coordinate, the fringe spacing Δx is

$$\Delta x = (d_i/d_a)v\Delta\varphi. \tag{3.4}$$

Since x and d_i can be measured in pixels, the only additional information needed is the size d_a of the lens aperture and the object distance v. Roughly, the particle size is proportional to the number of fringes observed in a droplet image. Counting fringes provides the droplet sizes on a discrete scale. However, in our method, we will use the detailed intensity information, which, in principle, allows us to quantify the size of particles that produce less than two fringes. Nevertheless, particle size measurements benefit from large spatial fringe frequencies.

In order to have many fringes in a particle image, v must be small and d_a must be large (Eq. (3.1)). As the size of the out-of-focus images is determined by the lens aperture, dense droplet clouds lead to many overlapping particle images. An analysis regarding the optical limits of particle concentration is given by Damaschke et al. [59], where they introduce the overlap coefficient γ_o. We are interested, in particular, in the effects of overlap on the PDF of the droplet diameters. A few adaptations have been proposed in order
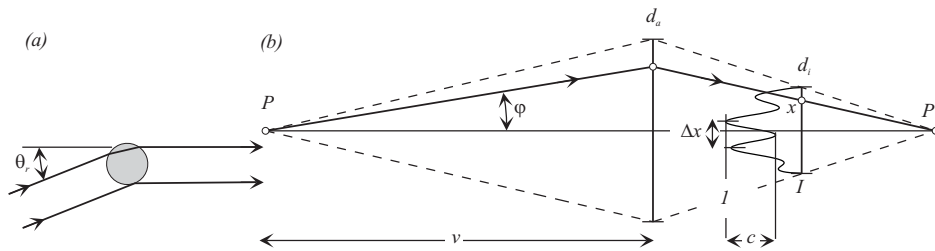
Figure 3.1: *(a) Geometric arrangement of interferometric particle imaging. (b) Schematic of the optical arrangement of IPI for a droplet positioned at the optical axis. The point P represents the position of the particle, v is the object distance, φ is an angular coordinate, with $\Delta\varphi$ (Eq. (3.3)) the angular fringe separation, while Δx is its linear counterpart. The focused image plane lies at point P'. The interference pattern has spot diameter d_i, and the aperture diameter is d_a. If the maximum intensity in the fringes is 1, c determines the fringe contrast.*

to optically alleviate this issue. Maeda et al. [60] suggested the optical compression of images along the axis parallel to the interference pattern, which resulted in thin ellipsoids and a reduced probability of overlap. Hardalupas et al. [61] used a rectangular mask together with a cylindrical lens, resulting in narrow, rectangular interference patterns. This approach allows for a larger droplet density, and also allows for the association of the size and position of a droplet. In this way the simultaneous measurement of size and velocity is possible using two cameras, one operating in-focus and the second one operating out-of-focus. However, it is our experience that if thin, rectangular interference patterns were to overlap, distinguishing one from the other becomes a challenging task.

The sphericity of the droplets and particles can also affect the accuracy of the results. Dehaeck & Beeck [62] looked at the influence of bubble deformation on their size determination, and discussed other sources of error such as the tilt angle of the deformed droplet and the uncertainty arising from the angle θ_r and the refractive index m. In our particle size range, however, we do not expect particle deformation since the droplets are much smaller than any length scale of the flow, and their velocities within the measurement volume are relatively low.

3.1.2 Image processing

It is relatively simple for a human to visually identify an interference spot and measure its wavelength. As the quantity of data increases, however, it becomes cumbersome to do this manually, so a reliable processing algorithm is necessary. Analysis of the fringe spacing in many particle images provides the probability distribution function of the particle sizes. The measurement of this PDF is the prime goal of this section. A key question is the influence of particle overlap. Several methods have been proposed that achieve automated data processing, but details regarding the algorithms have not been provided. Kawaguchi et al. [63] proposed the use of a Fourier transform method similar to that used in phase-Doppler anemometry, i.e. a one-dimensional signal in which a Gaussian fit to the Fourier spectrum is used to find the peak in the wavenumber space. An alternative proposed by Hardalupas et al. [61] is the automatic processing of the data using the continuous wavelet transform, which has the advantage of locality over its Fourier counterpart. The large scales of the wavelet transform were used to identify particles, whereas the small scales revealed the fringe spacing.

Inspired by this method, we will use a hybrid algorithm in which a single wavelet is used to locate the particle image, but where the particle size is inferred from a detailed representation of the fringe pattern. Let us now describe the steps taken in the image analysis. We will then test our method on simulated images with a prescribed PDF, and finally show the results of an IPI measurement on calibrated glass spheres.

The purpose of the image processing is to locate the particle images, determine the spatial frequency of the fringes within each particle, and make a histogram of particle sizes from the measured spatial frequencies. As each particle image is a disk whose diameter is determined by the aperture of the lens, the chances of overlapping images are sizable. This leads to ambiguity in the interpretation of the images. However, reducing the height of the particle images by use of masks, leads to loss of intensity, resulting in noisy images. It is our experience that, with the camera used for this study, the cylindrical lens approach to image compression [60] works well in lenses with small focal length, e.g. 55 mm, but as this value increases, a cylindrical lens with an extremely long focal length (>10 m) would be necessary. Instead of a unidirectional compression of the particle images, we will focus on the processing of images with circular spots; the algorithm can be readily adapted to ellipsoidal particle images.

The first task is locating the particle images. We make use of the circumstance that, when droplets are illuminated by a thin light sheet, all particle images have the same diameter d_i, and we convolve the image with a kernel $\kappa(x, y) = 1$ if $x^2 + y^2 < (d_i/2)^2$, and 0 otherwise. Next we seek for the local maxima in the convolved image. A center pixel (x_0, y_0) is a local maximum if its intensity is a factor F larger than all points within the circle $(x - x_0)^2 + (y - y_0)^2 = (d_i/2)^2$. For F we typically took the value $F = 1.1$. This leaves us with many candidate centers for each particle image. These are further pruned by sorting their intensities in decreasing order, picking the first candidate center, and deleting all other candidate centers that fall within the search circle of this particular image, and so on. For isolated particle images, this procedure leaves us with a complete list of images that satisfy the intensity contrast criterion. Exactly the same steps can be used for ellipsoidal particle images with circles replaced by ellipsoids. The key point of this procedure is the *a priori* knowledge of the outline of a particle image.

After finding the particle images, for each of them, the pixel values are summed along the fringe orientation (y-direction), resulting in an intensity distribution $I(x)$ for each of them. The function $I(x)$, $x \in [-d_i/2, d_i/2]$ is

defined at discrete pixel locations x_i; it is differentiated to reduce the pedestal modulation, extended with zeros to the left $x < -d_i/2$, and to the right, $x > d_i/2$, and Fourier transformed. The zero padding provides an interpolation on the spatial frequencies.

From the Fourier transform we determine the spatial wavelength λ_I with the maximum energy, and the corresponding phase ϕ. Due to the optical arrangement in our experiment, and the rather small particle sizes, often no more than a few fringes are observed and further refinement of the found fringe wavelength λ_I is necessary.

To this aim we fit the measured intensity function $I(x)$ to

$$I(x) = a \left[1 - \left(\frac{2x}{d_i} \right)^2 \right]^{1/2} \frac{(1 + c \cos\{2\pi(x/\lambda_I + \phi)\})}{(1 + c)}, \qquad (3.5)$$

where the intensity a, the fringe contrast c, λ_I, and the phase ϕ are determined in a least-squares procedure. The first factor results from the compression of the particle image in the y-direction and the second factor represents the fringes. Since for λ_I and ϕ a good estimate already exists from the Fourier transform, the least squares procedure was restrained. Without the refinement provided by Eq. (3.5), the fringe wavelengths λ_I and measured particle sizes approximately lock to discrete values.

The first question is whether this procedure reproduces the particle size distribution functions $P(d_p)$ in simulated images, and in particular whether the influence of particle overlap is detrimental.

3.1.3 Simulated images

Simulated particle images were made by randomly sprinkling disks with fixed diameter d_i and intensity profile

$$I(x,y) = \left[1 + \cos\left(\frac{2\pi x}{\Delta x} \right) \right] I_p(x - x_0, y - y_0), \qquad (3.6)$$

where $I_p(x,y)$ is I_0 inside the disk $x^2 + y^2 \leq (d_i/2)^2$, and 0 outside, and Δx is inversely proportional to the particle diameter d_p, $\Delta x = \mathrm{F}_p d_i / d_p$, with a proportionality factor F_p, whose value is determined from the experimental parameters θ_r, m, λ, etc. In the experiments the droplets are illuminated using a laser sheet with a Gaussian intensity distribution, accordingly the droplet

intensity was taken proportional to $\exp(-z^2)$, with z sprinkled uniformly on the interval $[-1.5, 1.5]$. Finally a small amount (1.5%) of random noise was added to the simulated images. The particle diameters d_p were picked randomly from a Gaussian distribution,

$$P(d_p) = \frac{1}{d_\sigma \pi^{1/2}} \exp\left[-\frac{(d_p - d_m)^2}{d_\sigma^2}\right], \tag{3.7}$$

with mean d_m and Gaussian width d_σ.

To assess the functionality of the processing algorithm, let us first look at the resulting histograms of the synthetic data. We simulate data over a range of droplet diameters $d_m = 10\ldots30\,\mu$m, in steps of $2.5\,\mu$m and Gaussian width $d_\sigma = 5\,\mu$m. This range was chosen because the smallest droplet diameters come with less than two fringes. Figure 3.2(a,b) show sample images and the resulting distributions produced by the processing algorithm. The resulting distributions are compared with the simulated ones. It can be seen that our procedure correctly reproduces the prescribed $P(d_p)$, but that problems arise at small particle diameters, where a particle image contains a single fringe. As expected, this problem is aggravated when particle images clutter.

In the case of Figure 3.2(a,c), a properly identified disk, overlaps on average with 2.5 disks in a simulated image, which is equivalent to an overlap coefficient of $\gamma_o = 0.24$, and only a fraction (0.36) of the generated droplets is found. For Figure 3.2(b,d), a found disk overlaps overlaps with 1.6 simulated disks ($\gamma_o = 0.36$), and a fraction of 0.55 of the simulated disks is found.

Probability density functions for a distribution of three superimposed Gaussians are shown in Figure 3.2(c,d). The problem with overlaps now is that, in a broad range of sizes, the number of small droplets is underestimated as overlaps introduce extra (but out-of-phase) fringes in a particle disk.

It may seem surprising that images with many overlapping particle disks, such as shown in Figure 3.2 still result in relatively small errors in measured particle size PDFs. We will try to understand this by using the simulated images, in which all droplet intensities and locations are known *a priori*, for further statistical analysis. The problem of overlaps is that found image disks may not correspond to one particular droplet, but may be positioned somewhere in the overlap region and cover several different droplet images. The spatial fringe frequency would, in that case, not correspond to any of the overlapping particle images. The advantage of our disk location method is that it is strongly biased towards a particular particle disk. It does not identify a particle disk through its edges, neither through its intensity maximum, but through
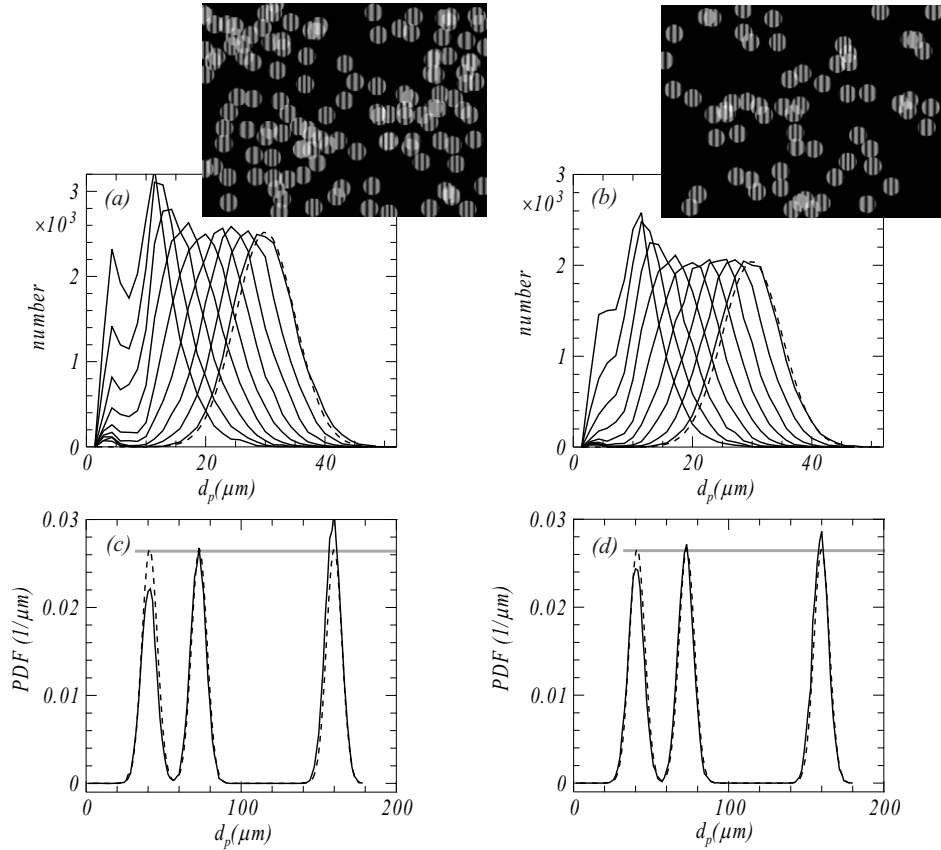
Figure 3.2: *(a) Particle size histogram measured from simulated images, with 128 particle images per frame, and 1024 frames. (b) Same as (a), but 64 particle images per frame. The particles sizes were distributed according to a Gaussian distribution, with mean $d_m = 10 \ldots 30\,\mu m$, in steps of $2.5\,\mu m$ and Gaussian width $d_\sigma = 5\,\mu m$. The dashed distribution represents the input to the synthetic data generation. The images are for the case $d_m = 30\,\mu m$. (c) Particle size distribution function measured from simulated images, with 128 particle images per frame, and 1024 frames. (d) Same as (c), but 64 particle images per frame. The dashed lines indicate the input PDF, the horizontal grey lines illustrate the d_p-independent peak heights of the input particle distribution. The PDFs have been normalized.*

its known shape—a disk, or an ellipse if cylindrical lenses are involved in the imaging.

The first question is if a particle found with our methods actually corresponds to a true particle disk, or falls somewhere in between overlaps. The answer can be found in Figure 3.3(a) where we show the histogram of distances of a found particle disk to the one in the simulated image that is nearest. Clearly, most particle disks are identified correctly, 94% of the found disks fall within $r_i/2$ of a simulated disk for the most dense image (Figure 3.2(a)). If particle disks overlap, the next question is if our method selects the brightest of a group of overlapping particle disks. The answer is in Figure 3.3(b), where we show the histogram of distances of a found particle disk to the original brightest one in an overlapping cluster. In most cases (83%) the brightest of a cluster corresponds to the found particle disk.
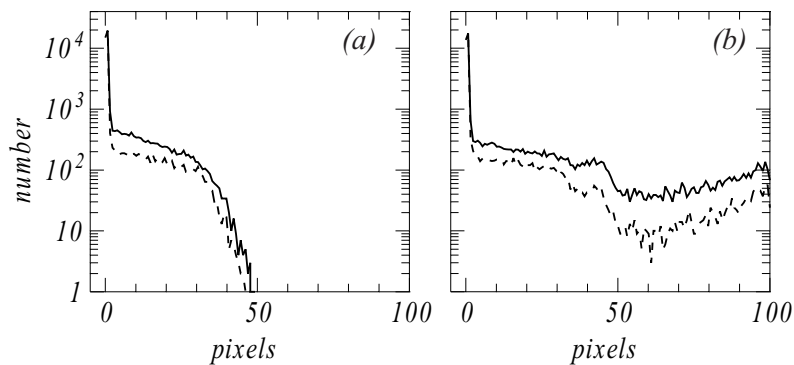

Figure 3.3: *(a) Histogram of distances of a found particle disk to the one in the simulated image that is nearest. The conditions are those from Figure 3.2. The full line corresponds to 128 particle disks per image, the dashed line to 64 particle images. The disk radius r_i is 50 pixels. For 128 (64) particle disks per image, each found particle disk overlaps on average with 2.5 (1.6) disks in a simulated image. (b) Same as (a), but now the distance is to the brightest simulated particle disk in an overlapping cluster.*

From these simulations we conclude that our methods find the correct PDF of particle sizes, as long as particles are not so small that their images contain less than two fringes. Finding the correct PDF of small particles ($d_p \lesssim 15$ μm) becomes more difficult when the particle density increases and particle images severely overlap. In the case of Figure 3.2(b), a fraction of 36% of the simulated droplet images is actually found because many images overlap, nevertheless, the resulting PDF of particle sizes appears to be correct.

Let us again emphasize that our approach differs from earlier work, where the main concern was the correct identification of droplets, their location and their velocity, in addition to their size. In this context, overlapping droplet images are indeed detrimental, as it leads to ambiguity about location and size.

3.1.4   Experimental validation

After establishing the functionality of our algorithm with synthetic data, we test it once again by imaging interference patterns of glass microspheres whose diameters have been measured using a microscope. The imaging setup for measurements of both glass spheres and droplets consists of an Nd:YAG laser (CFR 150, Quantel) with wavelength $\lambda = 532$ nm as a light source, and a 1200×1600 pixel CCD camera (ES 2020, Redlake). We create a light sheet by using a cylindrical lens.

Figure 3.4 compares the microsphere diameter histograms obtained through IPI and microscopy, which are in good agreement. Even though the glass spheres are spherical and smooth, inhomogeneities in their refractive index (possibly due to porosity) produce wavy fringe patterns when imaged with the IPI setup. Nevertheless, the IPI algorithm is robust enough to interpret the wavy fringes and reproduce the histogram of particle distributions reasonably well.
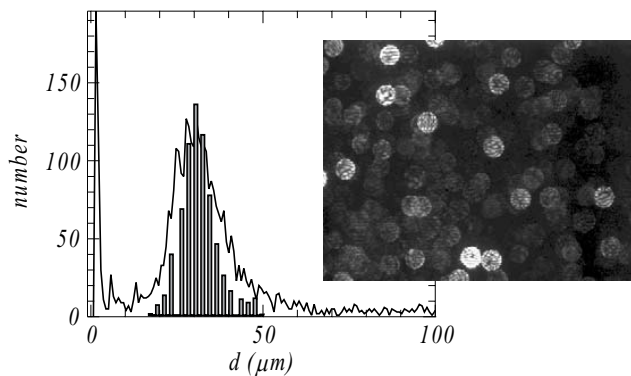

Figure 3.4: *Comparison of particle size distribution function measured from calibrated glass spheres by IPI and microscopy (in grey). Inhomogeneities in the refractive index of the glass microspheres result in wavy interference patterns. In this arrangement, the fringes run horizontally.*

3.2   Droplet generation

As previously mentioned, several monodisperse droplet generation methods are available. Vibrating orifice and flow focussing generators exploit the Rayleigh–Plateau instability. The former method, first proposed by Berglund & Liu [64], uses a piezo-electric crystal, or some other controllable vibrating mechanism, in order to induce perturbations on a liquid jet. These perturbations grow and result in the controlled pinch-off of identical droplets. The latter method focusses a liquid meniscus into a thin liquid thread by means of a concentric (gas or liquid) jet [65]. The interaction between the outer and inner fluids produces a Kelvin–Helmholtz instability at the interface which translates into a Rayleigh–Plateau instability, resulting in a controlled droplet pinch-off. The main drawback of these two methods is the inability of producing many simultaneous droplets, which is necessary in our flow tagging experiments given many droplets are lost in collisions against the wall.

Spinning disks and tops offer a considerably higher droplet production rate, at the cost of reduced monodispersity. We opt for the spinning disk generation due to cost, ease of fabrication and robustness. Let us now explore the working principle of this type of generators.

3.2.1   Spinning disk aerosol generation

Spinning disk aerosol generators were first proposed by May [54] and Walton & Prewett [55] over sixty years ago. An extensive review can be found in Davies & Cheah [56]. The working principle of spinning disk aerosol generators is the breakup of a liquid film at the edge of the disk due to centrifugal forces. Depending on the flow rate of the fluid supplied to the disk surface, droplets are ejected directly, or ligaments first form which break up into droplets. In the first mode of operation, nearly monodisperse droplets are created, trailed by much smaller droplets that result from the trailing ligament breakup. Balancing inertial and surface tension forces provides the droplet primary diameter d_p as a function of the disk radius R, its angular velocity ω, the fluid density ρ and the surface tension γ, $d_p/R = \mathrm{We}^{-1/2}\mathrm{Qu}$, in terms of the Weber number We, or

$$d_p = \frac{\mathrm{Qu}}{\left(R\rho/\gamma\right)^{1/2}\omega}.\tag{3.8}$$

The Quincke number Qu depends weakly on the supply rate of the fluid Q. The analysis of a collection of experiments lead Davies & Cheah [56] to the following empirical relation

$$\text{Qu} = \frac{1}{8}(\log \text{Qe} + 2.85)^2 + 2.15. \tag{3.9}$$

The dimensionless flow rate $\text{Qe} = Q/(2\pi R^2 (\nu\omega)^{1/2})$, is formed from Q and a reference value for a thin film driven by a centrifugal force, with ν the kinematic viscosity. Experiments show that the transition from direct droplet ejection to ligament formation occurs at Li $\simeq 0.08$, with the ligament number Li $= \text{QeWe}^{1.15}\text{Re}^{-0.95}$, which compares the length of the attached ligaments to their mutual distance [56].
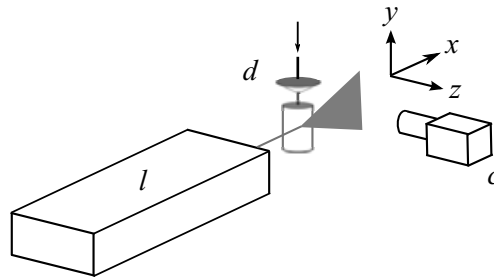

Figure 3.5: *Experimental setup for SDAG droplet measurement. A laser l illuminates the droplets being generated by the spinning disk d. The optical axis of the camera c is perpendicular to the laser sheet, i.e. $\theta_r = 90°$. The intensities of the reflection and first order refraction are comparable at this angle for the expected primary droplet sizes. The arrow points to the needle which feeds liquid onto the disk.*

For this study we use an air-driven spindle (EST 1000K, Mannesmann-Demag, Stuttgart, Germany) and two disks: radii 1 and 4 cm. Both disks are manufactured in-house out of stainless steel. The maximum angular velocity reached by the spindle is approximately $3600\,\text{s}^{-1}$ for the large disk and $7500\,\text{s}^{-1}$ for the small one. Even wetting is crucial to create a uniform film. We are interested in droplet sizes between $10\,\mu\text{m}$ and $60\,\mu\text{m}$. Given our maximum angular velocities, we must reduce the surface tension by means of surfactant addition in order to achieve such diameters. This also ensures proper wetting. We used demineralized water with Triton-X100 at 1% by vol-

ume to achieve a surface tension of $\gamma = 3.0 \times 10^{-2}$ N/m. The imaging setup is described in Section 3.1.4.

The purpose of the experiments was to measure the size distribution of droplets created by the spinning disk. Their mean size will be compared to the predictions by [56]. However, information about the size distribution appears to be scarce in the literature. Each data set contained 1000 frames taken at a sampling rate of 15 Hz. The number of valid droplets imaged in each frame depended on the particular optical setup of each case, i.e. the values of v, f and d_a.

Measurement of droplets with diameters in the vicinity of 30 μm presents a few practical issues. As apparent from Figure 3.1, a shorter distance v is desirable to increase the fringe frequency. Similarly, a larger aperture diameter will result in more inlying fringes. Unfortunately, these two approaches for decreasing the fringe spacing may have a negative impact on the data. To locate the particle images, our algorithm relies on the uniform diameter of the interference spots, which can only be achieved if the object distance v is equal for all droplets, that is, all imaged droplets lie within a thin volume parallel to the image plane. Lenses with large focal length were more susceptible to variations in spot size since a small change in the object distance v had considerable impact on the image distance b. This was particularly problematic when big droplets were imaged, since they can scatter sufficient light to be detected even when outside the laser sheet. To ensure the spot diameter remains constant a compromise between the focal length and the aperture diameter of the objective must be sought, depending on the droplet size.

3.2.2   Principal planes

All the above calculations assume a thin lens approximation, which does not apply to compound camera lenses. The accuracy in the measurement of the object distance v has a direct impact on the accuracy of measurement of droplet diameters. To determine the value of v, we do the following: take v' as the distance from the object to some reference plane P_{ref} on the objective, and δ as the distance from P_{ref} to the principal plane of the compound lens. We then have

$$\frac{1}{v' + \delta} + \frac{1}{b} = \frac{1}{f}$$

where b represents the distance from the image plane to the principal plane and f is the focal length. Then the magnification becomes

$$M = \frac{b}{v' + \delta}.$$

We combine the above equations to obtain

$$v' + \delta = f\left(\frac{M+1}{M}\right). \tag{3.10}$$

Using a calibration target we monitor the magnification as we change the distance between the object and the reference plane. From the values of v' and M we find a linear relation, the slope of which is determined by the focal length of the lens, and the y-intercept represents the value of δ (see Figure 3.6). To validate this result we compare the slope of the line to the lens focal length f and get a match to within 3%.
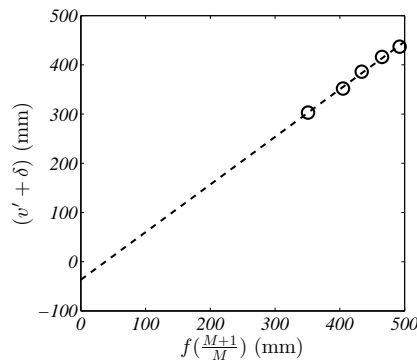

Figure 3.6: *Distance between reference plane and object plane as a function of the magnification for the $55\,mm$ focal length lens. The y-intercept represents the distance δ between the principal plane and the reference plane P_{ref}. A similar result, to within 0.5%, was obtained for the 105 mm lens.*

3.2.3   Disk size and Kármán flow

Rotating objects can act as pumps by inducing flow normal to the axis of rotation, which in turn creates an axial flow in order to replace the fluid transported outwardly. These flows were first studied by von Kármán, who

through a series of transformations described the flow created by an infinite disk. Cochran [66] followed von Kármán's analysis and found a numerical solution for the transformed variables. From Cochran's solution we know the induced flow velocity $u \propto R\omega$.

In our flow tagging experiments and PIV measurements, this parasitic flow disturbed the flow within the chamber, which, as seen in Chapter 2, must be homogeneous, isotropic and have a negligible mean velocity.

For a given droplet size d_p, a disk with large radius rotates more slowly, but the secondary flow is larger. From Eq. (3.8) we see that $u \propto R^{1/2}d_p^{-1}$. Additionally, the viscous drag on the disk is proportional to R^4, which results in a need for higher air pressures for larger disks. If the air pressure is limited, as in our case, the use of a small disk is preferred.

3.2.4 Droplet ejection distance

As the droplets rupture from their ligaments, they are ejected with the tangential velocity of the disk, which in some cases exceeds 100 m/s. The difference in diameter between the primary and satellite droplets results in a different deceleration magnitude, creating a spatial segregation. We can take advantage of this fact to separate droplets depending on the spatial position they reach after being flung away from the disk. To accomplish this, we must calculate at what point in space will the droplets stop when ejected into still air. The prediction of the velocity and position of a droplet will allow for the separation between bigger primary droplets and smaller satellite droplets. From Newton's second law we have

$$m\frac{\mathrm{d}^2x}{\mathrm{d}t^2} = -C_D\frac{\pi\rho_a r_p^2 V_d^2}{2} \tag{3.11}$$

where m is the mass of the droplet, C_D is the coefficient of drag, ρ_a is the density of the air, $r_p(= d_p/2)$ is the droplet radius and $V_d = \mathrm{d}x/\mathrm{d}t$ is the velocity of the droplet. The mass of the droplet is related to its diameter and density. Since the density ratio of the carrier fluid to the particle plays an important role, we wish to state this explicitly,

$$\frac{4}{3}\pi r_p^3\rho_p\frac{\mathrm{d}^2x}{\mathrm{d}t^2} = \frac{1}{2}\rho_a\pi V_d^2 r_p^2 C_D. \tag{3.12}$$

The initial droplet velocity is given by the diameter of the spinning disk D and its angular velocity ω. For small droplets ($r_p \sim 10\ \mu$m), the particle

Reynolds number can reach magnitudes on the order of 10^2, where Stokes flow is inapplicable. We use the definition given by [67],

$$C_D = \frac{24}{\mathrm{Re}}\left[1 + \frac{1}{6}\mathrm{Re}^{2/3}\right],$$

(we know $\mathrm{Re} = 2V_d r_p/\nu_a$) and Eq. (3.12) becomes

$$\frac{\mathrm{d}^2 x}{\mathrm{d}t^2} = \frac{9}{2}\frac{\rho_a \nu_a}{\rho_p}\frac{1}{r_p^2}V_d\left[1 + \frac{1}{6}\left(\frac{2V_d r_p}{\nu_a}\right)^{2/3}\right]. \tag{3.13}$$

Integrating Eq. (3.13) once and twice for velocity and position, respectively, and applying the initial conditions $V(0) = V_0$ and $x(0) = D/2$, we arrive at (see Appendix A.2 for full derivation)

$$V_d(t) = \frac{e^{-\alpha t}}{\left(-\beta e^{-\frac{2}{3}\alpha t} + \left(\frac{D}{2}\omega\right)^{-2/3} + \beta\right)^{3/2}} \tag{3.14}$$

and

$$x(t) = -\frac{3}{\alpha}\left[\frac{e^{-\frac{1}{3}\alpha t}}{\beta(V_0^{-2/3} + \beta - \beta e^{-\frac{2}{3}\alpha t})^{1/2}}\right.$$
$$-\frac{1}{\beta^{3/2}}\tan^{-1}\left(\frac{\beta^{1/2}e^{-\frac{1}{3}\alpha t}}{(V_0^{-2/3} + \beta - \beta e^{-\frac{2}{3}\alpha t})^{1/2}}\right)$$
$$\left.+\frac{1}{\beta^{3/2}}\tan^{-1}\left(\frac{\beta^{1/2}}{V_0^{-1/3}}\right) - \frac{1}{\beta V_0^{-1/3}}\right] \tag{3.15}$$

where

$$\alpha = \frac{9}{2}\frac{\rho_a \nu_a}{\rho_p r_p^2} \qquad \text{and} \qquad \beta = \frac{1}{6}\left(\frac{2r_p}{\nu_a}\right)^{2/3}.$$

Unfortunately, this equation fails to describe the velocity and position of a droplet that is ejected into a turbulent fluid, which is the case for most instances analyzed in this study. However it can be useful if the spinning disk is small enough that the Kármán flow is negligible.

3.3   Results and discussion

3.3.1   Droplet size distribution

From the experimental data we are able to retrieve the histograms of the droplets produced using spinning disks. Figure 3.7 shows droplet diameter PDFs for two disk radii, $R = 1\,\text{cm}$, and $R = 4\,\text{cm}$, and a range of rotation speeds. The particle size distribution functions show a large peak at $d_p \approx 1.5\,\mu\text{m}$, which corresponds to particle disks without interference fringes. These blank disks are produced by very small droplets, such images contain too little information, and our algorithm decides on a fringe spacing which equals half the droplet disk diameter. It must be noted that this peak, while present in the histogram of the glass microspheres, is much higher in the case of droplets produced by the SDAG. We believe this difference stems from the presence of tiny droplets created during ligament breakup.

Particle disks with a single intensity minimum give rise to another parasitic peak at $d_p \approx 5\,\mu\text{m}$ and $d_p \approx 9\,\mu\text{m}$, depending on the optical arrangement used. Such images /are often the result of overlaps. For large enough mean droplet diameters, the contribution of the satellite droplets can be observed as a broad distribution centered at $\approx d_p/3$ for the $R = 4\,\text{cm}$ disk. This distribution is much broader in case of the $R = 1\,\text{cm}$ disk.

Our image analysis algorithm finds a broad range of droplet sizes, apart from a well-defined contribution of the main droplets. The corresponding peak in the PDF has a significant width, with both peak position and width quantified using a Gaussian fit. The results for the two disk diameters are shown in Figure 3.8. The agreement with the predicted size is fair. Although the cause of the discrepancy is not entirely clear, we believe evaporation might explain the disparity.

The main droplets are fairly monodisperse; the width of the primary peak in the PDF is about $7\,\mu\text{m}$ for the smallest droplet size, and increases to $\approx 10\,\mu\text{m}$ for the largest ones. The peak positions and widths were quantified using a Gaussian fit. The results for the two disk diameters are shown in Figure 3.8, with the error bar indicating the full width half maximum of the peak. The agreement with the predicted size is fair. Although the cause of the discrepancy is not entirely clear, we believe evaporation might explain the disparity.
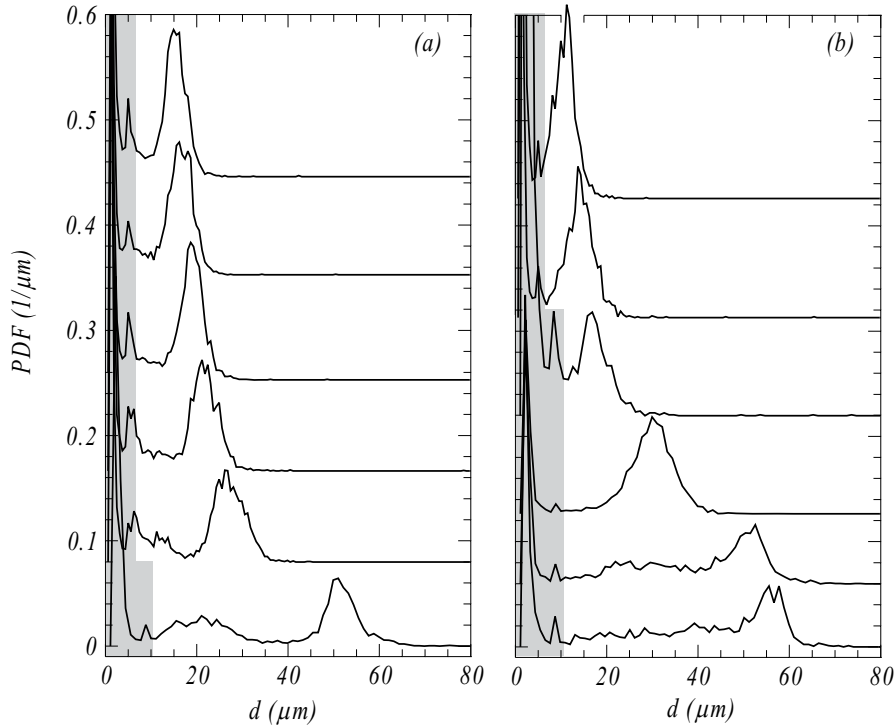
Figure 3.7: *Particle diameter PDFs of droplets generated by spinning disks with radius $R = 4$ and $1\,cm$ for case (a) and (b), respectively. The angular velocity of the disk decreases from top to bottom. For frame (a), the values are $\omega = 3.7, 3.6, 3.1, 2.8, 2.2$, and $1.2 \times 10^3\,s^{-1}$. At $\omega = 1.2 \times 10^3\,s^{-1}$, the ligament number is $Li = 3.5 \times 10^{-5}$. In the case of frame (b) the rotation speeds are $\omega = 7.6, 5.8, 5.1, 3.5, 2.2$, and $2.1 \times 10^3\,s^{-1}$. At $\omega = 7.6 \times 10^3\,s^{-1}$, the ligament number is $Li = 3 \times 10^{-3}$. For large enough mean droplet diameters, the contribution of the satellite droplets can be observed as a broad distribution centered at $\approx d_p/3$ for the $R = 4\,cm$ disk. This distribution is much broader in case of the $R = 1\,cm$ disk. The greyed regions denote the droplet diameters that are too small to be estimated correctly because particle disks contain less than approximately one intensity minimum. The size of this region depends on the optical arrangement used, for the region reaching to $10\,\mu m$, a lens with $55\,mm$ focal length was used, while a $105\,mm$ lens was used in the region reaching to $7\,\mu m$.*
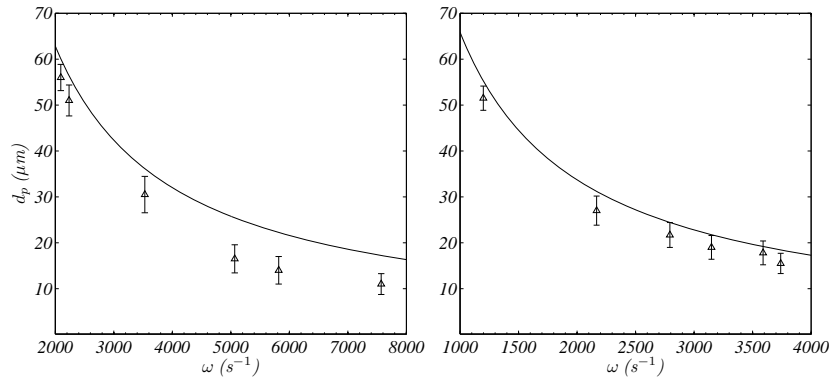
Figure 3.8: *Symbols: Mean diameter of primary droplets as a function of angular velocity for (a) $R = 1\,cm$ and (b) $R = 4\,cm$. The error bars indicate the standard deviation of the droplet diameters, which was obtained from a Gaussian fit to the measured PDFs. Solid lines are the predicted diameters from Davies & Cheah [56]. The measured droplets are consistently smaller than the prediction, which could, partially, be explained by evaporation.*

3.3.2   Satellite droplets

Satellite droplets are a result of ligament breakup. As a drop detaches from its ligament, considerably smaller droplets emerge. Their size and quantity varies depending on the liquid feed rate, normally falling between $d_p/2$ and $d_p/4$ [54]. In each experiment we find a large amount of droplets which are so small that their size could not be determined, i.e. their images are uniform, without a trace of an interference pattern. At low angular velocities, satellite droplets should be big enough to be resolved in our optical setup, but the presence of many blank droplet images suggests otherwise. These tiny droplets imply the ligament breakup process is not a clean one, that is, more than one size of satellite droplets exists, some being much smaller than the others. This is illustrated in Figure 2 of Davies & Cheah [56], which shows a primary droplet followed by several satellite droplets of different sizes as they detach from a ligament.

Even though we have a low Ligament number, it appears that a large amount of detected droplets are extremely small. According to Davies & Cheah [56], if Li $\leq 3 \times 10^{-3}$, only one or two satellites are expected per primary droplet. We see that satellites of about a half to a quarter of the primary droplet diameter do appear in approximately the same quantity as the main

droplets, but the smallest satellite droplets (blank disks) appear in considerably larger amounts.

3.4 Conclusion

We presented an algorithm capable of automatically processing interferometric particle imaging data and test its functionality through simulated data as well as calibrated glass spheres. The processing algorithm is capable of almost exactly reproducing the droplet distribution of the synthetic data for interference patterns with two or more fringes, despite a high number of overlaps. Overlapping particle images negatively impact the ability to reproduce the particle distributions for small droplets, but this effect is small for large droplets. The issue of overlap is circumvented in the processing algorithm by 'locking' to one of the overlapping images, allowing for the correct identification of at least one droplet in the overlapping group. Using this algorithm we analyze the droplet distributions produced by a spinning disk aerosol generator. The measured mean droplet diameter compares well with the predictions of literature [56]. The width of the size distribution of the primary droplets is approximately $3\,\mu$m. We find a large number of satellite droplets with diameters $d_{sat} \lesssim 5\,\mu$m, whose size could not be measured and are considerably smaller than the expected satellite droplet diameter of $d_p/4 < d_{sat} < d_p/2$.

CHAPTER 4

PHOSPHORESCENT FLOW TAGGING [†]

In the previous chapter we have illustrated the experimental methods necessary to establish the proper flow conditions that will allow us to test our proposed phosphorescent tagging technique. The foreseeable applications for this technique are varied: one can observe the dispersion of a cloud of particles, analyze the deformation of material lines of the dispersed phase, or follow a specific set of droplets using particle tracking techniques, among others. In the present chapter we focus on the workings of the tagging mechanism itself, as well as practical details about the phosphorescent solution, leaving its application for later chapters. In Section 4.1 the photophysics involved in the tagging process are briefly explored, and the distinction between fluorescence and phosphorescence is clarified. In Section 4.2 we give an overview of Molecular Tagging Velocimetry; Section 4.3 addresses the characteristics of lanthanide chelates and explains the optimization of the phosphorescent solution. We close the chapter with conclusions in Section 4.4.

[†] This chapter done in collaboration with Thanja Lamberts.

4.1   Photophysics

Photophysics describes the interaction between light (photons) and matter (atoms or molecules). The photophysical properties of each molecule determine the wavelength and number of photons required to take it into a particular excited state. Quantum mechanics dictates there are a number of discrete electronic states in which an atom or molecule can reside, with the ground state, under normal circumstances, being the most probable.

Typically, atomic or molecular energy levels are illustrated schematically using Jablonski diagrams like the one in Figure 4.1. Three distinct groups of lines are shown, each representing (in this illustrative case) a particular spin state, S_0 being the singlet ground state, and the vertically ascending groups symbolizing excited singlet (S) or triplet (T) states of increasing energy. The lines within these groups correspond to different vibrational states. Each vibrational state has fine structure due to rotation, but this is omitted here. Molecules in any state may transition to another state through interactions with their environment. Not all transitions can take place, or are 'allowed', as a result of symmetry constraints and selection rules that follow from theory.
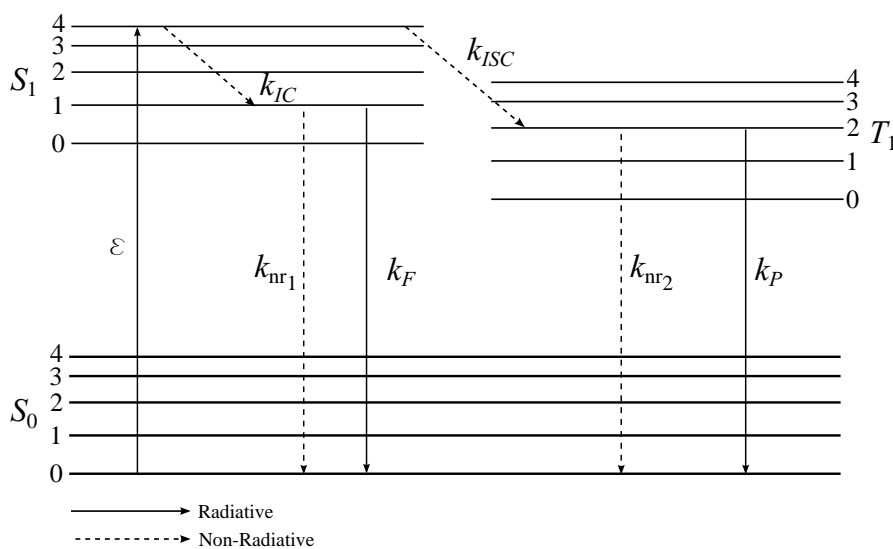

Figure 4.1: *A Jablonski diagram illustrates the different molecular states. The labels, S and T stand for singlet and triplet, and denote the total electron spin state of a system. The numbers alongside each group of lines are the vibrational quantum numbers.*

Symmetry restrictions for larger molecules can usually be neglected as these molecules themselves are often no longer symmetric. One selection rule that applies to every system is the selection rule for the net electron spin, which states that electric-dipole-induced transitions cannot take place between energy levels of different spin state. This concerns, in first order, all radiative transitions. In general, a real (and often unknown) energy level in a molecule can be thought of as a combination of known theoretical energy levels with various spins. This leads to forbidden transitions to be in fact observable, although typically with low efficiency.

Phosphorescence typically arises from forbidden transitions. The low efficiency of these transitions has a negative effect on the excitation process $S_0 \rightarrow T_1$. Nevertheless, in our application, low efficiency can be beneficial in the relaxation process, i.e. $T_1 \rightarrow S_0$, since molecules will only slowly emit photons as they relax. In molecules in which the excited singlet ($S_{1,2,...}$) and triplet states are strongly coupled, one can use the alternative route of Figure 4.1 to avoid the direct excitation process and indirectly create a pool of highly excited (metastable) molecules. This is achieved by exciting S_1, which is quickly transferred to T_1, where thermalization occurs so that the entire population reaches $T_1(\nu=0)$. This, too, is important since $T_1(\nu=0)$ is lower in energy than S_1, therefore, with no energy-conserving way back to S_1, the excited pool is trapped in T_1.

In what follows, a brief description of the main processes is given. For an in-depth review of photophysics we refer the reader to [68, 69].
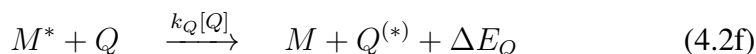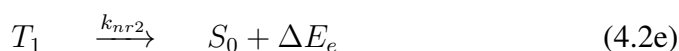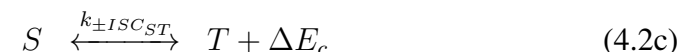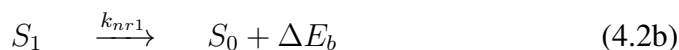
4.1.1 Photophysical processes

We consider three radiative processes: absorption, fluorescence and phosphorescence. Absorption is the process in which a molecule takes a photon and reaches an excited state,

$$S_0 + h\nu \xrightarrow{\epsilon} S_1. \tag{4.1}$$

The efficiency of the absorption process in Eq. (4.1) is measured by the extinction coefficient ϵ. Once a molecule is taken to an excited state, it can return to its ground state through both radiative or non-radiative decay, that is, through the release of energy in the form of a photon or as heat. In general, this so-called relaxation can proceed via various pathways, as indicated

in Figure 4.1.

$$S_1 \quad \xrightarrow{k_F} \quad S_0 + h\nu \tag{4.2a}$$

$$S_1 \quad \xrightarrow{k_{nr1}} \quad S_0 + \Delta E_b \tag{4.2b}$$

$$S \quad \xleftrightarrow{k_{\pm ISC_{ST}}} \quad T + \Delta E_c \tag{4.2c}$$

$$T_1 \quad \xrightarrow{k_P} \quad S_0 + h\nu \tag{4.2d}$$

$$T_1 \quad \xrightarrow{k_{nr2}} \quad S_0 + \Delta E_e \tag{4.2e}$$

$$M^* + Q \quad \xrightarrow{k_Q[Q]} \quad M + Q^{(*)} + \Delta E_Q \tag{4.2f}$$

Each decay process has a certain probability of occurrence, which is represented by a rate constant k. In an ensemble (population of molecules), all the processes described by Eqs. (4.2) happen simultaneously at different rates. Depending on the process being allowed or forbidden, the rate coefficient k is large or small, respectively.

After absorption, the energy in the excited state can decay back to the ground state through phosphorescence (Eq. (4.2d)), or fluorescence (Eq. (4.2a)), or an inter-system crossing (ISC, Eq. (4.2c)) may occur. Note that phosphorescence is usually preceded by inter-system crossing. Non-radiative transfer of energy (Eqs. (4.2b) and (4.2e)) or energy flow through highly energetic vibrations, can also lead to a decay from the excited state to the ground state, which is accompanied by a release of surplus energy as heat.

4.1.2   Rates of decay

Fluorescence and phosphorescence are collectively known as luminescence, and both are radiative decay processes. Atoms and molecules, depending on their particular structure, can often be modeled as two- or three-level systems, as shown in Figure 4.2 below.

The natural time evolution of the population of excited molecules or atoms in a two-level system can be represented mathematically as

$$\frac{\partial N_2(t)}{\partial t} = -k_{21} N_2(t), \tag{4.3}$$

resulting in an exponential decay: $N_2(t) \propto e^{-k_{21}t}$. The addition of a third level adds substantial complexity to the system, since two simultaneous processes
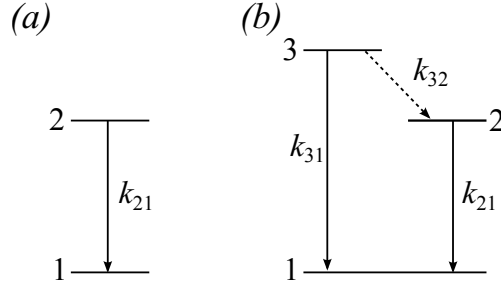
Figure 4.2: *Schematic representation of (a) two- and (b) three- level systems. In our experiment we excite in 1→3 and observe in 2→1. 3→2 represents inter-system crossing.*

affect the decay of the excited population:

$$\frac{\partial N_2(t)}{\partial t} = -k_{21} N_2(t) + k_{32} N_3(t) \tag{4.4a}$$

$$\frac{\partial N_3(t)}{\partial t} = -(k_{31} + k_{32}) N_3(t) \tag{4.4b}$$

Integrating the above equations yields

$$N_2(t) \propto \frac{k_{32}}{k_{31} + k_{32} - k_{21}} e^{-k_{21}t} \left(1 - e^{(k_{21}-k_{31}-k_{32})t}\right) \tag{4.5a}$$

$$N_3(t) \propto e^{-(k_{31}+k_{32})t}. \tag{4.5b}$$

Eqs. (4.5) show us a clear distinction between the decay rates of these two different processes. The time constants for fluorescence and phosphorescence are $\tau_f = 1/(k_{31} + k_{32})$ and $\tau_{ph} = 1/k_{21}$, respectively, which helps explain the difference in the lifetimes between the two mechanisms; in general, $\tau_f \ll \tau_{ph}$.

Both of these decay mechanisms can be used for fluid flow diagnostics, each having advantages and disadvantages. Fluorescence typically has a stronger signal intensity since all photons are emitted quasi-instantaneously, while in phosphorescence a slower emission of photons translates into a longer lasting signal with a significantly lower intensity.

4.2 Molecular tagging velocimetry

Now that we have a better, albeit limited, understanding of photophysical processes, it is time to apply this knowledge to a flow diagnostic tool. Molecular

tagging velocimetry (MTV) encompasses minimally or non-intrusive proce-
dures in which the photochemical characteristics of specific molecules, ei-
ther naturally occurring or added to the fluid, are exploited to get information
about the flow characteristics. The main advantage of this class of techniques
is the use of the fluid itself as a flow tracer; however, certain issues may arise
due to the excitation process. A brief explanation of the different MTV meth-
ods will be given below. For an in-depth analysis, we refer the reader to [70]
and references therein.

In a nutshell, the extraction of information consists of tagging a well de-
fined region of the flow and visualizing the tracers after a determined period
of time (Figure 4.3). Naturally, the experimental aspects will impact the mea-
surements, i.e. which components of the velocity can be extracted, the maxi-
mum tracking period, *et cetera*. Typically, the tagging step is achieved using
a focused pulsed laser, which allows for a well-defined region to be tagged
in a well-defined moment in time. The visualization or reading step can be
performed one or more times, depending on the lifetime of the tracer. With
this data, a Lagrangian displacement vector can be calculated, from which an
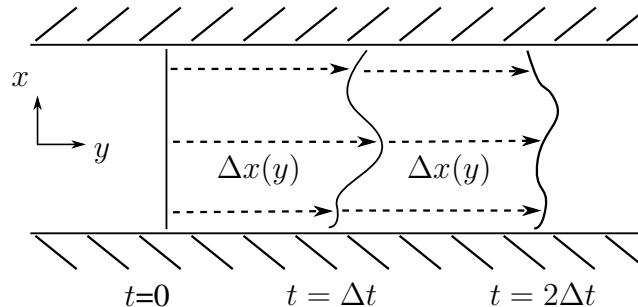estimate of the velocity vector can be obtained.

Figure 4.3: *Schematic representation of molecular tagging velocimetry as a flow
diagnostic in channel flow. At $t = 0$ a straight line is tagged, after a short period
of time Δt, the interrogation or reading step is performed. The displacement
vector Δx can be used to determine the average velocity of the flow between the
writing and reading steps.*

An important consideration is the pattern chosen for tagging, e.g. line,
cross, grid, etc., which will be used to determine certain properties of the flow,
and will limit access to some information. For example, in some instances, if
we choose to tag a line, information about the flow parallel to the line will not
be available.

4.2.1   Tagging mechanisms

There are two main tagging mechanisms in molecular tagging velocimetry, both of which start with one or several precursors. These are photochemically manipulated by one of two options: 1) direct excitation of a precursor to create a metastable state or 2) creation of a different chemical species through photochemistry. Techniques such as RELIEF, LIPA and phosphorescence fall into the first category. The second class includes PHANTOMM, APART, and several other nitric oxide (NO) production techniques. Let us briefly look at a some of these techniques.

LIPA (Laser-induced photochemical anemometery, Figure 4.4(a)) is based on the detection of absorbance by using a tautomer—a structural isomer that can rapidly interconvert due to proton transfer—as a tracer. The tracer M is excited radiatively with photons of energy $h\nu$ producing an excited molecule M^*. This excited molecule then relaxes via non-radiative decay creating a high-energy tautomer (the molecule consists of the same atoms connected through different bonds). The absorption spectra of M and P_{taut} are different, allowing the use of white light to detect the excited tracer. The advantage of this method is the long lifetime of P_{taut}, which can reach several seconds before thermally converting back to M, while the drawbacks include the need for two light sources, the poor solubility of known photochromic dyes in water, and the low signal-to-noise ratio caused by the measurement of the difference between the incident and the transmitted light instead of measuring an emitted signal against a black background.

On the other hand, in RELIEF (Raman excitation plus laser-induced electronic fluorescence, Figure 4.4(b)) the precursor M is irradiated with radiation of frequency ν_0. Through Raman scattering, a vibrationally excited state M' is created at a level $\nu_0 - \nu$, which is a long-lived tracer that can be interrogated using a second light source producing $h\nu'$. M^* decays back to M via fluorescence, making it possible to detect the displacement of the fluid. The first step of this mechanism ($h\nu_{ex}$) requires a high power laser or a stimulated Raman scattering setup to produce enough M'.

PHANTOMM—photo-activated non-intrusive tracking of molecular motion—is schematically portrayed in Figure 4.4(a). This technique uses 'caged' fluorescent tracers to visualize the flow, falling into the second tagging mechanism. The caging consists of attaching a deactivating group to the tracer molecule, and removing this group photochemically. The removal is irreversible, meaning that the fluid containing uncaged tracers can be tracked
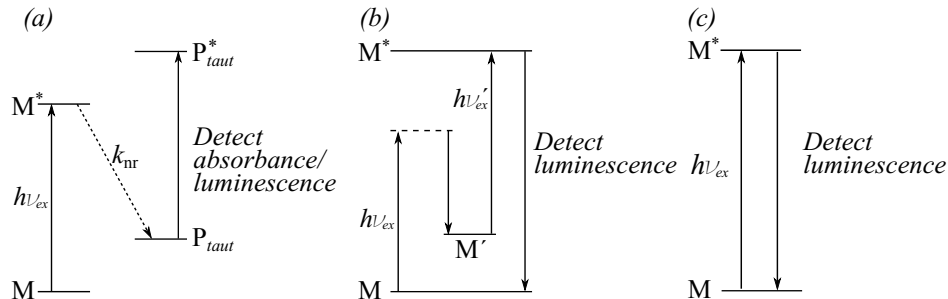
Figure 4.4: *Schematic diagrams of the four general mechanisms used in MTV. (a) LIPA and PHANTOMM, (b) RELIEF, and (c) direct phosphorescence.*

indefinitely as long as the reading step is repeated. This can be advantageous in instances such as channel flow, since it allows to observe the tagged fluid for long periods of time, but requires replacement once a considerable amount of tracer has been uncaged.

Direct phosphorescence, as illustrated in Figure 4.4(c), works by exciting a molecule with photons of a specific energy, after which the tracer relaxes by emitting photons of a different wavelength. As we have mentioned before, due to the forbidden nature of most triplet transitions, direct phosphorescence has a low efficiency. A more common approach involves a three-level system as depicted in Figures 4.1 and 4.2(b), where the excited molecule usually undergoes inter-system crossing and decays to the original state by emitting photons of a different wavelength. From the different processes that have been probed, this is the most accessible, requiring only one light source and being directly detectable. As mentioned earlier, it has a relatively long lifetime. Also, the tracer returns to the ground state, meaning it can be reused. The increase in lifetime comes at the price of lower efficiency in the form of quenching and competing energy channels.

4.2.2   MTV applications

Many variations on the mechanisms presented above have been successfully attempted. Different fluorescent or phosphorescent molecules are employed to suit the particular needs of the flow in question as well as the properties of the fluid itself. For an in-depth review, the reader is referred to [70]. Let us revisit a few of these variations for illustration purposes.

The development of the PHANTOMM technique by Lempert et al. [71] was used to visualize tip vortices created by a wing in channel flow with two different tagging agents: dextran carboxy fluorescein and 8-hydroxypyrene-1,3,6-trisulfonic acid. The experiment consisted of tagging a thin line adjacent to the wing and perpendicular to the mean flow with a Nd:YAG laser at 355 nm, and using a dye laser to interrogate the flow at a later time. The technique was tested by measuring a well known velocity profile in Poiseuille flow, agreeing well with theoretical predictions.

Other variations use naturally present compounds to obtain information about the flow, e.g. creating nitric oxide (NO), which can easily be visualized by laser-induced fluorescence, from N_2 and O_2 in air using an ArF excimer laser and a dye laser for interrogation [72]. The technique was applied to a laminar flow and a pulsed jet. This technique had the obvious advantage of avoiding the addition of any seeding, since gases present in the flow are used to determine characteristics of the flow. The problem with tagged molecules in a gas is that written patterns blur because of diffusion. Since the ratio of the diffusion rate of momentum (the kinematic viscosity) to the molecular diffusion is approximately 1, this poses a fundamental limit on the visualization of the smallest vortices of turbulence.

One more example of flow tagging, this time in a dispersed phase, comes from a study performed by Krüger and Grünefeld [45], who used a Terbium-based phosphorescent solution to estimate the velocity of droplets produced by a fuel injector. The droplets were tagged by a laser grid and interrogated twice after a single tagging event. Subsequent images were correlated in a similar fashion as PIV, and the velocity field of the dispersed phase was obtained. In this study, the authors stress the capabilities of flow tagging in dense clouds. The volume tagged was in the central part of the cone produced by the injector, however, the tagged lines were clearly visible and distinguishable from one another even though the space between them was only a few millimeters.

4.3 Phosphorescent solution

As with any experiment, the (time and length) scales of the phenomenon of interest set many of the study parameters. Our case is no different and, as mentioned before, the Kolmogorov scales will define the resolution needed to observe the droplet dynamics. In this regard, the phosphorescent solution

from which the droplets will be produced plays a crucial role in the proposed diagnostic technique. It is its phosphorescence lifetime that will constrain many of the parameters of the flow, and its intensity will affect the imaging setup, more specifically, the gate time of the camera. Given the importance of this component of the technique, it is critical to have a thorough characterization of it, and optimize it to our particular application.

There are several lanthanide elements which have phosphorescent capabilities. One of them must be chosen depending on several factors, e.g. toxicity, ease of synthesis, lifetime, excitation and emission wavelengths.

4.3.1 Tracer characterization and optimization

The first and foremost characteristic we look for in a luminescent tracer molecule is the emission of sufficient light. Secondly, the lifetime should be compatible with the phenomena of interest. As previously mentioned, quenching can significantly affect the phosphorescence lifetime of a molecule, so it too should be considered. One should also keep in mind the complexity of the synthesis of each solution, since chemical equipment might not be readily available within our lab and a substantial amount of the solution could be necessary.

Most of these requirements are met by some of the so-called lanthanide complexes, and the use of one of these for droplet tracking has been successfully demonstrated [45]. The lanthanides (from Lanthanum) or rare earth metals, are the elements with partially filled 4f shell, which form stable trivalent cations, e.g. Ln^{3+}.

Direct excitation of the ions proves to be difficult, but can be overcome by making use of complexation, a typical feature of metal ions. The metal ion is then surrounded by so-called ligands, typically organic molecules. The complex thus consists of one or more metal centers and multiple ligands. Weissmann was the first to note the effect of complexation as well as the importance of solvent and temperature on Europium luminescence in 1942 [73]. Much follow-up research has been performed since.

The various lanthanide elements emit at different wavelengths, ranging from the ultraviolet (Gd^{3+}) to the visible (blue, Tm^{3+}; green, Tb^{3+}; yellow, Dy^{3+}; orange, Sm^{3+}; red, Eu^{3+}) to the near infrared (Yb^{3+}, Nd^{3+} and Er^{3+}). Several review articles concerning the quenching [74], the energy transfer and various ligands [75] and design [76] of luminescent lanthanide complexes are available. For the current study, we use Europium due to its ease of prepara-

tion, well-separated excitation and emission wavelengths and the availability of a light source with the required excitation wavelength ($\lambda_{ex} = 355$ nm).

4.3.2 Sample preparation

The light-emitting Europium molecule Eu^{3+} is docked within one or more ligand molecules, which serve as antennae to absorb energy from the laser beam and transfer it to the lanthanide, which in turn emits this energy as photons with a wavelength $\lambda_{em} = 613$ nm. The ligands used in this solution were thenoyltrifluoroacetone (TTA), which has a strong absorption peak at 355 nm, and trioctylphosphine oxide (TOPO). Although the stoichiometric composition of the solution was found to be $Eu(TTA)_3(TOPO)_2$ by Arnaud and Georges [77], it was also concluded that phosphorescence reached a maximum when the concentration of TTA was at least ten times that of Europium. This is beneficial to our method since a stronger phosphorescent signal allows for a longer tracking of the droplets. With this in mind, the solution used in the present study was prepared taking the 10:1 ratio into consideration.

Two solutions were prepared and tested to assess dependence of signal intensity and decay on the concentration of the ingredients. Before preparing the working solutions, stock solutions for each of the three components were mixed separately. The Europium stock solution used distilled water as a solvent and Europium(III) chloride hexahydrate, while the TTA and TOPO solutions used ethanol; all stock solutions have a concentration of 10^{-2} M. The working solutions used in the measurements were prepared by mixing demineralized water with the necessary amount of each ligand solution. The Eu^{3+} was added first, followed by the TTA and finally the TOPO, which did not fully mix, creating a milky appearance. Finally, to clear the solution and serve as a wetting agent, 0.1% $\sqrt{v}$ of Triton X-100 was added. The concentration of the components in the solutions is presented in Table 4.1 below.

Solution	Eu^{3+} 10^{-5}M	TTA 10^{-4}M	TOPO 10^{-4}M
1	8.3	8.3	8.3
2	1	1	1

Table 4.1: *Concentration (molarity) of the components of the analyzed solutions.*

4.3.3   Signal intensity and saturation

Following on the characterization of the phosphorescent solution we test phosphorescence intensity as a function of laser power as well as any self-quenching effects on the decay constant. Saturation must be considered to avoid using excess energy which could be scattered outside the cross section of the laser beam resulting in widening or blurring of small features in the tagging pattern. This, of course, depends on the scales of interest for each particular experiment.

The measurements consisted on creating a light sheet with a pulsed Nd:YAG laser (Powerlite Precision II 8010, Continuum, Santa Clara, CA) to illuminate droplets and recording the phosphorescent signal using an intensified high-speed camera (HiCAM 5000, Lamberts Instruments, Roden, The Netherlands). The laser beam power was measured using a thermopile power sensor (Coherent model PM10V1). Approximately 600 sequences of ten frames each were recorded. The measurement was repeated for six different power settings on the laser. The sequences were phase-averaged and the intensity as a function of time was fitted with an exponential function. No apparent effect of the laser power on the decay constant was evident. The values of τ_{ph} fluctuated around 654 μs without a particular trend, with the maximum variation being approximately 6% of the mean. Figure 4.5(a) shows the decay of the phosphorescence intensity of the case with power setting of 616 mW. The signal to noise ratio is considerably reduced in the final data points, resulting in a standard deviation with a higher value than the mean. Because of this, error bars must be truncated when plotted on a logarithmic scale.

The intensity as a function of power shows a clear saturation trend. This effect can be seen in Figure 4.5(b). Even though at the maximum tested laser power a slight increasing trend can be observed, the intensity increases marginally as the power is raised. The intensity was determined by averaging over a small region of the frame (this helped increase the signal-to-noise ratio).

The first data point in all of our decay measurements was consistently higher than the fitted curve (see Figure 4.5(a)). This suggests a double exponential trend as a result of a secondary process (possibly fluorescence). We believe this does not significantly affect any of our results since the timescale involved is much shorter than any timescale of the flow.

Both solutions show an almost identical decay constant, however, the intensity of the signal increased substantially with higher Europium concentra-
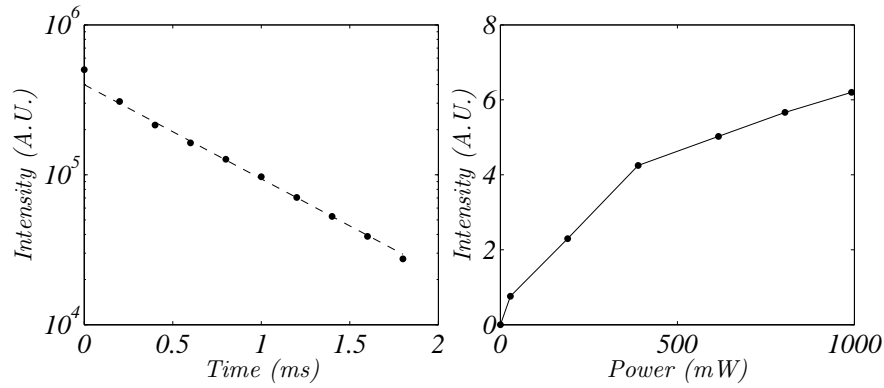
Figure 4.5: *(a) Phosphorescence intensity as a function of time for case with power of 616 mW, resulting in $\tau_{ph} = 691\,\mu s$.(b) Phosphorescent signal intensity as a function of laser power for solution 1. Error bars for both cases are on the order of the symbol size.*

tion. When using solution 2, writing well defined volumes was not possible, given the lower saturation threshold. That is, droplets outside the cross section of the laser beam receiving only stray light had a similar intensity as those within the beam. After this analysis, it was decided to use solution 1 for all dispersed phase measurements.

Imaging a dynamic luminescent signal can present a few challenges, particularly in regard to the exposure settings of the camera. If one has an excessively long exposure time the first few images could be overexposed, however, if one has a short exposure, the frames recorded further into the sequence may be too dark to yield any significant information. To counteract the signal decay, we exponentially increase the exposure time of the camera. This allows to record a longer sequence with a reduced difference in the signal intensity. Two considerations must be addressed: 1) the possibility of imaging streaks due to the rapid movement of the droplets and 2) the maximum length of the exposure is tied to the frame rate of the camera. These concerns must be addressed specifically for each measurement, seeing that their effects are potential sources of error.

4.3.4   Phosphorescent tagging in continuous phase

Even though the present study is focused on the application of phosphorescent tagging in dispersed (droplets) phases, the Europium solution may be used as a flow diagnostic in continuous (liquid) phases. Using solution 1 from Table 4.1 above, we inspect the behavior of the phosphorescent signal as a function of power and the spatial uniformity of the emitted signal as a beam traverses it.

We fill a $(2{\times}3{\times}4\ cm^3)$ cuvette with phosphorescent solution 1, illuminate it with a pulsed laser beam of approximately 8 mm diameter, and record the intensity of the phosphorescent signal using an intensified camera with an exposure time of 500 ns. To reduce noise and beam inhomogeneity effects, we average the intensity values over a narrow rectangle (Figure 4.6(a)) as well as only the incoming or outgoing half of the rectangle. The procedure is repeated over a range of powers.
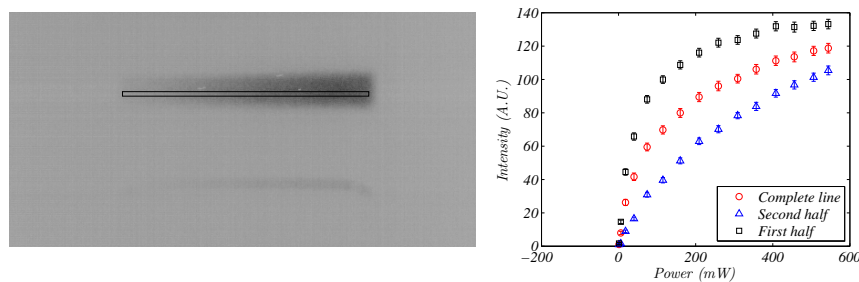

Figure 4.6: *(a) Excerpt of the image of tagged liquid in a cuvette showing the thin rectangle over which the intensity was averaged, (b) phosphorescence intensity as a function of power for solution 1. Error bars denote the standard deviation of the pixel values within the averaged region.*

It is evident from Figure 4.6 that intensity is lost as the beam traverses the fluid in the cuvette. Also, it can be seen that the solution in the incoming side of the cuvette quickly saturates. Similar measurements were tried with solution 2 (not shown), but the quick absorption of UV light by the solution due to the high TTA concentration hinders a comparison between measurements. The implications of these results are two: 1) a very high power laser or a very thin beam is necessary to write a line of uniform intensity across a continuous liquid phase and 2) low (high) Europium concentrations will allow (curb) the phosphorescent tagging across relatively long sections of continuous liquid.

4.4 Conclusions

Throughout this chapter we have presented the results of the characterization of the Europium-based solution used in our tagging experiments. There are multiple mechanisms applicable to molecular tagging velocimetry of which some use fluorescence and some phosphorescence, each with its benefits and disadvantages. Europium is one of many lanthanides that can be used for MTV. Its decay constant in the particular solution used here, $\tau_{ph} \approx 650\,\mu$s, appears to be a good match for the timescales of interest in our turbulent flow (see Section 2.1). The intensity of the phosphorescence allows us to obtain approximately 2 ms of data, which is approximately equivalent to $5\tau_{\eta}$.

We have also seen that concentration can play an important role in both dispersed and continuous phases. Less concentrated solutions are suitable for continuous phase tagging, while dispersed phases benefit from a more concentrated solution. In addition, the concentration appears to have minimal impact on the decay constant.

CHAPTER 5

DISPERSION OF HEAVY DROPLETS

Turbulent dispersion plays a crucial role in many natural and industrial processes. In nature, animals rely on the dispersion of scents to locate both mating partners and prey [1], while mushrooms rely on turbulence to get their spores transported away from their fruiting bodies [78]. In urban areas, the dispersion of pollutants produced by cars and factories is of interest due to health concerns [79]. Another important example is the dispersion of nuclear particles or chemical agents after catastrophic events. Although apparently similar, the above mentioned examples have fundamental differences that set them apart. For once, the dispersion of a passive scalar—an agent that opposes no resistance to the flow—can be considerably different than the dispersion of inertial particles. Furthermore, these cases can also be classified as either absolute or relative dispersion, depending on the reference frame used in the analysis.

Briefly, absolute dispersion is concerned with the concentration of the agent at a particular point in space, i.e. Eulerian frame. For example, the concentration of dye as a function of time and position after a small ink blob is released into a turbulent field. On the other hand, we have relative dispersion, where the relevant value is the distance between two particles, fluid or otherwise, as they are advected by the flow. This, of course, is based on a Lagrangian frame, since both particles are followed as they move around

the flow field without regard of their absolute position. An extension of the relative dispersion problem is the relative dispersion of a cloud or puff of particles, which could be seen as a collection of $N(N-1)/2$ pairs for a cloud of N particles, although in this case—depending on the size of the cloud—particle pairs may be correlated with each other, which appears to be different than taking many pairs that are uncorrelated from all other pairs.

Even though most of the examples presented above involve atmospheric dispersion, which in most cases is inhomogeneous and anisotropic, experiments in an idealized flow can provide insight into fundamental aspects of the dispersion phenomenon in general. In our experiment, we are able to create—without influencing the flow—a particle cloud within a turbulent field. This allows us to look at the dynamics of the concentration of particles. It must be noted, however, that the particles are not entirely passive, since their inertia is enough to resist the fastest accelerations in the flow. As we have seen in Chapter 1, dispersion has been of scientific interest for over 90 years [23]–[25]. In this chapter we will revisit this longstanding problem. In Section 5.1 we will give an overview of the existing background followed by a description of our experiment (Section 5.2). Next, in Section 5.3, we will present the outcome of our phosphorescence measurements, and complement these experiments with PIV of heavy particles (Section 5.4) and with numerical simulations (Sections 5.5 and 5.6). We will close the chapter in Section 5.7 with a summary of the results and concluding remarks.

5.1   Background

5.1.1   Absolute dispersion

The problem of turbulent dispersion was first addressed by G.I. Taylor [23] in his classical paper *Diffusion by continuous movements*, where he explored the evolution of a scalar field within a turbulent velocity field. In his study, Taylor argues that the role of molecular diffusion is so small compared to that of turbulent diffusion, that it can be neglected. This assumption allows scalar particles to be treated as fluid particles, translating into the possibility of approaching the issue through the probability density function of the Lagrangian position of the fluid particles.

For a point source, the probability $f_x(\boldsymbol{x}; t|\mathbf{Y}_0)$ that a fluid parcel is found at $\boldsymbol{x}$ at time t, given it was at $\mathbf{Y}_0$ at $t = 0$ is equal to the density $\phi(\boldsymbol{x}, t)$ of a

scalar released from the origin. We are interested in the moments of f_x. The probability density f_x can be physically interpreted in the following way: if at time $t = 0$ we release a blob of dye from a point $\mathbf{Y}_0$ then, as time progresses, we would see the blob expanding in such a fashion that the amount of dye along any straight line crossing $\mathbf{Y}_0$ would have a profile equal to the PDF $f_x(\boldsymbol{x}; t | \mathbf{Y}_0)$.

The second-order moment of the particle position $\langle x_{ii}^2(t) \rangle$ follows from the dynamics $x_i(t) = x_i(0) + \int u_i(t') \, \mathrm{d}t'$,

$$\langle x_{ii}^2(t) \rangle = \langle x_{ii}^2(0) \rangle + 2 \int_0^t \int_0^t \langle u_i(t') u_i(t'') \rangle \mathrm{d}t' \mathrm{d}t'', \qquad (5.1)$$

where $\langle x_{ii}^2(0) \rangle$ can be interpreted as the squared size of the initial cloud. Assuming stationarity of the turbulence statistics, $\langle u_i(t') u_i(t'') \rangle$ depends only on the time difference $t'' - t'$, and

$$\langle x_{ii}^2(t) \rangle = \langle x_{ii}^2(0) \rangle + \langle u_i^2 \rangle \int_0^t (t - s) R_{ii}(s) \mathrm{d}s, \qquad (5.2)$$

with the Lagrangian velocity autocorrelation function defined as

$$R_{ii}(s) = \frac{\langle u_i(s) u_i(0) \rangle}{\langle u_i^2 \rangle}. \qquad (5.3)$$

For very short times ($s \ll T_{ii}$) the normalized correlation function $R_{ii} \approx 1$, and the dispersion proceeds ballistically,

$$\langle x_{ii}^2(t) \rangle = \langle x_{ii}^2(0) \rangle + \langle u_i^2 \rangle t^2, \qquad (5.4)$$

while for very long times t,

$$\langle x_{ii}^2(t) \rangle = \langle x_{ii}^2(0) \rangle + 2\langle u_i^2 \rangle T_{ii} t. \qquad (5.5)$$

where $T_{ii} = \int_0^\infty R_{ii}(s) \mathrm{d}s$ is the Lagrangian integral time, also known as the large-eddy turnover time.

The above relations apply to fluid parcels, and their accuracy in describing trajectories of heavy droplets is not guaranteed, given that inertial particle trajectories deviate from those of tracers. Particle velocity fluctuations are expected to be smaller than its fluid parcel counterpart due to the smoothing effect of the increased reaction time originating from the inertia. The Stokes

number quantifies the inertia of a particle. Higher Stokes numbers indicate a larger reaction time, whereas tracers have Stokes number zero.

Evident from the above analysis is the fact that the autocorrelation function lies at the core of the dispersion problem. Prompted by this premise, Snyder & Lumley [31] studied the autocorrelation function of heavy particles within grid turbulence in a vertical wind tunnel. Particles with different densities (glass, pollen and copper) and diameters (47 and 87 μm) were used in order to explore the autocorrelation function of particles with equal Stokes number but different diameters and viceversa. This analysis concluded that the autocorrelation decreases much faster for heavier particles than it does for fluid tracers (47 μm hollow glass beads). The decrease was linked to inertia effects and a gravitational phenomenon referred to as 'crossing trajectories'. Inertia effects are the result of heavy droplets resisting sudden accelerations, thus filtering out the fastest scales in the flow. The crossing trajectories effect is observed when, due to the terminal settling velocity induced by gravity, a particle that otherwise would have remained within an eddy throughout its turnover time, crosses from one eddy to another, decorrelating itself from its initial velocity much faster. Due to the decaying nature of grid turbulence it was not possible to characterize the particles with a single Stokes number, but an estimate gives St ≈ 0.15 for the hollow glass spheres and St ≈ 4.22 for the copper particles, on average.

A correction of the autocorrelation function was necessary given the decaying nature of grid turbulence. The adjusted values show a considerable decrease in the autocorrelation of particles as their inertia increased. The particle dispersion also saw a decrease. It must be noted that the terminal settling velocity of the heavier droplets was over three times the turbulent velocity fluctuations, which can have a considerable impact on droplet behavior, for example, preferential sweeping [30, 29]. In our experiments, the heaviest droplets have a settling velocity of approximately 1% of the turbulent velocity fluctuations.

Many other studies have been dedicated to the analysis of dispersion of heavy particles (see [14] and references therein), but most of them have focused on times $t \sim T_L$. Such studies agree on the conclusion that heavy droplets may disperse faster than their massless counterpart due to the effects observed by Snyder & Lumley [31]. The question is: at times $t \sim \tau_\eta$, will heavy particles disperse faster or more slowly than tracers? It is the aim of this chapter to look at the dispersion of heavy droplets at the shortest timescale of the flow, namely the Kolmogorov timescale. We wish to quantify the dif-

ference in the dispersion of heavy droplets versus the theoretical expectation of fluid particles with zero diffusivity. To do this, we set up an experiment using the aforementioned phosphorescent tagging method (Chapter 4).

Before we engage in the experimental details, let us consider three instances in the Stokes parameter space to aid in the understanding of the effects increased inertia brings with it. When St→0 the autocorrelation of tracers and particles is identical. As the Stokes number becomes finite, there are two competing forces affecting the autocorrelation: since inertia prevents sudden changes in velocity, the value of $R^{(p)}$ tends to increase with inertia. However, the converse is true for the crossing trajectories effect.

These two counteracting effects are influenced differently by inertia, meaning that one may overpower the other as inertia is further increased. Lastly, for particles that are very massive (St $\rightarrow \infty$) $R^{(p)}(t) = 1$ and $R^{(f)}(t)$ becomes the Eulerian autocorrelation function since the particle becomes insusceptible to changes in the flow, maintaining its velocity for longer periods of time. These effects will obviously modify the dispersion statistics of heavy particles, nevertheless, the quantification of this difference remains unanswered.

The great advantage of our tagging technique is that creating the initial condition does not perturb the flow, unlike the experiments by Gopalan [32], where drops of light fluid were injected into the turbulent flow. Nevertheless, some aspects of the initial condition must be considered. Naturally, our initial puff of particles is not point-like, but has the shape of a sausage. The droplets within this cylinder are not a collection of independent point-sources, as the length of the cylinder can be compared to the integral length scale. This may influence the rate of increase of the width of the cloud. Moreover, the cloud spans the entire frame along its axial direction, which may also cause an artificial widening when the sausage is smashed along its axis due to influence of the large-scale flow fluctuations. Finally, the tagged droplets already partook in the turbulence, which implies they may have undergone preferential concentration, and may sit in regions of the flow that have a rate of strain which is different from the average [19]. Therefore, the spreading of a tagged cloud provides a biased view of dispersion compared with a cloud which is initialized freshly.

5.1.2   Relative dispersion

Our analysis is mostly based on absolute dispersion, i.e. in the Eulerian frame of reference. For completeness, however, we will give a brief overview of relative dispersion. For an in-depth review, we refer the reader to recent reviews by Sawford [80] and Salazar & Collins [81].

Richardson's seminal paper [24] set the foundation for the study of relative dispersion; both the separation of a particle pair as well as the statistics of this value for a cloud of particles were addressed as diffusion of a passive scalar. In this study it was concluded that the mean square separation

$$\langle \Delta(t)^2 \rangle = (r_1(t) - r_2(t))^2, \tag{5.6}$$

would grow as t^3. This conclusion was later refined by Obukhov [82], finding a dependence on the dissipation rate ε, resulting in

$$\langle \Delta(t)^2 \rangle = g\varepsilon t^3, \tag{5.7}$$

where g is a universal constant. Neither of the above authors included the initial separation as a variable in their studies, which proved essential when within the inertial range.

It is known that the velocity of two neighboring fluid parcels will be correlated for a time comparable to the turnover time of the largest eddies of the flow T_L. This introduces a 'memory' effect to the fluid parcels. Within the inertial range, two particles situated a distance Δ_0 apart will remember for a time comparable to the turnover time of an eddy size $l_0 = \Delta_0$. Meaning that it will take longer for them to forget their initial relative velocity as their initial separation is increased. To account for this memory effect, Batchelor [25] resorted to the second-order Eulerian structure function to develop a relation in which the initial separation of the fluid parcels plays a role in the growth of the distance between them, and only after time $t_0 = (\Delta_0^2/\varepsilon)^{1/3}$ will the Richardson-Obukhov scaling be observed. For $t < t_0$, Batchelor's prediction is

$$\langle [\Delta(t) - \Delta_0]^2 \rangle = \frac{11}{3} C_2 \left(\varepsilon \Delta_0 \right)^{2/3} t^2, \tag{5.8}$$

where C_2 is the constant found in the second-order structure function and has an approximate value of 2.1.

Recently, an experimental study performed by Bourgoin et al. [26] confirmed the existence of the Batchelor scaling and was able to detect a

Richardson-Obukhov scaling for a very limited number of cases. It was suggested that in order for the t^3 scaling to be observed over an ample range of initial separations, a large difference between the three relevant timescales T_L, t_0 and τ_k was necessary. Also, it was stated that even in the most turbulent flows encountered in nature ($Re_\lambda \sim 1000$), the separation of these timescales scales would be modest.

Bec et al. [18] performed a numerical study of the dispersion of tracers and heavy particles in a turbulent flow over a range of St and initial separations. Their initial separations ranged from $l_0 < \eta$ to $l_0 = 6\eta$. They used such low initial separation values to assess the impact of caustics in the evolution of $\Delta(t)$. A noteworthy result is that the tracers show no sign of a Batchelor regime ($\propto t^2$) for either separation, going into a Richardson regime ($\propto t^3$) after 10η. This does not agree with the findings of Bourgoin et al. [26]. However, this difference might arise due to the relatively large initial separations ($\sim 10\eta$) in the experiment. Smaller initial separations result in smaller t_0, allowing the particles to 'forget' their initial correlation, and enter Richardson's regime more quickly.

5.2 Experiment and data processing

The experiment consists of filling the turbulence chamber with phosphorescent droplets and tagging a narrow cylindrical volume using a laser. As the glowing droplets are advected by the flow, images are recorded, allowing us to follow the droplets emerging from this 'line-source'.

Tagging is done using a high-power, frequency tripled Nd:YAG pulsed laser (Powerlite Precision II 8010, Continuum, Santa Clara, CA) at a rate of 10 Hz and a power output of approximately 120 mJ/pulse (355 nm wavelength). The recording begins 0.5 μs after the laser shot, for which an intensified CMOS camera was used (HiCAM 5000, Lamberts Instruments, Roden, The Netherlands). The intensifier is necessary due to the low light intensity emitted by the glowing droplets. The signal intensity is further reduced by the short exposure time derived from the high frame rate. The recordings have a frame rate of 5000 FPS with a 512×512 pixel^2 resolution. The field of view is a 32×32 mm^2 window, resulting in a magnification of 64 μm/pixel.

The tracking of the particles is not meant in a strict sense as in PTV. Rather, it is the signal intensity of the images which is used to determine the width of the cloud as a function of time. For every case, a series of 3275

sequences is recorded, each containing 18 frames. This procedure is repeated
for different Stokes numbers to estimate the effect inertia will induce. The
particle diameters for each case, together with the resulting Stokes number,
are listed in Table 5.1. As mentioned in Section 3.2.3, there are slight differ-
ences in the turbulence statistics among cases due to the fine-tuning necessary
to balance the speaker forcing with the perturbation created by the spinning
disk aerosol generator.

Case	1	2	3	4	5
d_p (μm)	11.0	15.4	16.5	18.8	21.9
St	0.95	1.67	1.86	2.43	3.15

Table 5.1: *Particle diameter and resulting Stokes number for each one of the
studied cases. Information about the turbulence statistics is presented in Chapter
2.*

The concentration of droplets is estimated with two different procedures.
The first one consisted of counting droplets from PIV-like images. Each im-
age is processed with a particle locating algorithm from which an average
quantity is obtained. The volume is approximated by the area of the field of
view and the thickness of the laser sheet. This yields a mean inter-particle
separation of approximately 30 particle diameters. This method, however,
cannot distinguish between primary and satellite droplets, since it uses diffrac-
tion (not phosphorescence) to image particles, making satellite particle detec-
tion possible. Nevertheless, we are interested in the concentration of primary
droplets. Additionally, we believe that satellite droplets are small enough to
be disregarded in our volumetric fraction calculation. The signal intensity of
phosphorescent particles is proportional to their volume, that is, d_p^3, therefore
we expect the phosphorescence signal intensity of satellite droplets to be less
than 30 times that of primary droplets, thus having little effect in our analysis.

A second method, which is more appropriate for the scenario at hand, is to
determine the particle concentration from the approximate number of droplet
collisions with the wall. Since the signal intensity of our data remains rel-
atively constant throughout the experiments, this means that the number of
collisions per second is approximately equal to the number of droplets gen-
erated in the same time. The feed rate of liquid to the aerosol generator Q is
known, therefore we can estimate the number of droplets generated (assuming
all the liquid is used in primary droplets). From kinetic theory we can readily

prove that the number of collisions to the wall N_c can be approximated by

$$N_c \approx \frac{v A_{ch} n}{2\pi^{1/2}},$$ (5.9)

where v is the *rms* velocity of the particles, A_{ch} is the area of the walls of the chamber, and n is the particle density. By equating Eq. (5.9) to the number of droplets generated $N_g = Q/(\pi d_p^3/6)$, we estimate the particle density to be 172 particles/cm^3. This is equivalent to a volume fraction of approximately 7.2×10^{-7}. This value falls under one-way coupling according to Sommerfeld [83]. From the volume fraction, we estimate an average inter-particle distance of approximately 90 particle diameters. We see that the particle counting method overestimates the volume fraction of droplets, and as such, it is not suitable to our circumstance. The big difference between the two methods is that even though satellite droplets have a tiny volume in comparison with primary droplets, they are still detected by the particle detection algorithm.

In Chapter 4 we addressed the characteristics of the phosphorescent solution, where it was shown that it has an exponential intensity decay. To counteract the decaying intensity of the glowing droplets we use a Field Programmable Gate Array (FPGA) board, which externally controls the intensifier gate time. This allows us to exponentially increase the exposure within a sequence in order to compensate for the decrease in the intensity of the phosphorescence. For all five cases the first frame has an initial exposure time $\tau_0 = 40\,\mu$s. The exposure time is increased exponentially in the following frames proportional to the phosphorescence lifetime $\tau_{ph} \approx 691\,\mu$s. Once the exposure time reached the limit set by the frame rate (200 μs at 5 kHz), the exposure time was held constant at 199.5 μs, 0.5 μs less than the inter-frame time.

The data was processed in a phase-locked fashion, that is, the nth frame of each sequence (where $n = 1, 2, \cdots, 18$) is superimposed with the corresponding frame of every sequence in the entire series. After all sequences have been accounted for, an average is obtained for each time delay within the sequence. Figure 5.1(a) shows a single shot of the tagged volume. Because of the intensity decay in time, the signal to noise ratio is dramatically reduced as the end of the sequence is approached, which can have an impact on the fit quality. To increase the signal-to-noise ratio, each image from the averaged sequence is further averaged along the (horizontal) x-direction. Any streaking due to the relatively long exposure time does not affect the results, since, by superimposing all images, data about each particular droplet is lost.

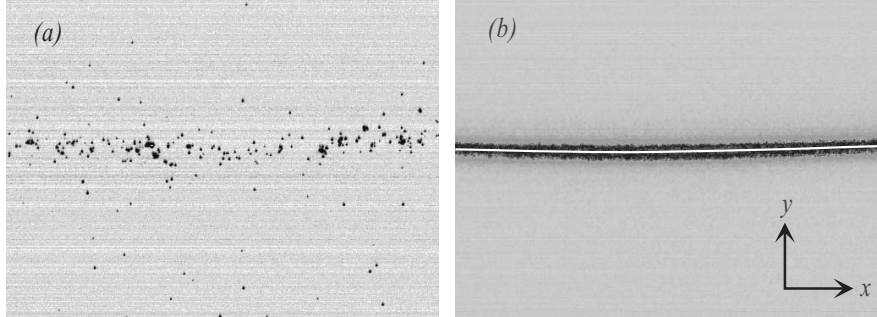The optical setup introduced aberrations resulting in a slight deformation

Figure 5.1: *(a) Single shot of the tagged volume. The sparseness of the droplets can be appreciated. (b) Resulting intensity map after phase-averaging showing the backbone (solid white). It can be observed that, due to optical aberrations, the line appears bowed. This is corrected by straightening the backbone and shifting the intensity profile accordingly.*

of the registered image, making the line appear bowed (Figure 5.1(b)). To avoid an artificial widening of the profile, this anomaly was rectified by finding the intensity peak along sections of the image in the x-direction, with every resulting peak becoming a node in the backbone of the line. The backbone was then aligned with the x-axis, resulting in a straight line .

In order to quantify the dispersion we want to measure a characteristic length scale of the tagged cloud as a function of time. The shape of the laser beam sets the initial intensity profile, which may or may not be Gaussian. In the case of a Gaussian profile, the two-dimensional projection is also a Gaussian profile, however, other beam shapes translate into more complex profiles.

A diffusive process evolves in a Gaussian fashion. In the present study, we expect to see diffusive spreading of the tagged cloud. If our initial condition is given by some profile $P(y, z)$, the evolution of the profile will follow

$$I(y, z) = \frac{1}{\pi \sigma^2} \int P(y', z') \exp\left(\frac{-(y - y')^2 - (z - z')^2}{\sigma^2}\right) \mathrm{d}y' \, \mathrm{d}z',$$

where x, y and z follow a right-handed coordinate system as in Figure 5.1(b). Because of experimental setup limitations, we have no information about the depth (z-direction) of the cloud, so that we must integrate the above equation over z, to obtain

$$I(y) = \frac{1}{\pi^{1/2} \sigma} \int P(y') \exp\left(\frac{-(y - y')^2}{\sigma^2}\right) \mathrm{d}y', \qquad (5.10)$$

where $P(y) = \int P(y, z)\mathrm{d}z$. In general, the projection of a rotationally symmetric profile is called an Abel transformation. For arbitrarily widening sausages, an initial radial profile must be determined through the inverse Abel transform, after which the temporally evolved profile must be compared to the experiment through a forward Abel transform. For Gaussian spreading, this tedious procedure can be circumvented, as Eq. (5.10) demonstrates.

The initial profile in our experiments is not exactly a Gaussian, but could be represented well by a Voigt profile, which is the convolution of a Gaussian and a Lorentzian,

$$P(y) = A_p \frac{\gamma}{\sigma_0 \pi^{3/2}} \int_{-\infty}^{\infty} \left(\frac{1}{\gamma^2 + (y - y')^2} \right) \exp\left(\frac{-y'^2}{2\sigma_0^2} \right) \mathrm{d}y',$$

where A_p gauges the intensity and σ_0, γ are the parameters that were determined from the initial profile using a least squares procedure. Substitution in Eq. (5.10) results in

$$I(y) = A_p \frac{\gamma}{\sigma^2 \pi^{3/2}} \int \frac{1}{\gamma^2 + y'^2} \exp\left(\frac{-(y - y')^2}{\sigma_0^2} \right) \mathrm{d}y', \qquad (5.11)$$

where we have trivially replaced $\sigma^2(t) + \sigma_0^2$ by $\sigma^2(t)$. At later times we must determine A_p and σ, and, in addition, allow for a background B and a shift y_0 of the line due to a residual mean velocity. Because of the decaying phosphorescence the integrated line intensity A_p decreases exponentially in time, after correcting for the increasing exposure intervals. Also the background (dark) intensity increases slowly during the lifetime of the tagged pattern. Summarizing, a least-squares fit provided the time-dependent values of σ, y_0, A_p, and B.

5.3 Experimental results and discussion

We expect the dispersion of heavy droplets to deviate from that of fluid tracers as a result of droplet inertia. As the Stokes number increases, we anticipate these effects will become more apparent. In the Eulerian frame, we foresee a t^2 dependence of the widening of the phase-averaged cloud. Figure 5.2 shows the phase-averaged intensity profile of the cloud for the first six time steps of case 5 (St $= 3.15$). We can see that the quality of the fit is very good, which is true for all cases; however, these are not shown for brevity.
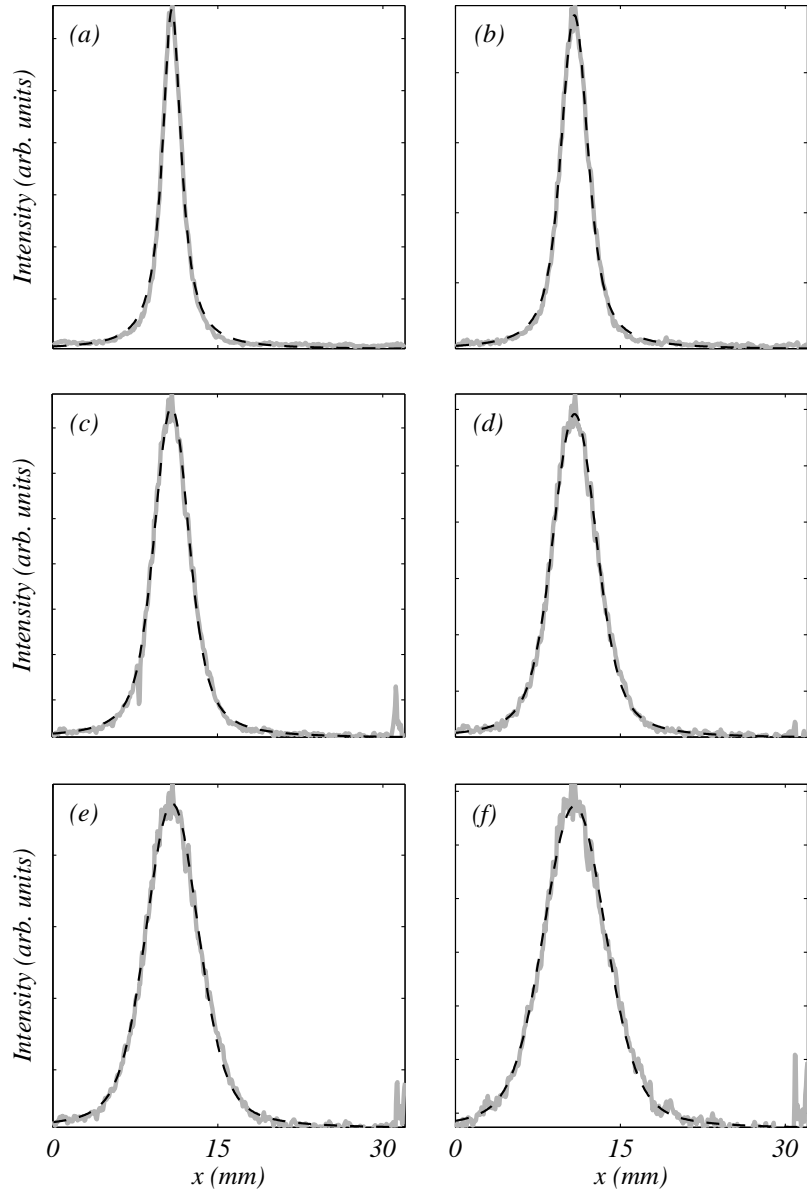
Figure 5.2: *Cloud profile (solid line) and corresponding fit (dashed line) for case 5, (a)–(f) for time steps corresponding to $t = 200$–$1200\,\mu s$ in increments of $200\,\mu s$.*

We quantify the width of the line with $\sigma^2(t)$, as defined in Eq. (5.11), however, we subtract the initial width σ_0^2 for easy comparison among cases (see Figure 5.3). Clearly, $\sigma^2(t)$ increases proportional to t^2, $\sigma^2(t) - \sigma_0^2 = v_s^2 t^2$, where v_s is the spreading velocity. For fluid tracers, v_s is the turbulent velocity u. Below, we will discuss a similar experiment which follows true fluid tracers. As Figure 5.3 demonstrates, v_s is always larger than the turbulent velocity u, and reaches a maximum at St ≈ 2.

An outstanding result is the appearance of a peak in the dispersion as a function of Stokes number. In Figure 5.3(b) it can be observed that the particles with the lowest and highest Stokes number show a significantly slower dispersion than the particles with intermediate inertia. This suggests an optimum dispersion at St ≈ 2. The mechanism behind the faster dispersion is unclear, as it is well established that the rms velocity of heavy particles is lower than that of fluid tracers.
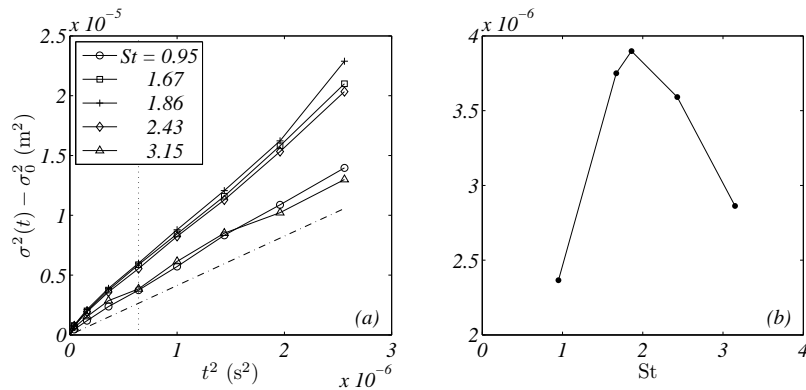
Figure 5.3: *(a) Cloud width as a function of time $\sigma^2(t) - \sigma_0^2$ for different Stokes numbers. Dotted line marks $t \approx 1.6\tau_\eta$. (b) Cloud width as a function of Stokes at $t = 800\,\mu s$ indicated by the dotted line.*

Before discussing this remarkable result, let us first describe the analogous fluid-particle experiment. In this experiment, we create a thin line of nitric oxide (NO) molecules in air with an excimer laser using a technique which has been described elsewhere [84]. These NO molecules, which are faithful tracers in air, are then made visible using fluorescence induced by a second (dye) laser, whose beam is expanded wide enough to embrace the tagged line as it has been deformed by the turbulent flow. The initial profile is Gaussian (i.e. $\gamma = 0$), but otherwise the analysis of this experiment proceeds in exactly

the same way. The result is shown in Figure 5.4. At $t \sim 2\tau_\eta$ the line has widened so much that the slightly non-homogeneous profile of the dye laser becomes visible. In this experiment the spreading velocity $u_s/u \simeq 1.05$.
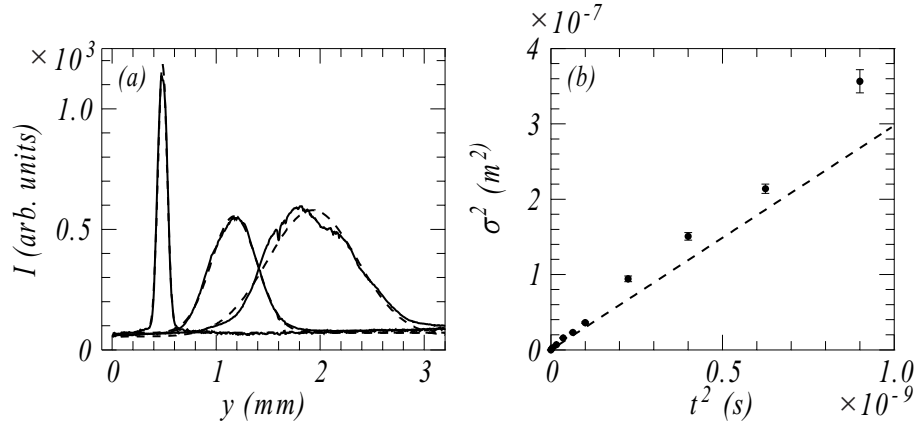

Figure 5.4: *The width of averaged lines in a fluid tracer experiment as a function of the delay time t between writing and reading. (a) Full lines are measured profiles at $t = 0.2, 15$ and $30\,\mu s$ ($t/\tau_\eta = 0, 1.1, 2.1$). Dashed lines are Gaussian fits $I(y) \propto \exp(-y^2/\sigma^2)$. (b) Dots are widths $\sigma(t)^2 - \sigma(0)^2$, dashed line is $\sigma^2(t) - \sigma_0^2 = 2\,u^2\,t^2$, with $u = 12\,m/s$.*

For droplets, Figure 5.5 shows that the ratio v_s/u may reach $v_s/u \approx 1.5$. This is a surprising result, since it is commonly believed that the fluctuating particle velocity $\langle v_s \rangle \leq \langle u_{rms} \rangle$ as a result of the filtering effect of inertia. We estimate v_s by fitting a function to the quantity $\sigma(t) - \sigma_0$. It can be seen that in all of the cases $\langle v_s \rangle > \langle u_{rms} \rangle$.

Even though there are fundamental differences between the study performed by Gopalan et al. [32] and our experiments, we can resort to their results to obtain clues regarding this anomaly. They found the turbulent velocity fluctuations of diesel droplets to be up to 10% higher than those of fluid tracers. This also contradicts the common notion that the $u_i > v_i$. The two main differences between the studies are the size of the droplets in comparison to the Kolmogorov length scale η and the effect of buoyancy.

The size of the droplets can have considerable repercussions on the dynamics of the particle, as more of the forces outlined in the equation of motion of a sphere (Eq. (1.10)) become important. In our experiments, the value of η remains close to constant. However, the droplet diameter doubled from the lowest to the highest Stokes number. For $d_p \approx 20\,\mu m$, $d_p/\eta \approx 1/4$, which may
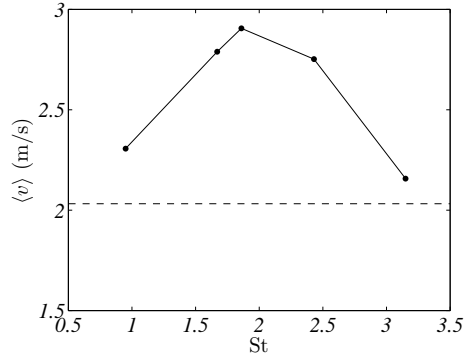
Figure 5.5: *Spreading velocity of droplet v_s (symbols) compared to the turbulent velocity fluctuations (dashed). We see that the difference reaches almost 50% for case 3 ($St \approx 2$).*

not be low enough for a point-particle approximation. Two of the neglected forces in the Maxey & Riley equation are affected by the droplet size. The Faxén correction accounts for the local curvature of the velocity field, which can induce lift forces on the droplet. For highly turbulent velocity fields the effect of the Basset history force, which accounts for transients in the development of the boundary layer around the particle, can be challenging to calculate, and is usually neglected or estimated using models of particles in chaotic fields. However, it has been pointed by Daitche & Tél [10] that the history force may become important even for relatively large, heavy particles.

In the case of diesel drops, the added mass becomes important, given the density ratio between diesel and water is close to unity. We do not expect this term to affect water droplets in air given such high difference between the densities of these fluids.

Another explanation may be that a tagged cloud gives a biased sampling of droplet, a bias induced by preferential concentration. At the moment the cloud is tagged,the droplets are not homogeneously distributed. The droplets have been suspended in the flow for a relatively long time, and the effects of turbulence may have become apparent in the form of droplet agglomeration in regions of high strain [19]. These regions have a higher stretching rate [27], which could result in faster separation of droplet clouds.

5.4   PIV of heavy particles

A complementary experiment that may help explain the faster dispersion of heavy particles was the measurement of the velocity field of droplets through particle image velocimetry. The setup for this experiment is exactly equal to that explained in Chapter 2, and only case 2 was analyzed. Measurements under the exact same conditions were performed for tracers (smoke) and heavy particles. A remarkable difference was found in the structure functions and, consequently, in the energy dissipation rate. Additionally, a slight increase was seen in the turbulent velocity fluctuations of the heavy droplets as compared to tracers.

The *rms* velocities saw a slightly anisotropic increase, with a higher increase in the vertical than in the horizontal direction—possibly due to gravity. The magnitude of the increase was approximately 5% and 10%, respectively. This modest increase, however, cannot explain the increase of the energy dissipation rate, which amounted to almost 80%. This increase in the dissipation rate, we believe, can be explained by the increase in the velocity differences (structure functions), shown in Figure 5.6, which is in agreement with the findings of Bec et al. [85], and can be explained by the existence of caustics in the particle velocity field. Such singularities manifest themselves as particles with finite velocity differences even when their separation approaches zero.
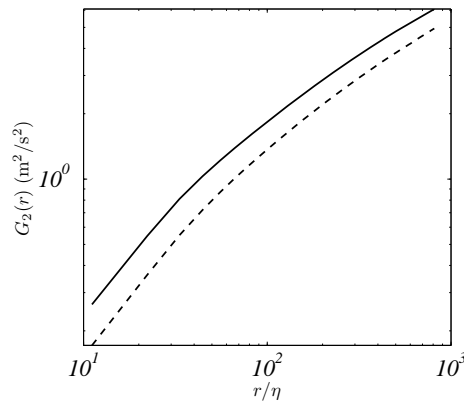

Figure 5.6: *Comparison of structure functions of tracers (dashed) and heavy (solid) droplets. The increase in velocity differences may be explained by the appearance of caustics in the particle velocity field.*

As we have seen in Section 5.1, the cloud width $\sigma(t)$ depends on the turbulent velocity fluctuations, so higher *rms* velocities translate into faster dispersion. Nevertheless, the increased velocities experienced by heavy droplets are substantially lower than the spreading velocities seen in Figure 5.5, which cannot fully explain the rapid dispersion observed in our measurements. However, we believe the increase in velocity *differences* may, in part, explain the increase in dispersion, since droplets with higher relative velocities will more quickly increase their separation.

5.5   Numerical simulations

The dispersion of drops and fluid elements is described by the velocity correlation functions. The short-time dispersion, $\langle x^2 \rangle \sim t^2$, follows from the short-time behavior of the correlation function, while the long-time diffusive spread is related to the integral times of the correlation function. We can distinguish between the correlation of fluid-element velocities u, the fluid velocity at the position of the particle u_0, and that of the particle velocity v. For simple linear Stokes friction, it can be readily shown that [14]

$$\langle v(t+\tau)v(t) \rangle \equiv R^{(p)}(\tau) = \frac{1}{2\tau_p} \int_{-\infty}^{\infty} \exp\left(\frac{-|t'-\tau|}{\tau_p} \right) R^{(f)}(t')\mathrm{d}t', \quad (5.12)$$

which relates the particle velocity correlation function $R^{(p)}$ to the correlation of the fluid velocities at the location of the particle $R^{(f)}$ and where τ_p is the particle relaxation time, $\tau_p = (\rho_p d_p^2)/(18\mu)$.

At $\tau = 0$ we have the fluctuating velocity of the particle,

$$\langle v_{rms}^2 \rangle = \frac{1}{2\tau_p} \int_{-\infty}^{\infty} \exp\left(\frac{-|t'|}{\tau_p} \right) R^{(f)}(t')\mathrm{d}t'. \quad (5.13)$$

Since $R^{(f)}(0) = \langle u_0^2 \rangle$, this implies that $\langle v^2 \rangle \leq \langle u_{rms}^2 \rangle$. More specifically, if we assume an exponential form for the fluid correlation as seen by the particle, $R^{(f)}(\tau) = \langle u_0^2 \rangle \exp(-\tau/T^f)$, which defines T^f as the associated integral time, it can be shown readily that

$$\langle v_{rms}^2 \rangle = \frac{\langle u_0^2 \rangle}{(\tau_p/T^f) + 1}. \quad (5.14)$$

Using Eq. (5.12) it can also be readily shown that

$$\int_0^\infty R^{(p)}(t')\mathrm{d}t' = \int_0^\infty R^{(f)}(t')\mathrm{d}t'. \tag{5.15}$$

Since many of these quantities are not accessible in an experiment, it is useful and instructive to compute them from numerical simulations. To obtain numerical information, we resort to a set of data available in the iCFDdatabase (www.cineca.it), which consists of Lagrangian tracks of particles in homogeneous, isotropic turbulence with zero-mean flow for several Stokes numbers. A brief account of the details about the simulations will be given here, for more information the reader is referred to [18]. The turbulent velocity field is obtained through direct numerical simulations (DNS) using a pseudospectral method. It uses a grid of 2048^3 points with a $\mathrm{Re}_\lambda = 420$. The time resolution of the numerical experiment is $\tau_\eta/200$. The Lagrangian timestep is equivalent to $\tau_\eta/20$. Lagrangian tracks are calculated using the point-particle approximation (Eq. (1.11))

$$\frac{\mathrm{d}v_i}{\mathrm{d}t} = \frac{1}{\tau_p}(u_i - v_i).$$

Initially, the particles are seeded randomly throughout the flow and given the local fluid velocity. However, the particle statistics are calculated after a 'thermalization' period which allows the particles to forget their initial condition. The database includes the position of the particle, its velocity v and the velocity of the fluid at the position of the particle u_0. It also includes the instantaneous accelerations of the particle, however, we do not use this information. The turbulence statistics are shown in Table 5.2 below.

$\langle u_{rms} \rangle$	Re_λ	ϵ	η	τ_η	L	T_E
1.4	420	0.88	2.8×10^{-3}	2×10^{-2}	3.14	2.2

Table 5.2: *Particle diameter and resulting Stokes number for each one of the studied cases. Information about the turbulence statistics is presented in Table 2.2.*

From these data sets we calculate the autocorrelation function of the particle $R_{ii}^{(p)}(\tau)$ and of the fluid seen by the particle $R_{ii}^{(f)}(\tau)$. Additionally, using the case for $\mathrm{St} = 0$, we calculate the autocorrelation of a fluid tracer $R_{ii}(\tau)$.

We also calculate the cross-correlation between the fluid velocity and the particle

$$R_{uv}(\tau) = \frac{\langle u(0)v(\tau) \rangle}{\langle uv \rangle}, \tag{5.16}$$

which gives us information about the time it takes a particle to decorrelate from its surroundings.

5.6 Numerical results

The Lagrangian statistics of the flow are calculated with fluid tracers, i.e. $St = 0$. We also calculate statistics for seven other Stokes numbers: 0.16, 0.6, 1.0, 2.0, 3.0, 5.0, and 10.0. The velocity fluctuations of the fluid tracers $\langle u_{rms} \rangle = 1.4$. This is calculated by averaging over all three components $\sqrt{u_x^2 + u_y^2 + u_z^2}/3$. The velocity fluctuations of the particles $\langle v_{rms} \rangle$ and those of the fluid at the position of the particle $\langle u_0 \rangle$ are shown in Figure 5.7(a) as a function of Stokes number. As expected $\langle v_{rms} \rangle$ decreases considerably with inertia, while $\langle u_0 \rangle$ remains almost constant.

The prediction of Eq. (5.14) is shown in Figure 5.7(b) together with the measured velocity. The difference is substantial due to the fact that it lays on the assumption that the correlation $R^{(f)}$ has an exponential form. As the inertia increases the correlation moves away from this assumption and the difference between the prediction and the measurement increases substantially.
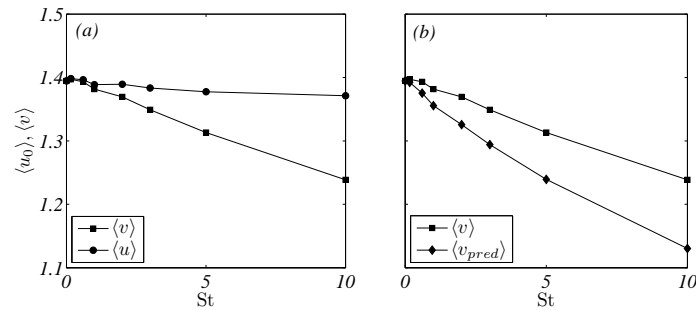
Figure 5.7: *(a) Velocities as a function of Stokes number. It can be seen that the velocity of the particle $\langle v_{rms} \rangle$ decreases with inertia, while the velocity of the fluid at the position of the particle remains (almost) constant. (b) Prediction of the particle velocity velocity from Eq. (5.14) and those measured from the simulations.*

Intuition tells us that a heavy particle will resist changes imposed by its surroundings. This means that the autocorrelation of a heavy particle should be higher than that of a fluid tracer. Figure 5.8 shows the autocorrelation for the particle and the fluid at the position of the particle. Our results agree with notion that the autocorrelation for particles is higher than that of a tracer, however, this is not entirely clear from Figure 5.8(a) due to the normalization with the corresponding integral timescale. Nevertheless, the inset of the figure shows a clear increase in the integral timescale $T^{(p)}$. On the other hand, the autocorrelation of the fluid velocity at the position of the particle—shown in Figure 5.8(b)—displays a different behavior. For small Stokes numbers, $R^{(f)}(\tau)$ increases with inertia, however, after a critical value is reached, we see a decrease in the correlation. This agrees with the notion of crossing trajectories, where a particle moves across eddies due to inertial effects. Even so, the crossover does not seem to affect the particle correlation, which keeps increasing with Stokes number.
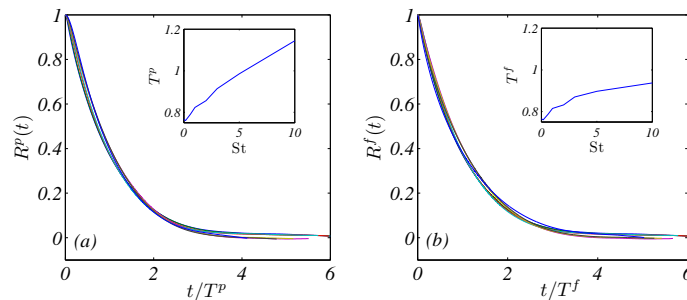
Figure 5.8: *Normalized Lagrangian autocorrelation function for particles (a) and fluid at the position of the particle (b) for the eight Stokes numbers analyzed. The time is normalized with the corresponding integral timescale for each case. Inset: Corresponding integral timescale as a function of Stokes as calculated from the integral of the autocorrelation function.*

The insets of Figure 5.8 show the corresponding Lagrangian integral timescales for particle and fluid. It can be seen that $T^{(p)}$ increases considerably with Stokes number. However, we expect this behavior to subside as inertia increases, reaching a saturation point. The saturation arises from the fact that as particles become heavier they are less susceptible to the fluid forcing. In the limit of infinite Stokes number the Lagrangian integral timescale becomes equal to its Eulerian counterpart T_E. A slight anomaly is observed in the first two points of this graph, where $T^{(p)}$ has a modest drop to later in-

crease again. We believe this is caused by the fact that the autocorrelation has not yet reached zero. The fluid velocity counterpart $T^{(f)}$ saturates much faster given the drop in correlation due to inertia effects. These results are in good agreement with those of Wang & Stock [14]. However, the Stokes values in their study are much higher.

The exact relation given by Eq. (5.15), implies that

$$T^p v^2 = T^f u_0^2. \tag{5.17}$$

This can be used to corroborate our results, given this relation is exact. These values are plotted in Figure 5.9 below, showing excellent agreement.
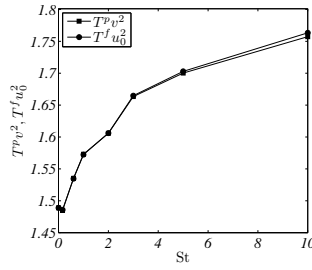
Figure 5.9: *Comparison of integral timescales as given by Eq. (5.17). The fit is excellent, and only at very large Stokes numbers can a small difference be seen.*
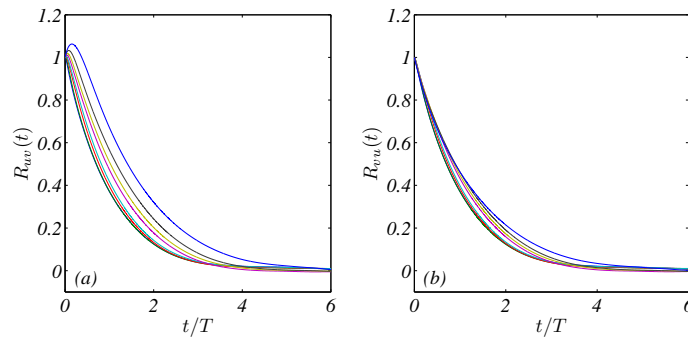
Figure 5.10: *Normalized Lagrangian cross-correlation functions (a) R_{uv} and (b) R_{vu}, respectively. Time has been normalized using the integral timescale for tracers T.*

The cross-correlation function gives us insight into the lag between the fluid and particle velocities. R_{uv} (Figure 5.10(a)) increases above 1.0 at short

times. This, we believe, happens due to the delayed response of the particle to the fluid forcing, that is, after a short time, the particle velocity adjusts to its surrounding, becoming more correlated to it. We should note that both the magnitude and the location of the peak shift with Stokes number. The forward movement is expected given the increase in reaction time. On the other hand, the complementary cross-correlation R_{vu}, does not suffer any notable changes.

None of the numerical results suggest a mechanism that may increase the dispersion of inertial particles. We see an increase in the particle velocity autocorrelation, however, there is also a reduction in the velocity fluctuations. Moreover, we do not observe any change that suggests an optimum Stokes number for dispersion at short timescales. Again, we believe, the dispersion of clouds—as opposed to single droplets—may introduce effects that increase the spreading velocity. Also, we have seen that relative dispersion of heavy particle pairs is, in some instances, faster that that of tracers. In our experiment, we cannot discriminate between absolute and relative dispersion. The puff is being advected by the large-scale velocities, but it is also widening due to the velocity differences between the droplets in the tagged cloud. As we have seen in Section 5.4, these differences are higher in the case of heavy droplets than in fluid tracers. Simulations on the dispersion of clouds of droplets would be beneficial for the physical interpretation of the phenomenon, however, the available database does not have the necessary density to replicate our experiments.

5.7   Conclusions

We have shown an experiment in which we tag a thin cylindrical volume (sausage) within a turbulent cloud of heavy droplets with predetermined Stokes numbers (diameters). In all five cases, the cloud of inertial particles disperses faster than the theoretical expectation for fluid tracers. Even more notable is the appearance of a peak in the dispersion at $St \approx 2$, which suggests an optimum Stokes number for accelerated dispersion. The physics behind the fast dispersion remain unclear. One reason that may help explain this behavior is the fact that heavy droplets preferentially gather in areas of high strain, which have higher stretching rates, and the preferential collinearity of the velocity and acceleration differences [19]. Nevertheless, more information is needed to pinpoint the cause behind this anomalous behavior.

To obtain more information about heavy particles we used numerical simulations from the iCFDdatabase. These show that the Lagrangian velocity autocorrelation of inertial particles increases with Stokes number. However, the autocorrelation of the fluid velocity at the position of the particle increases for low inertia and decreases as inertia increases above a critical point. Numerical results agree well with both numerical and theoretical literature, however, there is no indication that droplets could disperse faster than fluid tracers. Numerical simulations of cloud dispersion—a numerical recreation of our experiment—could help in the interpretation of our intriguing experimental results.

CHAPTER 6

DYNAMICS OF PREFERENTIAL CONCENTRATION

As has been previously mentioned, inertia effects create concentration inhomogeneities in the dispersed phase even when the carrier flow is homogeneous and isotropic. This anomalous behavior stems from the inability of heavy particles to faithfully follow the flow. Preferential concentration is known to impact many natural and industrial processes. Some examples that appear in nature include rain initiation in warm clouds [16, 3, 35], and sediment transport in rivers [86]; industrial processes such as spray drying [87] and fuel sprays ([33] and references therein) are also affected by the dynamics of particle–turbulence interaction.

Numerical, theoretical and experimental work consistently agree on the existence of such phenomena and, to a lesser extent, on its effects. Nevertheless, the time and length scales at which this behavior occurs remains a matter of debate. While it is commonly agreed upon that flows with St ~ 1 display a higher degree of segregation ([3] and references therein), Bec et al. [22]—among others—have pointed out that the size of the voids and clusters is related to the time and length scales at which observations are made. For example, segregation will occur at small scales when $(\tau_p/\tau_\eta) \sim 1$, however, for particles with $\tau_p \gg \tau_\eta$, a characteristic timescale τ^* can be defined such that the concentration inhomogeneities will be observed at its complementary length scale ℓ^*. Moreover, little is known about the clustering timescales, that

is, if we start with a homogeneously distributed set of particles in region with size on the order of the dissipative scales, how long will it take before particles segregate? Throughout this chapter we will inspect the dynamical behavior of a cloud of particles with the goal of shedding light on these particular aspects of the dynamics of particle–turbulence interaction.

The chapter is structured as follows: in Section 6.1 we will give a brief overview of the relevant background of preferential concentration and some of the options available for quantification of clustering. This will be followed by the description of our experimental setup (Section 6.2). Thereafter, we will present the results of our data analysis from statistical (Section 6.3) and dynamical (Section 6.4) perspectives. Concluding remarks will be given in Section 6.5.

6.1   Background

In Chapter 1 it was stated that, according to Maxey [13], a particle field can be seen as a compressible field even when the carrier flow advecting the particles is incompressible. This compressibility manifests itself as the accumulation of droplets in regions of high strain and the ejection of droplets from those of high vorticity, as will be shown below. At this point we will paraphrase this derivation and point to the approximations made. For a more complete derivation, we refer the reader to the original article (on which we base our derivation).

The equation of motion of a droplet undergoing Stokes friction is

$$\tau_p \frac{\mathrm{d}\boldsymbol{v}}{\mathrm{d}t} = \boldsymbol{u}(t) - \boldsymbol{v}, \tag{6.1}$$

where the Stokes time $\tau_p = d_p^2 \rho_p / 18\mu$. We can integrate this equation once to obtain

$$\boldsymbol{v}(t) = \boldsymbol{v}(t=0)\exp(-t/\tau_p) + \frac{1}{\tau_p}\int_0^t \exp\left(\frac{t'-t}{\tau_p}\right)\boldsymbol{u}(t')\mathrm{d}t', \tag{6.2}$$

which can be integrated by parts once,

$$\boldsymbol{v}(t) = \exp(-t/\tau_p)(\boldsymbol{v}(0) - \boldsymbol{u}(0)) + \boldsymbol{u}(t) - \int_0^t \exp\left(\frac{t'-t}{\tau_p}\right)\frac{\mathrm{d}\boldsymbol{u}}{\mathrm{d}t'}\mathrm{d}t', \tag{6.3}$$

and once more,

$$\boldsymbol{v}(t) = \exp(-t/\tau_p)(\boldsymbol{v}(0) - \boldsymbol{u}(0)) + \boldsymbol{u}(t) - \tau_p \frac{\mathrm{d}\boldsymbol{u}}{\mathrm{d}t} \qquad (6.4)$$
$$+ \tau_p \frac{\mathrm{d}\boldsymbol{u}}{\mathrm{d}t}\bigg|_{t=0} \exp(-t/\tau_p) + \int_0^t \exp\left(\frac{t'-t}{\tau_p}\right) \frac{\mathrm{d}^2\boldsymbol{u}}{\mathrm{d}t'^2} \mathrm{d}t',$$

and so on.

For long times $t \gg \tau_p$ and small Stokes relaxation times, we have

$$\boldsymbol{v}(t) \simeq \boldsymbol{u}(t) - \tau_p \frac{\mathrm{d}\boldsymbol{u}}{\mathrm{d}t}. \qquad (6.5)$$

In fact, since the small-scale velocity field varies on time scale τ_η, the approximation depends on the smallness of τ_p/τ_η, i.e. the smallness of the Stokes number.

For $\mathrm{d}\boldsymbol{u}/\mathrm{d}t$ in Eq. (6.5) we have to take the material derivative,

$$\frac{\mathrm{d}\boldsymbol{u}}{\mathrm{d}t} = \frac{\partial\boldsymbol{u}}{\partial t} + (\boldsymbol{u}\cdot\nabla)\boldsymbol{u}, \qquad (6.6)$$

so that finally

$$\boldsymbol{v}(\boldsymbol{x},t) = \boldsymbol{u}(\boldsymbol{x},t) - \tau_p\left(\frac{\partial\boldsymbol{u}}{\partial t} + (\boldsymbol{u}\cdot\nabla)\boldsymbol{u}\right). \qquad (6.7)$$

In incompressible flow the divergence of the velocity field must vanish. The premise of the above derivation was precisely that a particle field may experience compressibility even when the carrier flow is incompressible. We examine this possibility by calculating the divergence of $\boldsymbol{v}(\boldsymbol{x},t)$, after which all but one term of Eq. (6.7) vanish, resulting in

$$\nabla\cdot\boldsymbol{v} = -\tau_p\nabla\cdot(\boldsymbol{u}\cdot\nabla\boldsymbol{u}). \qquad (6.8)$$

Rearranging terms and moving to a tensor notation we come to

$$\nabla\cdot\boldsymbol{v} = \tau_p\frac{\partial u_j}{\partial x_i}\frac{\partial u_i}{\partial x_j}, \qquad (6.9)$$

which is equivalent to Eq. (1.19),

$$\nabla\cdot\boldsymbol{v} = -\frac{\tau_p}{4}\left[\left(\frac{\partial u_i}{\partial x_j} + \frac{\partial u_j}{\partial x_i}\right)^2 - \left(\frac{\partial u_i}{\partial x_j} - \frac{\partial u_i}{\partial x_j}\right)^2\right]. \qquad (6.10)$$

The above derivation is part of an asymptotic analysis, and, as such, may not accurately represent the dissipative scale dynamics. However, it gives an impression of the underlying physics. Eq. (6.10) clearly conveys the notion of preferential concentration by demonstrating that particles will gather in high strain regions and avoid those with high vorticity. Let us now look at relevant experimental and numerical work which has focused on particle–turbulence interaction.

An experimental study by Gibert et al. [19] concluded that heavy particles preferentially probe particular regions of the flow. Tracking polystyrene, glass and stainless steel particles using PTV, they calculated the mixed velocity–acceleration Eulerian structure function $\langle \delta_r \boldsymbol{v} \cdot \delta_r \boldsymbol{a} \rangle$. For true fluid tracers the magnitude of this quantity equals a constant: -2ε [88]. Although constant for each type of particles, the magnitude for each group differed, with the highest value being associated with the heaviest particles. The increase in the value of the structure function could not be explained by the differences in relative velocities and relative accelerations alone. Therefore, the alignment between $\delta_r \boldsymbol{v}$ and $\delta_r \boldsymbol{a}$ must play a role in such increase. The cosine of the angle between these two vectors,

$$\cos \theta = \frac{\delta_r \boldsymbol{v} \cdot \delta_r \boldsymbol{a_p}}{|\delta_r \boldsymbol{v}| \, |\delta_r \boldsymbol{a_p}|}, \qquad (6.11)$$

gives information regarding their alignment. The probability density function (PDF) of $\cos \theta$ for heavy particles shows a clear preference for collinearity, that is, $|\cos \theta| \approx 1$, whereas the PDF of fluid tracers is more homogeneously distributed in the range $-1 < \cos \theta < 1$. The experimental results are compared to two hypothetical linear velocity fields $u_i = M_{ij} x_j$, where M_{ij} is the velocity gradient tensor. In a purely rotational field it can be easily shown that $\delta_r \boldsymbol{v} \cdot \delta_r \boldsymbol{a} = 0$. On the other hand, in a purely straining velocity field, numerical simulations display similar behavior as seen in experiments, i.e. the velocity and acceleration differences show a trend of enhanced collinearity, which increases with the ratio between the first and second eigenvalues $\langle \lambda_2 / \lambda_1 \rangle$. This, indeed, provides evidence that heavy particles preferentially probe strain-dominated regions of the flow as predicted by Eq. (6.10).

Experimental and numerical evidence exists which points to the filtering effect inertia has on the dynamics of a particle, that is, the most extreme fluctuations of velocity and acceleration are suppressed due to the increased response time of heavy particles. Ayyalasomayajula et al. [89] used 2D PTV to determine the probability density function of the acceleration of droplets with

St ≈ 0.1 in wind-tunnel grid turbulence. Their experimental setup included translating cameras, allowing them to track particles for relatively long periods of time. A comparison between the acceleration PDF of heavy particles and fluid tracers revealed a narrowing of the tails in the case of inertial particles. This agrees with the notion that inertia filters out the most extreme events, due to the increased reaction time.

An experiment in a similar setting was performed by Saw et al. [12], however, the approach was focused on the quantification of inhomogeneities in the particle concentration rather than the inertial effects on the dynamics of particles. Resorting to Taylor's hypothesis of frozen turbulence [90], a one-dimensional snapshot of the particle distribution was obtained using phase-Doppler anemometry (PDA). This information allowed them to calculate the pair correlation function, which gave proof of the clustering effect of inertia. PDA is able to measure both the velocity and size of the particle at one point, opening the possibility to calculate statistics conditioned on the particle size, i.e. for a given set of data, only particles with a diameter within a specific range $d_p \pm \Delta d_p$ can be considered.

For all the studied cases—in which the Stokes number and turbulence intensities were varied—the pair correlation shows a monotonic decrease as r increases, until the clustering scale reaches approximately 10η. As r enters the inertial range, clustering weakly decreases, and the dependence on Stokes number diminishes. The results also show a limited influence of the Taylor-based Reynolds number,Re_λ, on particles with $\text{St} \lesssim 1$, and suggest that such a dependence may arise after the Stokes number increases beyond this level.

The size of particle clusters plays an important role in the calculation of the collision kernel, which is commonly used in many multiphase flow models. Sundaram & Collins [91] performed a numerical study on the collision rates of a particle suspension in isotropic turbulence. They varied both flow and particle parameters in order to assess their effects separately. For intermediate St, their findings show two main effects. The first effect is the preferential concentration of particles in regions of high strain, which agrees with Eq. (6.10) and the findings of Gibert et al. [19]. The second effect is the decorrelation of particle pairs, which signifies an increase in the relative velocities between particles. The preferential concentration effect increases the collision rate, while the relative velocity effect can either increase or decrease the number of collisions, depending on the value of St. For small Stokes numbers, the collision frequency increases with Stokes numbers due to the increase in relative velocities and preferential concentration; a maximum is

reached at St = 0.4. At St > 0.4, the collision frequency keeps increasing, nevertheless, this effect is only due to high relative velocities. This trend continues until the filtering effect of inertia decreases the kinetic energy of the particle ($\tau_p \sim T$).

From the above examples, it is clear that inertia has an effect on the distribution of particles in turbulent flows. However, data on clustering dynamics, that is, how fast clusters are created in an initially homogeneous suspension, is not available. This is an interesting question that, unfortunately, has many practical obstacles, both numerically and experimentally. In numerical simulations the concentration of particles is usually very low due to computational costs. This results in a sparse distribution, and translates into an increased clustering time, e.g. the simulations by Bec et al. [18, 85] have an effective volume fraction of 10^{-10}. In experiments, one may introduce sufficient particles in a flow. For example, our particle volume fraction is three orders of magnitude higher than that in the mentioned simulations. However, starting from a reasonably homogeneous distribution cannot be easily achieved, since particles are affected by the flow as soon as they are introduced.

Nevertheless, Balkovsky et al. [92] have proposed a method which theoretically addresses the clustering dynamics of droplets. Generally, preferential concentration is quantified through the location of individual particles in a snapshot of the field. Their distribution is then compared to random processes to assess the magnitude of inhomogeneities. However, in their approach, it is proposed to look at the particles as a compressible concentration field which is advected by the turbulent flow. An increase in the moments of the concentration $\langle n^\alpha(t) \rangle$ indicates clustering. More details about this will be given in Section 6.4, where we will address the data analysis procedure.

Preferential concentration as a result of particle inertia is not the only collision-enhancing effect of inertia in particle-laden flows. Wilkinson & Mehlig [93] suggest the existence of an anomalous behavior characterized by caustics in the particle field, that is, droplets which are close together can have considerably different velocities, resulting in folds as faster particles may overtake slower ones. The appearance of caustics was also observed in a study by Bec et al. [85], where the particle velocity structure function was calculated from a numerical simulation of a large amount of point-particles. In this study, the absolute value of the difference in particle velocities as a function of their separation r remained finite as $r \to 0$. The explanation given for this anomalous behavior was the existence of caustics in the particle distribution.

6.2 Experimental setup

The overall characteristics of the setup described in the Chapter 5 remain unchanged. The single difference was the creation of a light sheet with a thickness of approximately 1 mm ($\approx 13\eta$) to tag a slab within the droplet cloud. In much the same way we obtained the dispersion data (Section 5.2), the experiments consisted of the acquisition of a series of frame sequences. Each sequence was triggered by a laser shot and consisted of 18 frames. For every analyzed case, we collected 3275 sequences. Measurements for cases 3–5 from Table 2.2 are presented in this chapter.

Again, we use a pulsed laser with a wavelength of 355 nm. Each laser pulse initiates the acquisition of a sequence. We image a square region in the center of the chamber with a side length of 32 mm. A slight illumination inhomogeneity arises due to the profile of the laser beam. We see a higher intensity in the central region of the image, however, this is corrected during the data processing.

While analyzing the data for these experiments, we consistently see a delay in the dynamical effects of the flow on the concentrations. This pattern arises from the contribution of the satellite droplets to the signal intensity of the acquired images. This trend affects the first five frames of our data, which are those on which we are able to compensate for the decay of the signal intensity. An argument can be made that our results are really showing the decay of the phosphorescent signal, however, this is corrected by the normalization of our intensity with the average intensity of the frame.

As mentioned before, the phosphorescent signal of the droplets depends on their volume, meaning that a satellite droplet with one-third the diameter of a primary droplet (see Section 3) will emit 27 times less light. This means that the signal from smaller droplets will decrease below the noise level much faster than the signal coming from primary droplets.

6.3 Statistical quantification of clustering

6.3.1 Deviation from complete randomness

A survey of relevant literature demonstrates that preferential concentration is commonly quantified through statistical analysis. One such example is the previously mentioned study by Saw et al. [12], where the one-dimensional

pair correlation function,

$$\chi(r) = \frac{\widetilde{Q}(r)/\delta r}{Q/L} - 1, \tag{6.12}$$

was calculated using PDA. Q is the total number of pairs detected, while $\widetilde{Q}$ is the number of pairs with separation $r \pm \delta r$; L is the total length probed, calculated from the average mean velocity and the time duration of the measurement. In essence, this quantity represents a histogram of the distance between particles. Similar information can be obtained from the correlation function

$$C(\boldsymbol{r}) = \frac{\langle (I(x+r_x, y+r_y) - \langle I \rangle)(I(r_x, r_y) - \langle I \rangle) \rangle}{\langle I^2 \rangle - \langle I \rangle^2}, \tag{6.13}$$

where $I(x, y)$ is the intensity of the pixel located at (x, y). However, this is not a count of pairs, but of the probability of finding clusters of bright pixels. A homogeneously distributed concentration would produce a delta pulse as its correlation will be greater than zero only at $r = 0$, whereas clusters produce a high value in the small scales with long tails due to the growth of voids. We perform this correlation over 16 pixels, which translates to 13η.

The radial correlation function $C(r)$ was obtained by the azimuthal average of $C(\boldsymbol{r})$. We notice that in 2D the definition Eq. (6.12) would require an
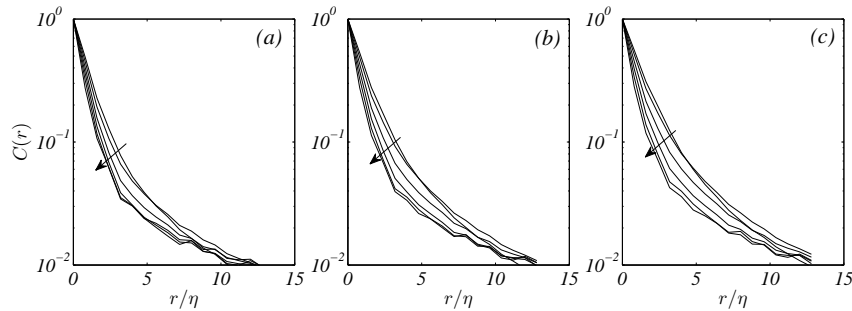
Figure 6.1: *Radial correlation functions of $I(\boldsymbol{x}, t)/\langle I(\boldsymbol{x}, t = 0) \rangle_c$, where $\langle \cdot \rangle_c$ denotes the cycle average and $\langle I(\boldsymbol{x}, t = 0) \rangle_c$ provides a correction for the slight illumination inhomogeneity of the sheet. (a)–(c) represent cases 3–5. The arrow represents time, where the delay goes from $t/\tau_\eta = 0.8$ to 3.4. At increasing delay times the tails of the correlation grow, representing the increasing size of clusters.*

azimuthal integration. The result, shown in Figure 6.1 can be compared to the correlation functions shown in [12]. Differences between our data and that of [12] are due to normalization, since $\chi(r)$ is normalized by the expected number of pairs, while we normalize with $C(r = 0)$. As time progresses, the correlation reaches out to larger separations,signifying the growth of clusters. In the smallest scales, we see a decrease in the correlation, signifying compression of the cluster. We see a very modest difference among different cases, where the correlation slightly increases with Stokes, whereas a strong dependence is seen by Saw et al. [12]. This could represent a larger size of the clusters at larger inertia, however, the difference is not enough to draw conclusions.

Randomly dispersed points usually follow a Poisson distribution. This is also true for the position of fluid tracers. Conversely, heavy particles segregate, preferentially concentrating in particular regions of the flow. This creates a deviation from a random process, which can give us clues regarding the relationship between the structure of the flow and the position statistics of inertial particles. A Poisson distribution is a discrete probability distribution which counts the occurrences of an event k. The special characteristic of such distribution is the fact that the mean and variance are equal. The probability is given by

$$P(k) = \frac{\lambda^k e^{-\lambda}}{k!}.$$ (6.14)

Monchaux et al. [94] quantified the inhomogeneities in the particle distribution by means of a Voronoï tesselation. To do this, they imaged droplets suspended in wind-tunnel grid turbulence, and compared the PDF of the Voronoï cell area to the theoretical expectation from a random Poisson process. Their results show a wider distribution than that expected from homogeneously distributed particles, suggesting the presence of voids and clusters. These findings were later confirmed in homogeneous isotropic turbulence using the Lagrangian Exploration Module [42] by Fiabane et al. [95]. In this study, the authors compare the cell area distribution of both neutrally buoyant and heavy particles. Due to their finite size, the neutrally buoyant particles have St > 0, however, the histogram of cell area does not show a significant deviation from that of a random process. On the other hand, the tails of the PDF for heavy particles show a considerable increase, indicating the existence of voids and clusters.

In many instances, such as the measurement of signal intensity or a concentration, the phenomena of interest are not discrete events, but continuous

functions. For such processes the probability can be approximated using a Gamma distribution. For the particular case of concentration measurements, a random process can be described by [96]

$$P(\mathcal{X}) = \frac{n^n}{\Gamma(n)} \mathcal{X}^{n-1} e^{-n\mathcal{X}}, \tag{6.15}$$

where $\mathcal{X} = I/\langle I \rangle$ and $\Gamma(n)$ is the Gamma function, and n is adjusted to adapt the fit.

In our experiment we take a slightly different approach. Instead of locating the particles within an image—as must be done in a Voronoï tesselation—we split the image into small windows of size δ and measure the intensity within them. This, in principle, should yield equivalent information. We calculate the histogram of the intensity $I_\delta(x,t)/\langle I_\delta(x,t) \rangle_c$ as a function of time. Due to the decaying intensity, we normalize using the time-dependent local average. It can be seen in Figure 6.2 that the measured histogram deviates from the random process, which is approximated in this case by a Gamma distribution. Our histograms show $t/\tau_\eta = 0.8$ to 4.4. The first few images were omitted due to the effects of the secondary droplets, which generate ambiguous results given their tracer-like behavior. We do not expect, however, to have a homogeneous distribution at the time of tagging, since the droplets have been affected by the turbulent flow as soon as they were created
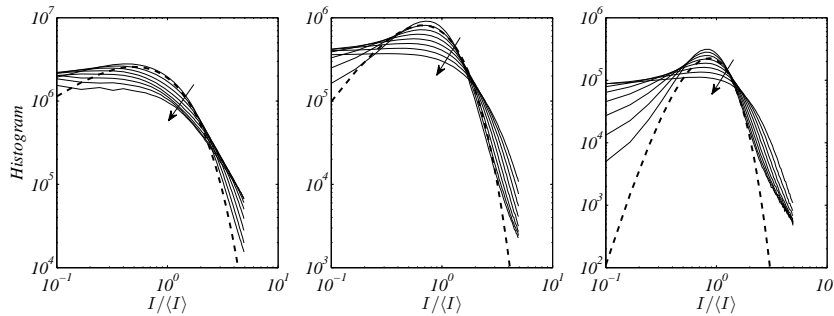
Figure 6.2: *Histograms of $I_\delta(x,t)/\langle I_\delta(x,t) \rangle_c$, where $\langle \cdot \rangle_c$ denotes the cycle average, $\delta/\eta = 3.2, 6.4$, and 12.8, and where the delay time t varies from to $t/\tau_\eta = 0.8$ to 4.4, with the arrow representing the direction of time. The dashed line is a reference obtained from the Gamma distribution with different parameters for each window size (see text). The enhanced probability of voids as time progresses points to clustering of the droplet distribution function.*

The Gamma distribution has a single adjustable parameter, which only

affects its shape. In our case we choose this parameter only as a reference, and not as a fit, since our data cannot be properly fitted given the large deviations from a random process. The values of n for the data seen in Figure 6.2 are $n = 2, 3$, and 7 for $\delta/\eta = 3.2, 6.4$, and 12.8, respectively. The Gamma distribution is a probability density, while we show our data as a histogram. This requires an appropriate scaling factor, which we picked by inspection.

6.3.2 Fractal dimensions

The dimensionality of simple shapes such as lines or blocks can be easily determined. It is obvious, for example, that a plane occupies two dimensions. The dimensionality of fractal objects, however, does not follow such simple rules. A homogeneously distributed cloud of points occupies all of its dimensions, but deviations from homogeneity may translate into reduced dimensionality. Droplets and bubbles in a turbulent flow are not homogeneously dispersed, creating voids and clusters as a result of their interaction with turbulence. Several studies have looked at the fractal dimension of dispersed phases in turbulent flows (see e.g. [22, 97]), finding that indeed the dimensionality of the dispersed phase is reduced due to inertia.

Calzavarini et al. [97], studied the dimensionality of light and heavy particles suspended in turbulence. As their numerical simulation provided dynamical information, they computed the Lyapunov exponents λ_i, which quantify the growth of perturbations along trajectories. Using this information the Kaplan–Yorke dimension can be computed as

$$D_{KY} = K + \sum_{i=1}^{K} \frac{\lambda_i}{|\lambda_{K+1}|}, \tag{6.16}$$

where K is defined such that $\sum_{i=1}^{K} \lambda_i \geq 0$. The Kaplan–Yorke dimension also estimates the fractal dimension of the particle distribution in space. It appeared that neutrally buoyant particles with St $\lesssim 1.5$, have $D_{KY} = 3$, which implies that they fill space homogeneously. This is in agreement with the results of [95]. On the other hand, both heavy and light particles present a dimensionality lower than three for this Stokes number region, with minima at St ≈ 0.5 and St ≈ 0.9, respectively.

Fractal dimensions gauge the self-similar distribution of droplet clusters. We compute them as generalized dimensions, which are related to the scaling

of the partition sum [98]

$$L(\delta; q) = \sum_i P_i^q \sim \delta^{(q-1)D(q)}, \tag{6.17}$$

where δ is the linear size of the square over which the mass P_i is summed, and in our analysis we approximate the mass as

$$P_i = \int_{B_{i,\delta}} \frac{I(x,t)}{\langle I(x, t=0)\rangle_c} \mathrm{d}x, \tag{6.18}$$

with $B_{i,\delta}$ the square with index i and linear size δ. The mass P_i is proportional to the number of droplets in a square of size δ. For a completely homogeneous distribution, $D(q) = 2$ for all values of q. The fractal dimension of droplet distributions in a 3D simulated velocity field was reported as $D(2) \simeq 2.4$, using the correlation dimension, which should be comparable to $D(q = 2)$ [97]. We are measuring the distribution of droplets in a tagged *sheet*. Using the intersection rule for a fractal dimension [99], the corresponding dimension in the sheet would be $D(2) - 1 = 1.4$.
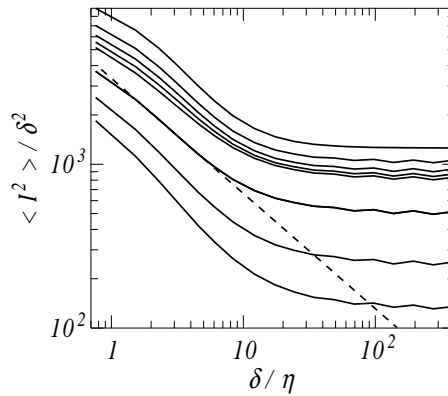
Figure 6.3: *Scaling of box-integrated intensity, $\langle I_\delta^2 \rangle / \delta^2$. In case of a homogeneously filled plane, $\langle I_\delta^2 \rangle / \delta^2$ would be independent of δ. The dashed line fitting the data at $t/\tau_\eta = 2.1$ shows $\langle I_\delta^2 \rangle \propto \delta^{1.3}$, which implies a fractal dimension of the three–dimensional droplet distribution $D(2) \approx 2.3$. However, the fractal scaling does not cover all scales, so that the droplet distribution is not self-similar. At the Stokes numbers used, clusters and voids cover distances up until $\approx 10\eta$.*

Instead of the partition sum $L(\delta; q = 2)$, we compute the deviation from plane filling $\langle I_\delta^2 \rangle / \delta^2$. For small distances $\delta/\eta \lesssim 10$, we find scaling with

a fractal dimension $D(2) \approx 1.3$. In three dimensions this would amount to $D(2) = 2.3$, which is in reasonable agreement with the dimensions found by Bec et al. [22] and Calzavarini et al. [97]. The fractal scaling does not cover all scales, which is in line with available literature (see e.g. [22]).

6.4 Dynamical quantification of clustering

As mentioned above, an interesting dynamical quantity of preferential concentration has been described by Balkovsky et al. [92]. Let us briefly paraphrase their argument. The key point is that we view the particle field as a continuous droplet concentration field $n(\boldsymbol{x}, t)$, which actually matches our experiment, where $n(\boldsymbol{x}, t)$ is proportional to the measured intensity.

This concentration field satisfies the continuity equation

$$\frac{\partial n}{\partial t} + \nabla(\boldsymbol{v} n) = 0. \tag{6.19}$$

In this equation, $\nabla \cdot \boldsymbol{v}$ is a source of random fluctuations, which, in the approximation of Eq. (6.10) is completely determined by the fluctuations

$$\nabla \cdot \boldsymbol{v} = \tau_p \nabla \cdot ((\boldsymbol{u} \cdot \nabla)\boldsymbol{u}) \tag{6.20}$$

of the turbulent velocity field $\boldsymbol{u}(\boldsymbol{x}, t)$. In the Lagrangian frame, Eq. (6.19) becomes an ordinary differential equation

$$\frac{\mathrm{d}n}{\mathrm{d}t} = -n(\nabla \cdot \boldsymbol{v}), \tag{6.21}$$

with the trivial solution

$$\ln\left(\frac{n(t)}{n(0)}\right) = -\int_0^t (\nabla \cdot \boldsymbol{v})\mathrm{d}t'. \tag{6.22}$$

Again, the fluctuations of the quantity $X(t) = \ln(n(t)/n(0))$ are induced by the fluctuations of the turbulent velocity field (Eq. (6.10)), but now taken along a Lagrangian trajectory. For long times, fluctuations are time-averaged over many correlation times, and the law of large numbers applies with the PDF of X assuming a Gaussian shape

$$P(x) = \frac{1}{(\pi \sigma t)^{1/2}} \exp\left(\frac{-x^2}{\sigma t}\right), \tag{6.23}$$

or, more general, $P(X) \sim \exp(-ts(X/t))$, with s a convex function. Eq. (6.23) expresses that the magnitude of the fluctuations decreases as $\langle X^2 \rangle \sim t^{-1}$ when time progresses. The consequence is that the moments

$$\langle n^\alpha \rangle \propto \int \exp\left[(\alpha - 1)X - ts(X/t)\right] \mathrm{d}X,$$

where the factor $\exp(-X)$ arises from the translation back to the Eulerian frame. For large t, only the minimum of the integrand contributes, so that

$$\langle n^\alpha \rangle \propto \exp\left[(\alpha - 1)X_\alpha - ts(X_\alpha/t)\right],$$

with X_α given by $s'(X_\alpha/t) = \alpha - 1$, so that $X_\alpha = tf(\alpha)$, and

$$\langle n^\alpha(t) \rangle \propto \mathrm{e}^{\gamma(\alpha)t}, \tag{6.24}$$

with $\gamma(\alpha) = (\alpha - 1)f(\alpha) - S(f(\alpha))$. In our experiment the time t extends to only a few Kolmogorov times, but we average $\langle n^\alpha(t) \rangle$ over an area spanning many Kolmogorov lengths, and the question is whether an exponential growth of moments can be observed in the experiment.

There are three crucial aspects on the applicability of this method to our data. First, the analysis relies on the assumption that the concentration is a conserved quantity, while our experimental data suffers from an inherent 'loss' of droplets due to the diminishing phosphorescent signal. Second, it is assumed by the authors of the study that the initial concentration $n(0)$ is homogeneous, however, this may not necessarily be the case at the time of tagging in our experiment, since droplets have undergone the effects of turbulence from the time they entered the chamber. Lastly, the analysis calls for the normalization of the concentration $n(t)$ by the initial concentration $n(0)$ in a Lagrangian sense, that is, when we take the local concentration of a small tile within the image, we must follow that tile as it is advected by the flow. Currently, this is not possible as we do not have the instantaneous particle velocity field.

The loss of particles is partially resolved by the exponential increase in the exposure of the camera, which ameliorates the intensity decay. In addition, we normalize the instantaneous local concentration using the instantaneous ensemble-averaged concentration.

A sample of a data image is plotted in Figure 6.4 together with the values for $\langle I_\delta^\alpha(x,t) \rangle_c / \langle I_\delta(x,t) \rangle_c^\alpha$. We see that the moments of the intensity increase

exponentially, as indicated by Eq. (6.24). Also we see that the exponent $\gamma(\alpha)$ saturates, fulfilling the convexity requirement. The increase in the moments is delayed by approximately by $2\tau_\eta$, after which we see the expected exponential increase.
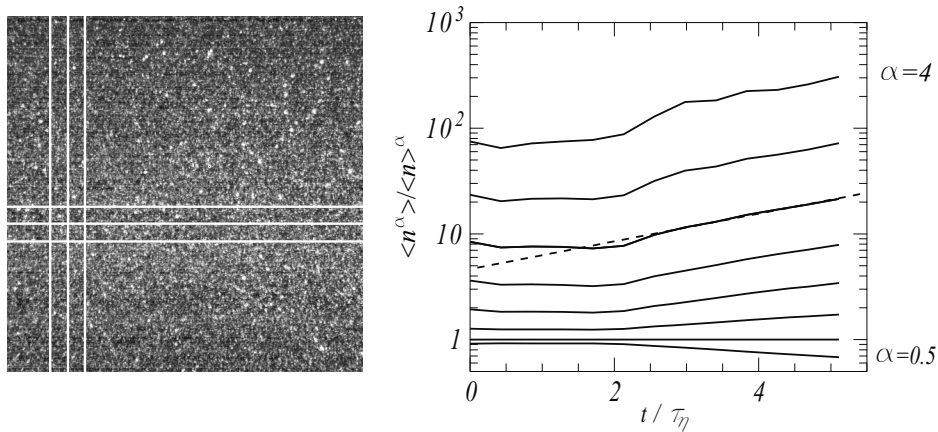
Figure 6.4: *Moments of local concentration fluctuations, $\langle I_\delta^m(x,t)\rangle_c / \langle I_\delta(x,t)\rangle_c^m$ as a function of delay time t and $\delta/\eta = 6.4$. The intersection of the solid white lines shows the windows over which the intensity was integrated. Dashed line: $\langle I_\delta^m(x,t)\rangle_c / \langle I_\delta(x,t)\rangle_c^m \sim \exp(\gamma t/\tau_\eta)$, with $\gamma = 0.3$. After $t/\tau_\eta \approx 2$, the moments increase exponentially due to the Langrangian average of the fluctuations of the divergence of the particle velocity field.*

As we mentioned in Section 6.2, the dynamical behavior displayed by our data in the first few frames is affected by the contribution to the intensity of the satellite droplets. This can be observed in the time evolution of the moments, where the first five points display an almost constant value. Once the signal from the satellite droplets is no longer appreciable, the behavior of the heavy droplets becomes apparent.

The length scale at which preferential concentration can be seen is a matter of debate. Measurements by Saw et al. [12] suggest clustering is seen at scales $\sim \eta$, where the effect of clustering on the pair correlation function is very weak at scales larger than 10η. On the other hand, it has been proposed by Bec et al. [22] that a clustering timescale τ^* can be found such that the Stokes number becomes unity, thus resulting in preferential concentration at its corresponding length scale ℓ^*. To assess this, we calculate the

moments of the local concentration averaged over three different box sizes $\delta = 3.2\eta$, 6.4η, and 12.8η.

In our experiments we have a relatively narrow distribution of droplets, meaning the Stokes number is well defined. Therefore,we expect to see clustering effects at scales corresponding to τ_η, i.e. the Kolmogorov length η. At larger length scales δ, we would see clustering at longer time scales. Figure 6.5 shows the behavior of the moments for case 3, which show an exponential increase of the moments at length scales $\delta = 3.2\eta$, 6.4η, while the largest scale $\delta = 12.8\eta$ clearly loses the exponential behavior. This behavior can also be seen in cases 4 and 5 (not shown).
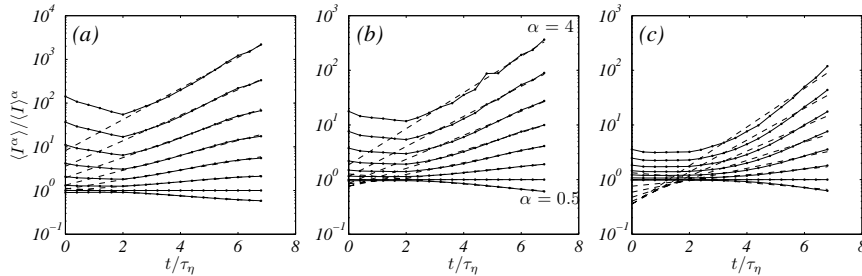
Figure 6.5: *Moments of the local intensity for case 3 for three interrogation size lengths $\delta/\eta = 3.2, 6.4$, and 12.8 for (a)–(c), respectively. We see that the exponential behavior is delayed for the largest interrogation size.*

A similar picture can be obtained from the fractal dimension of the droplet distribution. As seen in Figure 6.3, the reduced dimensionality reaches approximately 10η, being in agreement with the findings of [12].

6.4.1 Stokes number dependence

It has been previously established that inertia can be quantified through the ratio of particle and flow timescales, namely the Stokes number. We have also established that inertia has a filtering effect on the velocity of the droplets. Naturally, this will have an impact on the dynamics of the particles. To assess the extent of this effect we have performed experiments with three different Stokes numbers, cases 3–5.

From Eq. (6.24), we see that the function $\gamma(\alpha)$ gives an indication of the speed at which the moments grow, that is, a higher value translates into a faster increase of the moments. We see in Figure 6.6, that a considerable

difference is seen between the exponents of the three different inertia cases, with the heaviest droplets consistently being slower.
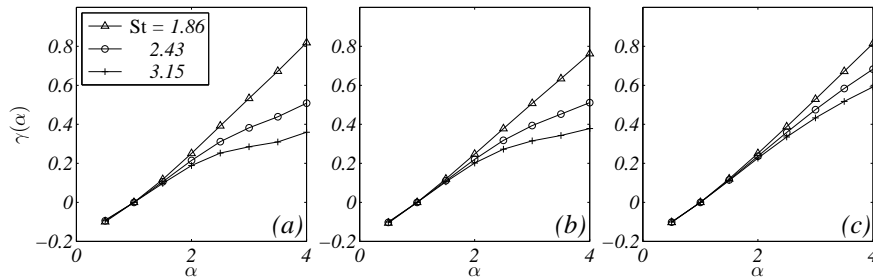
Figure 6.6: *Dependence of the function $\gamma(\alpha)$ on Stokes number. (a)–(c) for interrogation window size $\delta/\tau_\eta = 3.2, 6.4$, and 12.8, respectively.*

6.5 Conclusions

In this chapter, we have addressed the problem of preferential concentration of inertial particles by tagging a thin slab within a turbulent cloud. Once the sheet is tagged, we measure the inhomogeneity of particle concentration from a statistical and a dynamical perspective. Not much is known about methods that can probe the dynamics of clustering. Our results can be compared to results from the literature, which were from numerical simulations most of the time.

Throughout the chapter we have used three different approaches for the quantification of particle segregation, one of which consists of the measurement of the deviation of a particle distribution from a random process. In our case, we look at the deviation from a random Poisson process of the intensity histogram of small tiles within the imaged distribution. This shows a clear deviation from the expected distribution of a random process. Also, it shows that this deviation grows in time, pointing to the further clustering of the droplets.

We have also measured the dimensionality of the arrangement the particles take when suspended in a turbulent flow. The correlation dimension $D(2)$ of the intensity was measured by looking at the dependence of the box-integrated intensity on the size of the box. The particle distribution does not show self-

similarity, however, at the small scales a reduced dimensionality is clear. The value of $D(2) = 1.3$ agrees with numerical simulations by [22, 97].

Lastly, a dynamical perspective to the clustering of droplets was obtained by calculating the moments of the particle concentration as suggested by Balkovsky et al. [92]. We see that the moments increase exponentially after approximately two Kolmogorov times, and $\gamma(\alpha)$ meets the constraints placed by the theoretical analysis.

In both statistical and dynamical analyses, we see a clear dependence of the clustering manifestation on the scales at which the data is inspected. The fractal dimension shows a lower dimensionality at scales $\lesssim 10\eta$. Analogously, we also see a change in the clustering behavior as given by the moments of the intensity $\langle I_\delta^\alpha(x,t) \rangle_c / \langle I_\delta(x,t) \rangle_c^\alpha$. The moments lose their exponential behavior and appear to shift to a power law.

CHAPTER 7

CONCLUDING REMARKS

7.1 Conclusions

Throughout this thesis, we have given an in-depth description of a novel technique that makes the tagging of selected regions of clouds possible. We have tested this technique in a man-made cloud chamber which holds some of the characteristics possessed by natural clouds. The chamber is able to generate very intense turbulence ($Re_\lambda \approx 500$) with a negligible mean flow, and substantial isotropy and homogeneity. Phosphorescent droplets were generated using spinning disk aerosol generation. We used interferometric particle imaging to measure droplet diameters, and developed an algorithm capable of automatically processing IPI data. The algorithm is capable of locating particle images and generating a probability density function of the particle diameter. It is also able to partially circumvent the sensitivity of IPI to particle overlaps. Five different cases were inspected with droplet diameters ranging from 11 μm to 24 μm, the droplets having a narrow distribution with a standard deviation of approximately 3 μm. This allows us to have a well defined Stokes number in our experiments.

We have given a proof of principle on the use of phosphorescent droplets as a diagnostic tool for particle-laden flows. The phosphorescent solution used is water-based and uses Europium (Eu^{3+}) as its phosphor; the ligands used are TTA and TOPO. The solution has a phosphorescence lifetime $\tau_{ph} \approx$

123

$600\,\mu$s, which is comparable to the Kolmogorov timescale τ_η of our flow. The solution can also be used in continuous phases, however, it must be diluted to increase penetration of the laser beam into the fluid.

The longstanding problem of turbulent dispersion was revisited with a new perspective given by the newly developed phosphorescent tagging technique. We tag thin, pencil-like clouds of phosphorescent droplets and look at their widening at timescales comparable to τ_η. Two notable results came from these experiments: droplets disperse much faster (up to 50%) than the theoretical prediction for fluid tracers, and the spreading velocity of the cloud v_s has an optimum at St ≈ 2. Data from an analogous experiment with true tracers (nitric oxide in air) produces a spreading velocity which is slightly higher ($< 10\%$ than the *rms* velocity. From the pair dispersion study by Bec et al. [18], we know that relative dispersion may be faster in heavy droplets than in tracers. However, our experiment does not exclusively measure relative dispersion. The cause behind these results remains unclear, however, we speculate that such rapid dispersion may be a result of the higher velocity differences seen in heavy particles compared to fluid tracers. These velocity differences may translate into the faster separation of two particles.

Numerical simulations give no indication of such a rapid dispersion. However, the simulations do not exactly represent the experiment, since the dispersion, as measured by the velocity autocorrelation, does not account for larger velocity differences between particles. We believe a simulation with a higher concentration, where large groups (clouds) of particles can be tagged may help us understand the physics of puff dispersion.

A slight modification to our experimental setup allowed us to look at the preferential concentration phenomenon. By tagging a thin sheet of droplets within the turbulent cloud, we were able to quantify the segregation from both statistical and dynamical perspectives. The histogram of the local signal intensity (concentration) presents wider tails than expected from a random process. This is a signature of preferential concentration as voids and clusters translate into a higher probability of finding either very low or very high particle concentrations.

Another statistical tool that brings preferential concentration to light is the dimensionality of a dispersion of particles. Randomly dispersed particles occupy all space, while fractal structures display reduced dimensionality. The experimental data exhibits a correlation dimension $D(2) = 1.3$, which tells us that indeed a fractal structure is seen in the spatial concentration of droplets. This value, when translated to three dimensions, agrees reasonably well with

existing numerical data [22, 97].

As we have repeatedly mentioned throughout this thesis, the primary interest in the development of the phosphorescent tagging technique lies in the elucidation of the dynamics of preferential concentration. To this aim, we followed the approach proposed by Balkovsky et al. [92] to measure the growth of the moments of the intensity (concentration). Despite some differences between the theoretical instance and the experiment the moments grow exponentially, agreeing with the theoretical prediction. The exponent $\gamma(\alpha)$, which determines the growth in time of the moments of the concentration $\langle n(\boldsymbol{x}, t) \rangle$, satisfies the constraints set by the theoretical analysis, i.e. it is a convex function, $\gamma(1) = 0$, and $\gamma(\alpha < 1) < 0$.

7.2   Outlook

As we have seen throughout this work, particle-laden flows are commonplace in both nature and industry. Some of these instances are the dispersion of pollen and pollutants by wind and silt transport in rivers, while on an industrial setting, fuel injection and spray drying are intimately affected by aerosol physics. Because of such abundance and the increased interest in this type of flows, we propose a few experiments that may be created or adapted which can benefit from our tagging technique.

7.2.1   Collision detection

Even though some fundamental aspects of particle-laden flows remain unanswered, a substantial body of literature has been collected regarding the phenomenon of preferential concentration. However, the same cannot be said about the effect of preferential concentration on the collision kernel. The fact that particles agglomerate in certain areas of the flow increases the probability of collisions, yet a postulate by Woittiez [28] argues that droplets that are close to each other and have similar sizes will consequently have similar velocities, reducing the probability of collision. On the other hand, Wilkinson & Mehlig [93] point to the existence of caustics in the particle velocity fields, which precisely opposes the notion of Woittiez. However, it is argued that even a slight polydispersity can have a considerable effect on the collision kernel.

To address the question of droplet collisions we propose an experiment where two different liquids are used to make droplets, and only when two droplets of different type have collided will the droplet obtain phosphorescent properties. The possibility of using chemiluminescence is appealing, however, unless the luminescence is very short-lived, light-emitting fluid on the walls of the facility could deteriorate the quality of the data. We believe that a slight modification to our technique, where one type of droplets only contains Europium and water, and a second type contains ligands and water, may help in the detection and quantification of crucial collision statistics.

7.2.2   Gravity effects

The trivial situation of a droplet falling through a quiescent fluid becomes a complex issue when this circumstance arises in turbulent flow. Several studies (e.g. [29, 30]) suggest that the turbulent terminal velocity of a droplet is larger than that of a free-falling droplet as a result of 'preferential sweeping'—a propensity of droplets to sweep through regions of the flow that have a downward velocity. However, Pasquero et al. [100] obtained results opposing this view. In their simulations, two distinct terminal velocities appear for identical droplets. One of the populations has a settling velocity which is larger than the terminal velocity in still fluid, while the second one has a virtually zero terminal velocity. The second group of particles is product of droplets having closed trajectories, that is, the trajectory ends in its own tail. According to the authors of this study, this is possible due to the change of sign of the curvature along the trajectory.

A slight modification to our dispersion experiments (Chapter 5), where bigger droplets with settling velocities on the order of the turbulent velocity fluctuations are generated, may shed light on both the effect of gravity on lateral dispersion and the effective terminal velocity of a settling droplet.

7.2.3   Cluster break-up

When inspecting the data obtained from the experiments described in Chapter 6, we notice that, at times, clusters were present within the tagged slab and, as time progressed, these clusters would become elongated and disperse. As has been discussed above, in our experiments, tagged droplets have undergone the effects of turbulence before being tagged, resulting in clusters being present in the tagging event. We believe our technique is especially suited to investigate

this phenomenon, given these droplet bunches can be located using particle tracking algorithms, and the dispersion in a Lagrangian sense can be analyzed.

This cluster break up mechanism appears to counteract preferential concentration, opening yet another interesting question in the realm of cloud physics.

APPENDIX A

APPENDIX

A.1 Dissipation in isotropic turbulence

A fourth-order, isotropic tensor can be written as

$$c_{ijkl} = \alpha\delta_{ij}\delta{kl} + \beta\delta_{ik}\delta_{jl} + \gamma\delta_{il}\delta_{jk} \tag{A.1}$$

where α, β, and γ are scalars. For isotropic turbulence we have the fourth-order, isotropic tensor

$$\left\langle \frac{\partial u_i}{\partial x_j}\frac{\partial u_k}{\partial x_l} \right\rangle = \alpha\delta_{ij}\delta_{kl} + \beta\delta_{ik}\delta_{jl} + \gamma\delta_{il}\delta_{jk} \tag{A.2}$$

From continuity ($\nabla \cdot \boldsymbol{u} = 0$) we know $\frac{\partial u_i}{\partial x_i} = 0$. Setting $i = j$ in (A.2) we have

$$\left\langle \frac{\partial u_i}{\partial x_i}\frac{\partial u_k}{\partial x_l} \right\rangle = \alpha\delta_{ii}\delta_{kl} + \beta\delta_{ik}\delta_{il} + \gamma\delta_{il}\delta_{ik} = 0$$

Now setting $i = l$ and rearranging we get

$$\left(3\alpha + \beta + \gamma\right)\delta_{kl} = 0$$

$$3\alpha + \beta + \gamma = 0 \tag{A.3}$$

The second condition used is homogeneity (no spatial variation of the following average)

$$\frac{\partial}{\partial x_j} \left\langle u_i \frac{\partial u_j}{\partial x_l} \right\rangle$$

=0 Using the product rule

$$\left\langle \frac{\partial u_i}{\partial x_j} \frac{\partial u_j}{\partial x_l} + u_i \frac{\partial^2 u_j}{\partial x_j^2} \right\rangle$$

Again, due to continuity the second term goes to zero ($\frac{\partial u_j}{\partial x_j} = 0$) to get

$$\left\langle \frac{\partial u_i}{\partial x_j} \frac{\partial u_j}{\partial x_l} \right\rangle = \alpha \delta_{ij}\delta_{jl} + \beta \delta_{ij}\delta_{jl} + \gamma \delta_{il}\delta_{jj} = 0$$

Setting $j = l$ we get

$$\left(\alpha + \beta + 3\gamma \right) \delta_{il} = 0$$
$$\alpha + \beta + 3\gamma = 0 \tag{A.4}$$

From (A.3) and (A.4) we get $\alpha = \gamma = -\beta/4$. From isotropy we have

$$\left\langle \frac{\partial u_i}{\partial x_j} \frac{\partial u_k}{\partial x_l} \right\rangle = \beta \left(-\frac{1}{4}\delta_{ij}\delta_{kl} + \delta_{ik}\delta_{jl} - \frac{1}{4}\delta_{il}\delta_{jk} \right) \tag{A.5}$$

where

$$\left\langle \left(\frac{\partial u_1}{\partial u_1} \right)^2 \right\rangle = \frac{\beta}{2} \quad \text{and} \quad \left\langle \left(\frac{\partial u_1}{\partial u_2} \right)^2 \right\rangle = \beta \tag{A.6}$$

Now, we know the dissipation is defined as

$$\epsilon = \nu \left\langle \frac{\partial u_i}{\partial x_j} \frac{u_i}{x_j} \right\rangle \tag{A.7}$$

From (A.1) and (A.5), (A.7) can be written as

$$\epsilon = \nu\beta \left(-\frac{1}{4}\delta_{ij}\delta_{ij} + \delta_{ii}\delta_{jj} - \frac{1}{4}\delta_{ij}\delta_{ji} \right)$$

Setting $i = j$ we get

$$\epsilon = \nu\beta\left(-3/4 + 9 - 3/4\right) = \nu\beta\frac{15}{2}$$

which by (A.6) becomes

$$\varepsilon = 15\nu\left\langle\left(\frac{\partial u_1}{\partial x_1}\right)^2\right\rangle \tag{A.8}$$

In conclusion, the well-known results Eq.(A.8) follows from homogeneity and isotropy.

A.2   Velocity and position of an ejected droplet

Eq. 3.13 can be written in the form

$$\frac{dV_d}{dt} = -\alpha V_d\left(1 + \beta V_d^{2/3}\right) \tag{A.9}$$

where

$$\alpha = \frac{9}{2}\frac{\rho_a\nu_a}{\rho_p r_p^2} \qquad \text{and} \qquad \beta = \frac{1}{6}\left(\frac{2r_p}{\nu_a}\right)^{2/3}$$

We see that Eq. (A.9) can be solved analytically. We start with the ansatz $V_d = \xi e^{-\alpha t}$ to get

$$-\alpha V_d + e^{-\alpha t}\frac{d\xi}{dt} = -\alpha V_d - \beta V_d^{5/3}$$

Canceling terms and separating variables we get

$$\frac{d\xi}{\xi^{5/3}} = -\alpha\beta e^{-\frac{2}{3}\alpha t}dt$$

Integrating results in

$$-\frac{3}{2}\xi^{-2/3} = \alpha\beta\frac{3}{2\alpha}e^{-\frac{2}{3}\alpha t} + C_1$$

Rearranging,we get

$$\xi = \frac{1}{\left(-\beta e^{-\frac{2}{3}\alpha t} + C\right)^{3/2}} \qquad \text{or} \qquad V_d = \frac{e^{-\alpha t}}{\left(-\beta e^{-\frac{2}{3}\alpha t} + C_1\right)^{3/2}}$$

The value of the integration constant C_1 can be obtained by evaluating V_d at its initial condition $V_d(t = 0) = V_o = \omega\frac{D}{2}$ to get

$$C_1 = V_o^{-2/3} + \beta.$$

So

$$V_d(t) = \frac{e^{-\alpha t}}{\left(-\beta e^{-\frac{2}{3}\alpha t} + \left(\frac{D}{2}\omega\right)^{-2/3} + \beta\right)^{3/2}} \tag{A.10}$$

Now we can integrate the velocity to get the droplet position as a function of time. Again, we know

$$\frac{dx}{dt} = V_d(t)$$

Making the change of variable $y = e^{-\alpha t}$ $(dy = -\alpha e^{-\alpha t}dt \rightarrow dt = -y^{-1}dy/\alpha)$, from Eq. (A.10) we get

$$V_d(t) = -\frac{1}{\alpha}\frac{1}{\left(-\beta x^{2/3} + C_1\right)^{3/2}}dy \tag{A.11}$$

Making a second change of variable $z = y^{1/3}$ $(dz = y^{-2/3}dy/3 \rightarrow dy = 3z^2 dz)$, we get

$$V_d(t) = -\frac{3}{\alpha}\frac{z^2}{\left(-\beta z^2 + C\right)^{3/2}}dz \tag{A.12}$$

The resulting equation has an integral of the form

$$\int \frac{z^2}{(a - cz^2)^{3/2}}dz = \frac{z}{c(a - cz^2)^{1/2}} - \frac{1}{c^{3/2}}\tan^{-1}\left(\frac{c^{1/2}z}{(a - cz^2)^{1/2}}\right) + C_2$$

So Eq. (A.12) becomes

$$x(z) = -\frac{3}{\alpha}\left[\frac{z}{\beta(C_1 - \beta z^2)^{1/2}} - \frac{1}{\beta^{3/2}}\tan^{-1}\left(\frac{\beta^{1/2}z}{(C_1 - \beta z^2)^{1/2}}\right) + C_2\right]$$

Before we apply the initial condition $x(t = 0)$, we must return to our original variable t. This results in

$$x(t) = -\frac{3}{\alpha}\left[\frac{e^{-\frac{1}{3}\alpha t}}{\beta(C_1 - \beta e^{-\frac{2}{3}\alpha t})^{1/2}} - \frac{1}{\beta^{3/2}}\tan^{-1}\left(\frac{\beta^{1/2}e^{-\frac{1}{3}\alpha t}}{(C_1 - \beta e^{-\frac{2}{3}\alpha t})^{1/2}}\right) + C_2\right] \tag{A.13}$$

After applying the initial condition, the integration constant becomes

$$C_2 = \frac{1}{\beta^{3/2}} \tan^{-1}\left(\frac{\beta^{1/2}}{(C_1 - \beta)^{1/2}}\right) - \frac{1}{\beta(C_1 - \beta)^{1/2}}$$

Resulting in

$$x(t) = -\frac{3}{\alpha}\left[\frac{e^{-\frac{1}{3}\alpha t}}{\beta(C_1 - \beta e^{-\frac{2}{3}\alpha t})^{1/2}} - \frac{1}{\beta^{3/2}}\tan^{-1}\left(\frac{\beta^{1/2}e^{-\frac{1}{3}\alpha t}}{(C_1 - \beta e^{-\frac{2}{3}\alpha t})^{1/2}}\right)\right.$$
$$\left. + \frac{1}{\beta^{3/2}}\tan^{-1}\left(\frac{\beta^{1/2}}{(C_1 - \beta)^{1/2}}\right) - \frac{1}{\beta(C_1 - \beta)^{1/2}}\right] \quad \text{(A.14)}$$

REFERENCES

[1] B. Shraiman and E. Siggia, "Scalar turbulence," *Nature*, **405**, 639–646, (2000).

[2] K. D. Squires and J. K. Eaton, "Preferential concentration of particles by turbulence," *Physics of Fluids A: Fluid Dynamics*, **3**, 1169, (1991).

[3] R. A. Shaw, "Particle-Turbulence Interactions in Atmospheric Clouds," *Annual Review of Fluid Mechanics*, **35**, 183–227, (2003).

[4] S. Balachandar and J. K. Eaton, "Turbulent Dispersed Multiphase Flow," *Annual Review of Fluid Mechanics*, **42**, 111–133, (2010).

[5] F. Toschi and E. Bodenschatz, "Lagrangian Properties of Particles in Turbulence," *Annual Review of Fluid Mechanics*, **41**, 375–404, (2009).

[6] A. N. Kolmogorov, "Dissipation of Energy in the Locally Isotropic Turbulence," *Proceedings from the USSR Academy of Sciences*, **30**, 299–303, (1941).

[7] U. Frisch, *Turbulence: The Legacy of A.N. Kolmogorov*. Cambridge: Cambridge University Press, (1996).

[8] K. Sreenivasan and R. Antonia, "The phenomenology of small-scale turbulence," *Annual review of fluid mechanics*, **29**, 435–472, (1997).

[9] M. R. Maxey and J. J. Riley, "Equation of motion for a small rigid sphere in a nonuniform flow," *Physics of Fluids*, **26**, 883, (1983).

[10] A. Daitche and T. Tél, "Memory Effects are Relevant for Chaotic Advection of Inertial Particles," *Physical Review Letters*, **107**, 244501, (2011).

[11] M. Van Hinsberg, J. ten Thije Boonkkamp, and H. Clercx, "An efficient, second order method for the approximation of the basset history force," *Journal of Computational Physics*, **230**, 1465–1478, (2011).

[12] E. Saw, R. Shaw, S. Ayyalasomayajula, P. Chuang, and A. Gylfason, "Inertial Clustering of Particles in High-Reynolds-Number Turbulence," *Physical Review Letters*, **100**, 1–4, (2008).

[13] M. Maxey, "The gravitational settling of aerosol particles in homogeneous turbulence and random flow fields," *Journal of Fluid Mechanics*, **174**, 441–465, (1987).

[14] L. P. Wang and D. E. Stock, "On the dispersion of heavy particles by turbulent motion," *Journal of the Atmospheric Sciences*, **50**, 1897–1913, (1993).

[15] G. Gouesbet, A. Berlemont, and A. Picart, "Dispersion of discrete particles by continuous turbulent motions. Extensive discussion of the Tchen's theory, using a two-parameter family of Lagrangian correlation functions," *Physics of Fluids*, **27**, 827–837, (1984).

[16] G. Falkovich, A. Fouxon, and M. Stepanov, "Acceleration of rain initiation by cloud turbulence," *Nature*, **419**, 151–154, (2002).

[17] L. M. Pismen and A. Nir, "On the motion of suspended particles in stationary homogeneous turbulence.," *Journal of Fluid Mechanics*, **84**, 193–206, (1978).

[18] J. Bec, L. Biferale, A. S. Lanotte, A. Scagliarini, and F. Toschi, "Turbulent pair dispersion of inertial particles," *Journal of Fluid Mechanics*, **645**, 497–528, (2010).

[19] K. Gibert, H. Xu, and E. Bodenschatz, "Where do small, weakly inertial particles go in a turbulent flow?," *Journal of Fluid Mechanics*, **698**, 160–167, (2012).

[20] S. Ayyalasomayajula, Z. Warhaft, and L. R. Collins, "Modeling inertial particle acceleration statistics in isotropic turbulence," *Physics of Fluids*, **20**, 095104, (2008).

[21] E. Calzavarini, M. Cencini, D. Lohse, and F. Toschi, "Quantifying Turbulence-Induced Segregation of Inertial Particles," *Physical Review Letters*, **101**, 4–7, (2008).

[22] J. Bec, L. Biferale, M. Cencini, A. Lanotte, S. Musacchio, and F. Toschi, "Heavy particle concentration in turbulence at dissipative and inertial scales," *Physical review letters*, **98**, 084502, (2007).

[23] G. I. Taylor, "Diffusion by continuous movements," *Proceedings of the London Mathematical Society*, **151**, 196–212, (1921).

[24] L. Richardson, "Atmospheric Diffusion Shown on a Distance-Neighbour Graph," *Proceedings of the Royal Society A: Mathematical, Physical and Engineering Sciences*, **110**, 709–737, (1926).

[25] G. K. Batchelor, "The application of the similarity theory of turbulence to atmospheric diffusion," *Quarterly Journal of the Royal Meteorological Society*, **76**, 133–146, (1950).

[26] M. Bourgoin, N. T. Ouellette, H. Xu, J. Berg, and E. Bodenschatz, "The role of pair dispersion in turbulent flow.," *Science (New York, N.Y.)*, **311**, 835–838, (2006).

[27] J. Bec, L. Biferale, G. Boffetta, M. Cencini, S. Musacchio, and F. Toschi, "Lyapunov exponents of heavy particles in turbulence," *Physics of Fluids*, **18**, 091702, (2006).

[28] E. J. P. Woittiez, H. J. J. Jonker, and L. M. Portela, "On the Combined Effects of Turbulence and Gravity on Droplet Collisions in Clouds: A Numerical Study," *Journal of the Atmospheric Sciences*, **66**, 1926–1943, (2009).

[29] J. Davila and J. C. R. Hunt, "Settling of small particles near vortices and in turbulence," *Journal of Fluid Mechanics*, **440**, 117–145, (2001).

[30] S. Ghosh, J. Dávila, J. Hunt, A. Srdic, H. Fernando, and P. Jonas, "How turbulence enhances coalescence of settling particles with applications to rain in clouds," *Proceedings of the Royal Society A: Mathematical, Physical and Engineering Sciences*, **461**, 3059–3088, (2005).

[31] W. H. Snyder and J. L. Lumley, "Some measurements of particle velocity autocorrelation functions in a turbulent flow," *Journal of Fluid Mechanics*, **48**, 41–71, (1971).

[32] B. Gopalan, E. Malkiel, and J. Katz, "Experimental investigation of turbulent diffusion of slightly buoyant droplets in locally isotropic turbulence," *Physics of Fluids*, **20**, 095102, (2008).

[33] Z.-M. Cao, K. Nishino, S. Mizuno, and K. Torii, "PIV measurement of internal structure of diesel fuel spray," *Experiments in Fluids*, **29**, S211–S219, (2000).

[34] L.-P. Wang, Y. Xue, O. Ayala, and W. W. Grabowski, "Effects of stochastic coalescence and air turbulence on the size distribution of cloud droplets," *Atmospheric Research*, **82**, 416–432, (2006).

[35] E. Bodenschatz, S. P. Malinowski, R. A. Shaw, and F. Stratmann, "Can We Understand Clouds Without Turbulence?," *Science (New York, N.Y.)*, **327**, 970–971, (2010).

[36] H. Siebert, K. Lehmann, and M. Wendisch, "Observations of Small-Scale Turbulence and Energy Dissipation Rates in the Cloudy Boundary Layer," *Journal of Atmospheric Sciences*, **63**, 1451–1466, (2006).

[37] J.-L. Brenguier, T. Bourrianne, A. Araujo Coelho, J. Isbert, R. Peytavi, D. Trevarin, and P. Weschler, "Effects of stochastic coalescence and air turbulence on the size distribution of cloud droplets," *Journal of Atmospheric and Oceanic Technology*, **15**, 1077–1090, (1998).

[38] L. Chaumat and J.-L. Brenguier, "Droplet spectra broadening in cumulus clouds. Part II: microscale droplet concentration heterogeneities.," *Journal of Atmospheric Sciences*, **58**, 642–654, (2001).

[39] A. B. Kostinski and R. A. Shaw, "Scale-dependent droplet clustering in turbulent clouds.," *Journal of Fluid Mechanics*, **434**, 389–398, (2001).

[40] W. W. Grabowski and L.-P. Wang, "Growth of cloud droplets in a turbulent environment," *Annual Review of Fluid Mechanics*, **45**, 293–324, (2013).

[41] W. Hwang and J. K. Eaton, "Creating homogeneous and isotropic turbulence without a mean flow," *Experiments in Fluids*, **36**, 444–454, (2004).

[42] R. Zimmermann, H. Xu, Y. Gasteuil, M. Bourgoin, R. Volk, J.-F. Pinton, and E. Bodenschatz, "The Lagrangian exploration module: an apparatus for the study of statistically homogeneous and isotropic turbulence.," *The Review of Scientific Instruments*, **81**, 055112, (2010).

[43] K. Chang, G. P. Bewley, and E. Bodenschatz, "Experimental study of the influence of anisotropy on the inertial scales of turbulence," *Journal of Fluid Mechanics*, **692**, 464–481, (2012).

[44] C. Goepfert, J.-L. Marié, D. Chareyron, and M. Lance, "Characterization of a system generating a homogeneous isotropic turbulence field by free synthetic jets," *Experiments in fluids*, **48**, 809–822, (2010).

[45] S. Krüger and G. Grünefeld, "Droplet velocity and acceleration measurements in dense sprays by laser flow tagging," *Applied Physics B*, **615**, 611–615, (2000).

[46] H.-E. Albrecht, M. Borys, N. Damaschke, and C. Tropea, *Laser doppler and phase doppler measurement techniques*. Berlin: Springer Verlag, (2003).

[47] R. J. Adrian and J. Westerweel, *Particle Image Velocimetry*. New York: Cambridge University Press, 1 ed., (2011).

[48] M. Raffel, C. Willert, and J. Kompenhans, *Particle Image Velocimetry: A Practical Guide*. Berlin: Springer, 1st ed., (1998).

[49] J. Sheng, H. Meng, and R. Fox, "A large eddy PIV method for turbulence dissipation rate estimation," *Chemical Engineering Science*, **55**, 4423–4434, (2000).

[50] J. Smagorinsky, "General circulation experiments with the primitive equations, I. The basic experiment," *Monthly Weather Review*, **91**, 99–164, (1963).

[51] J. de Jong, L. Cao, S. H. Woodward, J. P. L. C. Salazar, L. R. Collins, and H. Meng, "Dissipation rate estimation from PIV in zero-mean isotropic turbulence," *Experiments in Fluids*, **46**, 499–515, (2008).

[52] G. P. Bewley, K. Chang, and E. Bodenschatz, "On integral length scales in anisotropic turbulence," *Physics of Fluids*, **24**, 061702, (2012).

[53] S. B. Pope, *Turbulent Flows*. Cambridge, UK: Cambridge University Press, 1st ed., (2000).

[54] K. R. May, "An Improved Spinning Top Homogeneous Spray Apparatus," *Journal of Applied Physics*, **20**, 932, (1949).

[55] W. H. Walton and W. C. Prewett, "The Production of Sprays and Mists of Uniform Drop Size by Means of Spinning Disc Type Sprayers," *Proceedings of the Physical Society. Section B*, **62**, 341–350, (1949).

[56] C. N. Davies and P. K. P. Cheah, "Spinning generators of homogeneous aerosols," *Journal of Aerosol Science*, **15**, 719–739, (1984).

[57] G. König, K. Anders, and A. Frohn, "A New Light-Scattering Technique to Measure the Diameter of Periodically Generated Moving Droplets," *Journal of Aerosol Science*, **17**, 157–167, (1986).

[58] R. Ragucci, A. Cavaliere, and P. Massoli, "Drop sizing by laser light scattering exploting intensity oscillation in the Mie regime," *Particle and Particle Systems Characterization*, **7**, 221–225, (1990).

[59] N. Damaschke, H. Nobach, and C. Tropea, "Ptical limits of particle concentration for multi-dimensional particle sizing techniques in fluid mechanics," *Experiments in Fluids*, **32**, 143–152, (2002).

[60] M. Maeda, T. Kawaguchi, and K. Hishida, "Novel interferometric measurement of size and velocity distributions of spherical particles in fluid flows," *Measurement Science & Technology*, **11**, 308–316, (2000).

[61] Y. Hardalupas, S. Sahu, A. M. K. P. Taylor, and K. Zarogoulidis, "Simultaneous planar measurement of droplet velocity and size with gas phase velocities in a spray by combined ILIDS and PIV techniques," *Experiments in Fluids*, **49**, 417–434, (2010).

[62] S. Dehaeck and J. P. a. J. Beeck, "Designing a maximum precision interferometric particle imaging set-up," *Experiments in Fluids*, **42**, 767–781, (2007).

[63] T. Kawaguchi, Y. Akasaka, and M. Maeda, "Size measurements of droplets and bubbles by advanced interferometric laser imaging technique," *Measurement Science & Technology*, **13**, 308–316, (2002).

[64] R. N. Berglund and B. Y. H. Liu, "Generation of monodisperse aerosol standards," *Environmental Science & Technology*, **7**, 147–153, (1973).

[65] A. Gañán Calvo and A. Barrero, "A novel pneumatic technique to generate steady capillary microjets," *Journal of Aerosol Science*, **30**, 117–125, (1999).

[66] W. G. Cochran, "The flow due to a rotating disc," *Proceedings of the Cambridge Philosophical Society*, **30**, 365–375, (1934).

[67] W. Hinds, *Aerosol technology: properties, behavior, and measurement of airborne particles*. Wiley-Interscience, Wiley, (1999).

[68] D. J. Griffiths, *Introduction to Quantum Mechanics.* Upper Saddle River, NJ: Prentice Hall, Pearson Education Ltd, second ed., (2005).

[69] N. J. Turro, *Modern Molecular Photochemistry.* Menlo Park, Califonia: Benjamin/Cummings, (1978).

[70] M. M. Koochesfahani and D. G. Nocera, "Molecular Tagging Velocimetry," in *Springer Handbook of Experimental Fluid Mechanics* (C. Tropea, A. Yarin, and F. J. Foss, eds.), ch. 5.4, Berlin: Springer Verlag, (2007).

[71] W. Lempert, P. Ronney, and K. Magee, "Flow tagging velocimetry in incompressible flow using photo-activated nonintrusive tracking of molecular motion (PHANTOMM)," *Experiments in Fluids*, **18**, 249 – 257, (1995).

[72] N. Dam, R. Klein-Dowel, N. Sijtsema, and J. ter Muelen, "Nitric oxide flow tagging in unseeded air," *Optics Letters*, **26**, 36–38, (2001).

[73] S. I. Weissman, "Intramolecular Energy Transfer: The Fluorescence of Complexes of Europium," *Journal of Chemical Physics*, **10**, (1942).

[74] G. E. Buono-Core, H. Li, and B. Marciniak, "Quenching of Excited States by Lanthanide Ions and Chelates in Solution," *Coordination Chemistry Reviews*, **99**, 55–87, (1990).

[75] S. Lis, M. Elbanowski, B. Makowska, and Z. Hnatejko, "Energy transfer in solution of lanthanide complexes," *Journal of Photochemistry and Photobiology A: Chemistry*, **150**, 233–247, (2002).

[76] L. Armelao, S. Quici, F. Barigelletti, G. Accorsi, G. Bottaro, M. Cavazzini, and E. Tondello, "Design of luminescent lanthanide complexes: From molecules to highly efficient photo-emitting materials," *Coordination Chemistry Reviews*, **254**, 487–505, (2010).

[77] N. Arnaud and J. Georges, "Comprehensive study of the luminescent properties and lifetimes of Eu^{3+} and Tb^{3+} chelated with various ligands in aqueous solutions: influence of the synergic agent, the surfactant and the energy level of the ligand triplet," *Spectrochimica Acta Part A: Molecular and Biomolecular Spectroscopy*, **59**, 1829–1840, (2003).

[78] C. T. Ingold, *Fungal spores. Their liberation and dispersal.* Oxford: Clarendon Press, (1971).

[79] K. R. Smith, "Fuel combustion, air pollution exposure, and health: the situation in developing countries," *Annual Review of Energy Environment*, **35**, 529–566, (1993).

[80] B. Sawford, "Turbulent Relative Dispersion," *Annual Review of Fluid Mechanics*, **33**, 289–317, (2001).

[81] J. P. L. C. Salazar and L. R. Collins, "Two-Particle Dispersion in Isotropic Turbulent Flows," *Annual Review of Fluid Mechanics*, **41**, 405–432, (2009).

[82] A. M. Obukhov, "Spectral energy distribution in turbulent flow," *Izvestiya Akademii Nauk SSSR.*, **5**, 453–566, (1941).

[83] M. Sommerfeld, "Theoretical and Experimental Modelling of Particulate Flow: Overview and fundamentals," (2000).

[84] J. Bominaar, M. Pashtrapanska, T. Elenbaas, N. Dam, H. ter Meulen, and W. van de Water, "Writing in turbulent air," *Phys. Rev. E*, **77**, 046312, (2008).

[85] J. Bec, L. Biferale, M. Cencini, A. Lanotte, and F. Toschi, "Intermittency in the velocity distribution of heavy particles in turbulence," *Journal of Fluid Mechanics*, **646**, 527–536, (2010).

[86] R. Mazumder, "Turbulence–particle interactions and their implications for sediment transport and bedform mechanics under unidirectional current: some recent developments," *Earth-Science Reviews*, **50**, 113–124, (2000).

[87] A. Lampa and U. Fritsching, "Spray structure analysis in atomization processes in enclosures for powder production," *Atomization and Sprays*, **21**, (2011).

[88] A. Pumir, B. I. Shraiman, and M. Chertkov, "The lagrangian view of energy transfer in turbulent flow," *EPL (Europhysics Letters)*, **56**, 379, (2001).

[89] S. Ayyalasomayajula, A. Gylfason, L. Collins, E. Bodenschatz, and Z. Warhaft, "Lagrangian Measurements of Inertial Particle Accelerations in Grid Generated Wind Tunnel Turbulence," *Physical Review Letters*, **97**, 144507, (2006).

[90] H. Tennekes and J. L. Lumley, *A First Course in Turbulence*. Cambridge, Maassachusetts: MIT Press, (1972).

[91] S. Sundaram and L. R. Collins, "Collision statistics in an isotropic particle-laden turbulent suspension. part 1. direct numerical simulations," *Journal of Fluid Mechanics*, **335**, 75–109, (1997).

[92] E. Balkovsky, G. Falkovich, and A. Fouxon, "Intermittent Distribution of Inertial Particles in Turbulent Flows," *Physical Review Letters*, **86**, 2790–2793, (2001).

[93] M. Wilkinson and B. Mehlig, "Caustics in turbulent aerosols," *Europhysics Letters*, **71**, 186–192, (2005).

[94] R. Monchaux, M. Bourgoin, and A. Cartellier, "Preferential concentration of heavy particles: A VoronoiÌĹ analysis," *Physics of Fluids*, **22**, 103304, (2010).

[95] L. Fiabane, R. Zimmermann, R. Volk, J.-F. Pinton, and M. Bourgoin, "Clustering of finite-size particles in turbulence," *Phys. Rev. E*, **86**, 035301, (2012).

[96] E. Villermaux and J. Duplat, "Mixing is an aggregation process," *Comptes Rendus MÃl'canique*, **331**, 515 – 523, (2003).

[97] E. Calzavarini, M. Kerscher, D. Lohse, and F. Toschi, "Dimensionality and morphology of particle and bubble clusters in turbulent flow.," *Journal of Fluid Mechanics*, **607**, 13–24, (2008).

[98] T. C. Halsey, M. H. Jensen, L. P. Kadanoff, I. Procaccia, and B. I. Shraiman, "Fractal measures and their singularities: The characterization of strange sets," *Phys. Rev. A*, **33**, 1141–1151, (1986).

[99] B. Mandelbrot, *The Fractal Geometry of Nature*. San Francisco: W.H. Freeman, (1983).

[100] C. Pasquero, A. Provenzale, and E. A. Spiegel, "Suspension and fall of heavy particles in random two-dimensional flow," *Physical Review Letters*, **91**, 054502, (2003).

SUMMARY

Glowing droplets: a diagnostic for particle-laden flows

Particle-laden flows surround us. From dust particles suspended in the air we breathe to the clouds that cover the sky, particle–fluid suspensions are ubiquitous. For instance, the internal combustion engine—one of the most prevalent machines—relies on the dispersion and evaporation of fuel droplets to achieve combustion. The homogeneity of the droplet distribution has an impact on the combustion efficiency, and given the current environmental and energy concerns, it is important to achieve the cleanest combustion possible.

Turbulence is known as a particularly efficient mixing agent, however, an anomalous behavior arises in turbulent particle-laden flows, that is, 'de-mixing' of the droplet suspension. This phenomenon is commonly referred to as preferential concentration, and has been documented in experiments and numerical simulations, yet most of our knowledge arises from statistical analysis. Through the development of a novel experimental technique, we aim at shedding light onto the dynamics of particle-laden flows. The technique consists of the generation of phosphorescent droplets which can be tagged and followed for relatively long periods of time.

The testing and development of an experimental technique requires a well characterized experimental setup. To this end, we have constructed a chamber capable of generating a highly turbulent homogenous, isotropic flow with a negligible mean velocity. Furthermore, we have fabricated an aerosol generator capable of producing monodisperse droplets. Additionally, a phosphorescent solution has been adapted to be used in our experiment. We use Europium (Eu^{3+}) as a phosphorescence agent.

Particle dispersion in a turbulent flow is well-documented process. It is of great importance in geophysical flows, such as volcanic ash and pollen transport. It also plays a crucial role in pollution control and catastrophic contaminant release. Nevertheless, most of the information we have about this process concerns the dispersion of fluid tracers at relatively long (integral) timescales. The longstanding issue of turbulent dispersion of heavy droplets is revisited using a novel experimental technique. Within a cloud of phosphorescent droplets, thin cylindrical volumes are tagged and recorded in a high-speed fashion as they are advected by the flow. The widening of these volumes provides experimental evidence of dispersion which is faster than that of fluid parcels. We explore the effect of inertia in the dispersion of heavy droplets by experimenting with several droplet diameters. A remarkable result is obtained where the spreading velocity of a cloud of heavy droplets is higher than the theoretical expectation for fluid tracers. Furthermore, there appears to be an optimum value for inertia where the droplets disperse fastest. This happens when the particle relaxation time is approximately twice the dissipative timescale of the turbulent flow.

Lastly, we look at the phenomenon of preferential concentration by tagging a thin slab within a cloud of droplets. First, spatial statistics of the droplet cloud are calculated and compared to available literature. We measure the dimensionality of the droplet cloud by calculating the correlation dimension. The dimensionality of the cloud is less than the expectation for a completely random distribution. Similarly, we measure the deviation from a homogeneous dispersion by measuring the probability density function of the local intensity. The dynamics of preferential concentration are probed by calculating the moments of the local concentration and looking the evolution in time. Our results show that the moments increase exponentially in time, which is in agreement with the theoretical expectation. Moreover, our data gives evidence that preferential concentration is a fast process which can be observed within the first few small-eddy turnover times.

ACKNOWLEDGMENTS

CURRICULUM VITAE

April 13, 1983:   **Born in Monterrey, México**

2002–2006:   **B.S. in Mechanical Engineering**
New Mexico State University
Las Cruces, NM, USA

2007–2009:   **M.S. in Mechanical Engineering**
New Mexico State University
Las Cruces, NM, USA

2009–2013:   **Ph.D. Candidate**
Turbulence and Vortex Dynamics
Applied Physics Faculty
Eindhoven University of Technology
Eindhoven, The Netherlands